



UNIVERSITY OF LEEDS

Simulated observations of and flow interactions with discs

Thomas Alexander Douglas

Department of Physics and Astronomy

University of Leeds

Submitted in accordance with
the requirements for the degree of

Doctor of Philosophy

2015

The candidate confirms that the work submitted is his own, except where work which has formed part of jointly authored publications has been included. The contribution of the candidate and the other authors of this work has been explicitly indicated. The candidate confirms that appropriate credit has been given within this thesis where reference has been made to the work of others.

This copy has been supplied on the understanding that it is copyright material and that no quotation from the thesis may be published without proper acknowledgement.

© 2015 The University of Leeds and Tom Douglas.

Preface

Within this thesis, chapter 3 has been based on work presented in the jointly authored publication “Simulated Observations of Young Gravitationally Unstable Protoplanetary Discs” by Douglas, T.A., Caselli, P., Ilee, J.D., Boley, A.C., Hartquist, T.W., Durisen, R.H. & Rawlings, J.M.C. (2013). As the lead author, I performed the radiative transfer simulations, conducted the analysis and wrote the text.

Acknowledgements

I would like to thank my supervisors Tom Hartquist, Paola Caselli, Julian Pitard and Melvin Hoare. Between you all I've learnt a huge amount from my time in Leeds and your guidance has been invaluable.

Also I'd like to thank my officemates and fellow PhD students. In particular Nichol Cunningham and John Fairlamb for always being there to have a moan with whenever things were going wrong and to John Ilee, both for being my academic big brother and for always having an appropriate (or not) Simpsons quotation for any moment.

Finally my most heartfelt thanks go out to my parents for always supporting me, without them I wouldn't have got to where I am today. And to Alex, for her objectively good Chinese food and for keeping me the rails these last few months.

Thank you

Abstract

This thesis presents simulations of the dynamics and radiation processes in accretion discs around young protostars. Firstly the dust continuum and molecular line emission from a gravitationally unstable, $0.4M_{\odot}$ disc around a young $1M_{\odot}$ mass protostar are calculated. Such massive, unstable discs are thought to be an early stage in the evolution of low mass protostars and the gravitational instabilities in them provide a method of transferring angular momentum outwards and mass inward when there is insufficient ionised material for magnetic instabilities to provide such torques. The potential for observations of such a disc in continuum and line emission with ALMA is explored using radiative transfer and synthetic observations and four molecular traces of spiral structure are identified.

Secondly, radiation-hydrodynamic models of accretion discs around $10M_{\odot}$ protostars of varying radii are presented. The effects of different driving parameters and accretion luminosity are explored. The resulting density distribution is analysed in order to distinguish between ionised and neutral material. The amount of mass lost, the linear and rotational velocity of the winds and the division of the mass between the slow, dense disc wind and the fast rarefied polar wind is analysed for each of the models. The amount of visible mass

lost through the disc is found to be strongly related to the luminosity of the disc and most of the disc mass is launched from the inner regions rather than mass loading further out.

Finally radiative transfer modeling and synthetic observations are performed for the hydrodynamic models from the previous chapter. These include radio free-free emission, ionised carbon forbidden lines and hydrogen recombination lines. These are compared to observations of discs around MYSOs. The radio free-free emission is used as the input to a telescope simulation in order to provide synthetic interferometer observations with the e-Merlin radio telescope network.

Abbreviations & Symbols

ALMA	Atacama Large Millimetre Array
FWHM	Full Width, Half Maximum
FWZI	Full Width, Zero Intensity
AMR	Adaptive Mesh Refinement
GI	Gravitational Instability
GMC	Giant Molecular Cloud
IR	Infrared
ISM	Interstellar Medium
KH	Kelvin-Helmholtz
LTE	Local Thermodynamic Equilibrium
MYSO	Massive Young Stellar Object
MRI	Magneto-Rotational Instability
RT	Rayleigh-Taylor
SED	Spectral Energy Distribution
UV	Ultraviolet
YSO	Young Stellar Object
c	Speed of light in a vacuum
h	Planck constant
k_B	Boltzmann constant
G	Gravitational constant
ρ	Mass density
p	Pressure
e	Total (thermal+kinetic) energy
\mathbf{a}	Acceleration
\mathbf{u}	Velocity
σ_e	Thompson scattering cross-section
j_ν	Emission coefficient
α_ν	Absorption coefficient
I_ν	Specific intensity
L	Luminosity
J	Angular momentum

Contents

1	Introduction	1
1.1	Outline	1
1.2	Star formation	2
1.2.1	Low mass star formation	7
1.2.2	High mass star formation	8
1.3	Circumstellar discs	10
1.3.1	The α disc	14
1.3.2	Gravitational instability	16
1.3.3	Radiative disc winds	18
2	Numerical Methods	25
2.1	Radiative transfer	26
2.1.1	Theory	26
2.1.2	LIME	30
2.1.3	Grid construction	34
2.2	Hydrodynamics	38
2.2.1	Equations of Hydrodynamics	38
2.2.2	Source terms	44

CONTENTS

2.2.3	Adaptive mesh refinement	46
3	Simulated observations of gravitationally unstable young proto-planetary discs	49
3.1	Introduction	49
3.2	Description of the Model	51
3.2.1	Physical structure	51
3.2.2	Chemical structure	56
3.3	Model Results	58
3.4	Predictions for ALMA	64
3.5	Conclusions and further work	71
4	Hydrodynamic simulations of line mediated radiatively driven disc winds	75
4.1	Introduction	75
4.2	Description of the Models	77
4.2.1	Model initial and boundary conditions	78
4.2.2	Hydrodynamic equations & source terms	85
4.2.3	Calculation of the line driving force	87
4.3	Analysis	94
4.4	Model Results	97
4.5	Conclusions	111
5	Radiative transfer and synthetic observations of disc wind simulations	113
5.1	Introduction	113

5.2	Method	115
5.2.1	Model interpolation	115
5.2.2	Bremsstrahlung	117
5.2.3	Hydrogen photoionisation, recombination and Transition lines	120
5.2.4	C ⁺ lines	123
5.3	Results	126
5.3.1	Bremsstrahlung	126
5.3.2	C ⁺ lines	139
5.3.3	Hydrogen recombination lines	147
5.4	e-Merlin simulated observations	151
5.5	Conclusions	160
6	Conclusions	163
6.1	Summary of conclusions	163
6.1.1	Simulated observations of gravitationally unstable young protoplanetary discs	163
6.1.2	Hydrodynamic simulations of line mediated radiatively driven disc winds	165
6.1.3	Radiative transfer and synthetic observations of disc wind simulations	166
6.2	Future work	168
6.2.1	Simulated observations of gravitationally unstable young protoplanetary discs	168

CONTENTS

6.2.2	Hydrodynamic simulations and radiative transfer calculations of line mediated radiatively driven disc winds	169
6.3	Final remarks	171
	References	172

List of Figures

1.1	Hierarchical cloud structure in CO, C ¹⁸ O and CS.	3
1.2	Schematic overview of star formation	6
1.3	The molecular outflow HH211	13
1.4	A sketch illustrating the geometry leading to the magneto-rotational instability	15
1.5	Gravitationally unstable discs	17
1.6	Density and velocities for a radiatively driven disc wind	20
1.7	Radiatively driven disc wind from a MYSO	21
1.8	The MYSO S140 IRS 1	23
2.1	Delaunay grids of points	32
2.2	LIME gridded points and photon propagation paths.	33
2.3	Model points histogram.	35
2.4	output scaling with number of model points.	37
2.5	The effect of averaging LIME runs.	38
2.6	Reimann problem schock tube.	42
2.7	AMR grids.	47
3.1	L1544 model	53

LIST OF FIGURES

3.2	Disc mid-plane velocity and best fit.	54
3.3	Density and temperature structure of the disc	55
3.4	Molecular column densities.	57
3.5	Molecular integrated intensity and intensity weighted velocity maps.	61
3.6	Molecular integrated intensity, intensity weighted velocity and position velocity diagrams.	63
3.7	Synthetic continuum observations.	65
3.8	H ₂ CO channel maps.	66
3.9	C ¹⁷ O synthetic observations.	68
3.10	Integrated intensity maps of synthetic observations.	69
3.11	Position velocity diagrams for each of the lines simulated with CASA. The green curve on each diagram is the best fit curve to the azimuthally averaged rotation profile from fig. 4.	70
3.12	Spectra taken from positions in figure 3.10.	71
4.1	The initial density (in kg/m^{-3} and velocity (scaled so the largest arrow is $2000 km s^{-1}$) distribution for one of the models simulated. Inset: inner region ($R = 0 - 10 R_*$) of the model.	78
4.2	Density and velocity distribution for 1D spherical CAK model.	82
4.3	The effect to fixing the inner region of the stellar wind.	83
4.4	Fractional differences in total mass, momentum, pressure and angular momentum with resolution.	84
4.5	CAK k and α parameters as a function of effective stellar surface temperature.	86
4.6	The geometry used in the calculations of the disc fluxes.	89

4.7	The flux vectors from a single point of the discretised disc of the R5.5 model.	92
4.8	The total disc flux vectors from reflected/reprocessed starlight and accretion heating for the R5.5 model.	93
4.9	The total flux vectors including disc and stellar contributions for the R5.5 model.	93
4.10	A snapshot of the total acceleration.	94
4.11	The ionisation fraction (top), mass density (bottom) and their product divided by the mean atomic mass, the number density of ions (middle), for the R5.5 model.	96
4.12	Density distributions of the models after 2×10^8 s (~ 6.3 yrs).	98
4.13	Densities and velocities of the models at 270 AU.	99
4.14	Definitions of the regions used in the analysis.	100
4.15	as fig 4.14 for each model.	101
4.16	Total outward mass fluxes.	103
4.17	The ratio of mass and energy of unbound material in the polar wind and disc-wind regions	104
4.18	The mass loss rate of the disc wind (green points, blue line) and the mean radiation flux from the disc (for $R < 10r_*$).	105
4.19	Cumulative mass fluxes as a function of latitude angle	106
4.20	The wind performance parameter for each of the models.	107
4.21	Velocities of the ionised material in the disc wind.	108
4.22	Rotational velocities of the ionised material in the disc wind.	109
4.23	Velocities of the ionised material in the polar wind.	109
4.24	Rotational velocities of the ionised material in the disc wind.	110

LIST OF FIGURES

5.1	The interpolated ion mass density (in g/cm^3) through the centre of the cube used for radiative transfer. The axes labels are in pixel numbers, and each pixel is a cell $(2 \text{ au})^3$	117
5.2	The value of the gaunt factor for various values of γ^2 and u , as defined in equation 5.4. Reproduced from Rybicki & Lightman (1986).	120
5.3	Free-free emission for the discs at an inclination angle of 0° and a frequency of 1.5GHz.	127
5.4	Free-free emission for the discs at an inclination angle of 45° and a frequency of 1.5GHz.	127
5.5	Free-free emission for the discs at an inclination angle of 75° and a frequency of 1.5GHz.	128
5.6	Free-free emission for the discs at an inclination angle of 0° and a frequency of 5GHz.	129
5.7	Free-free emission for the discs at an inclination angle of 45° and a frequency of 5GHz.	129
5.8	Free-free emission for the discs at an inclination angle of 75° and a frequency of 5GHz.	130
5.9	Free-free emission for the discs at an inclination angle of 0° and a frequency of 23GHz.	131
5.10	Free-free emission for the discs at an inclination angle of 45° and a frequency of 23GHz.	131
5.11	Free-free emission for the discs at an inclination angle of 75° and a frequency of 23GHz.	132

5.12	The 23GHz flux plotted against the mass flux divided by terminal velocity in the disc wind(blue crosses, best fit red line) and total mass flux (green crosses, best fit cyan line).	133
5.13	The free-free emission spectra for each of the models viewed with an inclination angle of 0°	134
5.14	The spectral index for each of the models as a function of frequency, for an inclination angle of 0°	134
5.15	The free-free emission spectra for each of the models viewed with an inclination angle of 45°	135
5.16	The spectral index for each of the models as a function of frequency, for an inclination angle of 45°	135
5.17	The free-free emission spectra for each of the models viewed with an inclination angle of 75°	136
5.18	The spectral index for each of the models as a function of frequency, for an inclination angle of 75°	136
5.19	Optical depths of the free free emission for the R10.0 model.	139
5.20	C ⁺ lines for the R05.5 model.	141
5.21	C ⁺ lines for the R07.7 model.	142
5.22	C ⁺ lines for the R10.0 model.	143
5.23	C ⁺ lines for the R11.7 model.	144
5.24	C ⁺ lines for the R16.2 model.	145
5.25	C ⁺ lines for the R07.7cut model.	146
5.26	The spectra of the hydrogen 66-65 line for the R05.5 model for 3 different inclinations.	148

LIST OF FIGURES

5.27	The spectra of the hydrogen 66-65 line for the R07.7 model for 3 different inclinations.	148
5.28	The spectra of the hydrogen 66-65 line for the R10.0 model for 3 different inclinations.	149
5.29	The spectra of the hydrogen 66-65 line for the R11.7 model for 3 different inclinations.	149
5.30	The spectra of the hydrogen 66-65 line for the R16.2 model for 3 different inclinations.	150
5.31	The spectra of the hydrogen 66-65 line for the R07.7cut model for 3 different inclinations.	150
5.32	Sythetic observations with e-Merlin at 1.5GHz and 0°	152
5.33	Sythetic observations with e-Merlin at 5GHz and 0°	153
5.34	Sythetic observations with e-Merlin at 23GHz and 0°	154
5.35	Sythetic observations with e-Merlin at 1.5GHz and 45°	155
5.36	Sythetic observations with e-Merlin at 5GHz and 45°	156
5.37	Sythetic observations with e-Merlin at 23GHz and 45°	157
5.38	Sythetic observations with e-Merlin at 1.5GHz and 75°	158
5.39	Sythetic observations with e-Merlin at 5GHz and 75°	159
5.40	Sythetic observations with e-Merlin at 23GHz and 75°	160

List of Tables

1.1	Properties of Molecular Clouds, Clumps and Cores	4
2.1	LIME gridding parameters	36
3.1	ALMA line sensitivities $\sim 300\text{GHz}$	64
4.1	Model parameters	85

LIST OF TABLES

Chapter 1

Introduction

1.1 Outline

This thesis is on simulations of discs around young protostars and synthetic observations of the simulations.

Chapter 1 presents previous work in the field of star formation and provides context for the work in this thesis.

Chapter 2 outlines the numerical methods used in simulations to create the work presented in this thesis.

Chapter 3 presents work, previously published in Douglas *et al.* (2013), on synthetic observations of a protoplanetary disc around a young class 0 protostar. The disc has sufficient mass to become gravitationally unstable and the simulations show that the spiral density waves which occur will be visible with the next generation of astronomical instruments (i.e. the Atacama Large Millimetre Array, ALMA). The synthetic observations were created by combining previous work on the hydrodynamics of gravitationally unstable discs (Boley *et al.* 2007a)

and on the chemistry within such a disc (Ilee *et al.* 2011) with radiative transfer and telescope simulation codes. This allows for accurate prediction of which molecular lines will be sufficiently excited, and on a large enough spatial scale, to be seen clearly with ALMA.

Chapter 4 features axis-symmetric radiation-hydrodynamic simulations of line driven disc winds from an accretion disc around a $10M_{\odot}$, $8500L_{\odot}$ protostar accreting at $10^{-4} M_{\odot} yr^{-1}$. These simulations include radiation line driving terms governed by Sobolev optical depths and use a distributed luminosity in order to simulate emission from both the star and accretion disc. Morphologies and mass fluxes are calculated for a range of protostellar radii, and it is found as the star becomes hotter and smaller a stronger wind is blown from the disc.

Chapter 5 contains observational predictions of the work shown in chapter 4. Radio free-free emission maps, forbidden line C^{+} emission and Hydrogen recombination of the models from chapter 4 are calculated and synthetic observations are created where appropriate.

Chapter 6 presents a summary of the findings of this thesis and describes possible future work.

1.2 Star formation

The basic process by which stars form has been well understood for a number of years (e.g. Mestel & Spitzer 1956, Roberts 1969). Clouds of material in the coldest phase of the ISM, the cold molecular component, contain regions which are gravitationally unstable and these collapse to form either single stars or bound multiples.

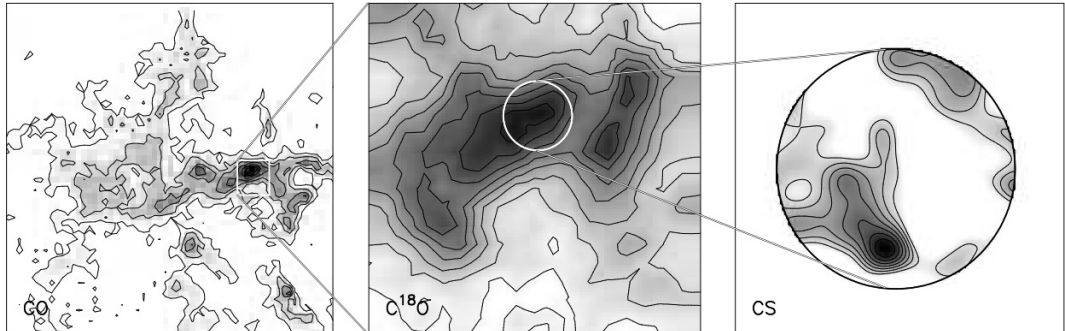


Figure 1.1: Hierarchical cloud structure. The three panels show a representative view from cloud to clump to core. The bulk of the molecular gas (cloud; left panel) is best seen in CO which, although optically thick, faithfully outlines the location of the H_2 . Internal structure (clumps; middle panel) is observed at higher resolution in an optically thin line such as C^{18}O . With a higher density tracer such as CS, cores (right panel) stand out. The observations here are of the Rosette molecular cloud (figure taken from Blitz & Williams 1999).

Most of the star formation, both in this galaxy and in others, occurs in large clouds of molecular gas (Kennicutt & Evans 2012), referred to as giant molecular clouds (GMCs). These clouds are highly turbulent (Zuckerman & Evans 1974) and feature prominent filamentary structure (Bergin & Tafalla 2007). It is currently unclear if they are transient structures resulting from colliding flows which dissipate on the order of a crossing time (Ballesteros-Paredes *et al.* 1999), or if they are quasi-equilibrium structures with the interior turbulence being continuously driven (possibly by feedback from star formation or galactic rotation e.g. Kim & Ostriker 2007, Vázquez-Semadeni 2011 and Boneberg *et al.* 2014).

The interior structure of GMCs can be subdivided into clumps (which are continuous regions in position-position-velocity (PPV) space), which themselves may contain significant interior structure. Within these clumps individual gravitationally bound cores are found (see figure 1.1).

Individual dense cores generally fall into one of two categories: firstly pre-

Table 1.1: Physical properties of Molecular Clouds and their sub-components (adapted from Bergin & Tafalla (2007))

	Clouds	Clumps	Cores
Mass (M_{\odot})	$10^3 - 10^4$	50-500	0.5-5
Size (pc)	2-15	0.3-3	0.03-0.2
Mean density (m^{-3})	$5 \times 10^7 - 10^8$	$10^9 - 10^{10}$	$10^{10} - 10^{11}$
Velocity extent (km s^{-1})	2-5	0.3-3	0.1-0.3
Crossing time (Myr)	2-4	~ 1	0.5-1
Gas temperature (K)	~ 10	10-20	8-12
Examples	Taurus, Oph, Musca	B213, L1709	L1544, L1498, B86

stellar cores are the progenitors of single stars (or bound multiples), they are gravitationally unstable to collapse and show observational signs of infall towards the centre; the second, starless cores, are stable structures showing no signs of collapse. The condition for gravitational collapse of a sphere of uniform density is given by equation 1.1 (Jeans 1929) in which ρ and T are the density and temperature of the gas, μ is the mean molecular mass and k_B and G are the Boltzmann and gravitational constants:

$$M_J = \sqrt{\rho^{-1} \left(\frac{\pi k_B T}{\mu G} \right)^3}. \quad (1.1)$$

If the mass of a core is greater than M_J it will undergo collapse as long as its temperature remains constant. However equation 1.1 only accounts for thermal pressure providing support against collapse. Molecular clouds are observed to have both magnetic fields (Kazes & Crutcher 1986) and supersonic turbulence Schneider *et al.* (2011), both of which could provide pressure and allow regions of masses greater than the Jeans mass to be stable against collapse.

Once a volume of gas becomes Jeans unstable it will continue to collapse as

long as it is able to radiate away the gravitational energy released and remains isothermal. When the core becomes optically thick to the main coolants present (primarily dust thermal emission and CO rotational transitions) the collapse is no longer isothermal and the temperature of the cloud will begin to rise, stabilizing it against collapse. As thermal pressure increases in the optically thick centre of the core the collapse will halt, resulting in an equilibrium structure referred to as the first hydrostatic core. This is only a transitory phase however, as radiation is still being emitted from the edge of the optically thick region and it will eventually cool down sufficiently to collapse further. This first hydrostatic core phase of the collapse has been theoretically predicted for a long time (e.g. Larson 1969), but due to its short duration and heavily embedded nature it is only recently that observations of this phase have become possible (Enoch *et al.* 2010; Chen *et al.* 2010; Pineda *et al.* 2011).

For any volume of gas we can calculate a free-fall time, which is the time it would take for the region to collapse down to a significantly smaller radius in the absence of any support mechanism (equation 1.2).

$$t_{ff} = \sqrt{\frac{3\pi}{32G\rho}}. \quad (1.2)$$

For a typical molecular cloud of density 10^8 particles per m^3 , $t_{ff} \simeq 3 \times 10^6$ yrs. That this is comparable with the sound crossing time of these clouds (see table 1.1) demonstrates that GMCs as a whole are not gravitationally collapsing. We can also define the Kelvin-Helmholtz time (the time taken for a protostar to radiate

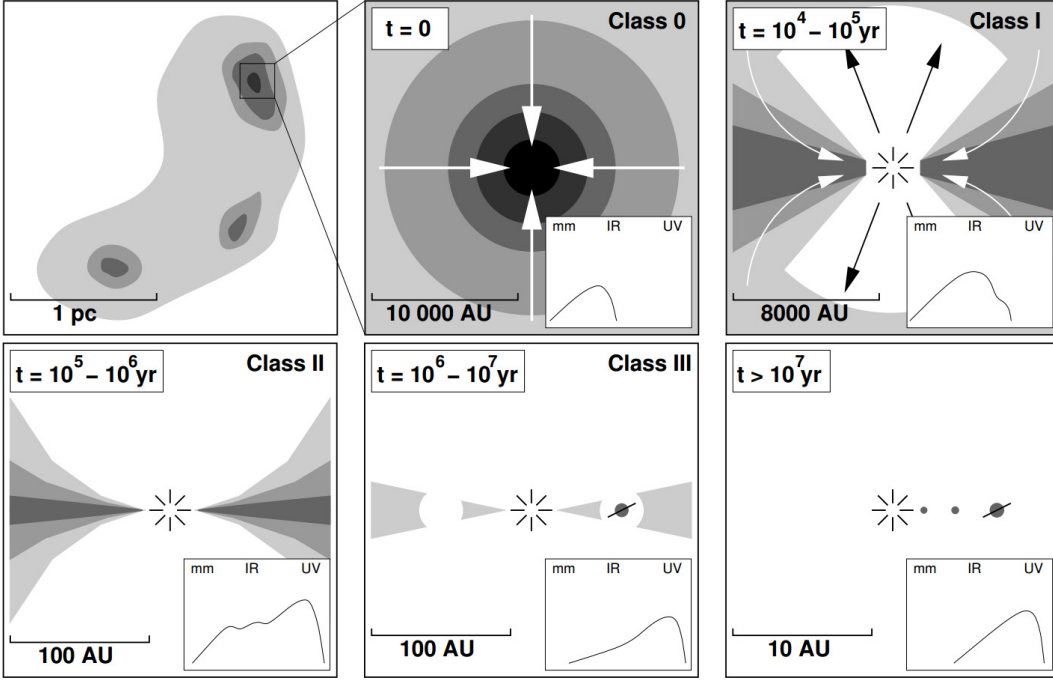


Figure 1.2: A schematic of the different stages of star formation and their observational category. The labels show the time passed since the formation of the protostar and inset are the SEDs used in classification. Adapted from Jonkheid (2006).

away a significant fraction of its gravitational energy):

$$t_{KH} = \frac{E_{grav}}{L_*} = \frac{3}{5} \frac{GM^2}{RL_*}. \quad (1.3)$$

Taking the freefall time for a core of radius 0.1 pc and density of $10^{10} m^{-3}$ and equating that with the Kelvin-Helmholtz time allows us to define the boundary between low mass star formation, where radiation isn't dynamically significant and high mass, where it is. Assuming that $L_* \propto (M_*/M_\odot)^{3.5}$ this simple method gives the boundary between the two modes of star formation at ~ 10 solar masses.

1.2.1 Low mass star formation

Observationally, YSOs are split into 4 classes, 0-III, distinguished by their spectral energy distribution (SED). Classes I, II and III were originally proposed by Lada (1987) who categorized them according to the spectral index, a , in the region of $10 \mu m \leq \lambda \leq 100 \mu m$:

$$a = \frac{d \log(\lambda F_\lambda)}{d \log(\lambda)} \quad (1.4)$$

Values $+3 \geq a \geq 0$ correspond to class I objects, $0 \geq a \geq -2$ are for class II objects and $-2 \geq a \geq -3$ are for class III objects. This was extended by Andre *et al.* (1993) to include class 0 sources for $a \geq +3$.

Class 0 objects are a collapsing envelope of material onto a newly formed/forming protostar. The SED observed has the shape of a black body at $\sim 30K$ with the peak of the flux at (sub)millimetre wavelengths. This is warmer than that of a pre-stellar core ($5\sim 15K$) due to the re-absorption of stellar luminosity heating the infalling material. Simulations have shown that material could form a disc during this stage even before the protostar forms (Machida *et al.* 2011a).

After $10^4 - 10^5$ years Class I sources have cleared out a significant amount of material along their rotation axis. This allows, depending on inclination, observations deeper into the envelope to warmer regions. Correspondingly, there is a shift in the SED to higher frequencies. In this regime material is primarily accreting onto the protostar via the disc rather than collapsing spherically.

Class II is $10^5 - 10^6$ years after the protostar formation. By this point there is little of a spherical envelope remaining and the majority of the mass not in the protostar is in the accretion disc. As the source is now almost entirely exposed

the SED is that of the protostar itself, with an additional longer wavelength (IR) component from the cooler disc.

Class III sources, occurring after $10^6 - 10^7$ years are protostars around which most of the disc mass has either been accreted or expelled. They are seen as stellar SEDs with a faint infrared excess due to the remnant disc. Planet formation is expected to occur during this phase and resolved observations of discs with gaps in them are believed to be evidence for this (e.g. ALMA Partnership *et al.* 2015; Osorio *et al.* 2014). After this stage is complete the star is said to be on the main sequence.

1.2.2 High mass star formation

Massive stars play a key role in star formation; they profoundly affect their surroundings by injecting significant amounts of momentum and energy through outflows, stellar winds and supernovae. This leads to them having a large effect on the environment in which other stars are formed. However, less is known about their formation than their low mass counterparts (see Tan *et al.* 2014) as they are much more difficult to observe. The difficulty in observing MYSOs comes partly from their rarity, meaning that the average distance to one is much larger than the average distance to a low mass YSO. In addition, MYSOs form and evolve over a much shorter period than low mass protostars. This again increases the rarity of observable MYSOs but also means that the ones which do exist are often still obscured by a large amount of dust.

One of the main unknowns about massive star formation is the source of matter feeding the protostar. The two main models for this are under active study

are Core Accretion and Competitive Accretion. In the core accretion model, high mass star formation is a scaled up version of low mass star formation and single stars (or small multiples) form from a single massive core which undergoes gravitational collapse to a disc and protostar(s). In this model the initial mass function (IMF) of stars is directly related to the core mass function (CMF) by an efficiency so that $M_* = \eta M_{core}$ with an efficiency (η) on the order of a half. For massive stars to form via this method, cores with mass $M \gg M_\odot$ must collapse without fragmenting into a cluster of low mass stars.

In the competitive accretion model, there is no single bound structure that undergoes collapse to form the star. Instead massive stars always form at the centre of clusters and the gravitational potential of the cluster as a whole funnels matter to the stars in the centre which accrete faster and become massive. Massive stars formed in this way would need to always form in association with a cluster of other stars and to be close to the centre of mass of this cluster.

Massive stars are highly luminous ($\sim 10^4 L_\odot$ for a $10M_\odot$ star) and this causes significant radiation pressure to be felt by material around the star. If the accretion onto the star was symmetric, this radiation pressure would lead to a truncation of the IMF when the radiation became strong enough to balance gravity. However recent 3D simulations have shown that when an accretion disc forms matter is still able to accrete onto the protostar though the disc thanks to a combination of the ‘flashlight’ effect (the radiation field becoming non-isotropic due to absorption and re-emission from the disc) and the high optical depth of the disc shielding the interior mass from the radiation pressure (Krumholz *et al.* 2005; Kuiper *et al.* 2015).

Recent modeling of the structure of protostars as they accrete mass at the high rates needed to overcome radiation pressure shows that they will increase in radius up to $\sim 100R_{\odot}$ as they gain in mass (Hosokawa & Omukai 2009). This inflation is caused by the entropy of the accreted mass being unable to be radiated away through the highly opaque cool material. As the protostar increases in temperature the opacity drops and entropy moves towards the surface, swelling the protostar's radius. This large increase in radius has the effect of decreasing both the surface temperature and gravity of the protostar.

1.3 Circumstellar discs

Circumstellar discs are ubiquitous around YSOs. They are seen around stars from brown dwarfs with masses $< 0.08M_{\odot}$ (e.g. Ricci *et al.* 2014, Liu *et al.* 2015) to high mass stars $> 8M_{\odot}$ (Wang *et al.* 2012) and even around binaries (Sánchez-Monge *et al.* 2013). These discs are formed as a natural consequence of the conservation of angular momentum from the parent cores. Consider a core with radius 0.1 pc ($3 \times 10^{15} \text{m} \sim 1$ Jeans length of a core) with a typical angular velocity of 10^{-14}s^{-1} (Lodato 2008). The angular momentum of the core

$$J = \Omega_{core} \lambda_J^2 \simeq 10^{17} m^2 s^{-1}. \quad (1.5)$$

Equating this with the angular momentum of a Keplerian orbit about a $1 M_{\odot}$ star at radius R gives:

$$\begin{aligned}
 J &= 10^{17} m^2 s^{-1} \\
 &= J_k = \sqrt{GM R} \\
 R &= \frac{J^2}{GM} = 7 \times 10^{13} m \simeq 500 AU.
 \end{aligned}
 \tag{1.6}$$

Thus, for mass to move inwards to smaller radii and accrete onto the central protostar there has to be some method of transferring this angular momentum away from the disc. This is commonly referred to as the “angular momentum problem”.

These discs are mainly composed of atomic or molecular hydrogen (depending on the luminosity of the central YSO and the accretion rate) and dust grains, with dust composing 1-2% by mass (Lodato 2008). If the opacities of the dust are known, then the mass of the disc can be obtained from its sub-millimetre emission, to which discs are typically optically thin. In a survey of discs in the Taurus-Auriga complex, Andrews & Williams (2007) measured a range of disc masses from $0.1 M_{\odot}$ to $10^{-4} M_{\odot}$ with a median of $5 \times 10^{-3} M_{\odot}$. Sizes ranged from ~ 100 to 1000 AU. However, the dust opacities are not well known causing large systematic errors on these values. Hartmann *et al.* (2006) show that if the dust has coagulated into larger grains then their opacity would be reduced and the corresponding mass estimate would increase.

Numerical studies of the collapse of a core towards a disc (Machida & Matsumoto 2011) suggest that discs form very early on in the collapse of a pre-stellar core and that they maintain their original spherical shape and structure even

after disc formation begins. This means in order to detect these earliest discs observations need to penetrate through the surrounding cloud in order to detect the disc. Other simulations show that young isolated systems are expected to contain a significant fraction of the mass in extended discs (Hayfield *et al.* 2011a) and these to be gravitationally unstable.

In addition to providing a path for material to accrete onto the protostar the disc also has a role in the launching of jets and outflows (e.g. Blandford & Payne 1982; Pudritz & Norman 1983; Shu *et al.* 1997, see figure 1.3). Outflows are launched from the disc along the rotation axis by a combination of magnetic pressure and magneto-centrifugal forces. These outflows have been seen to be rotating (Bacciotti *et al.* 2002) and so can also carry angular momentum away from the disc. In the case of high mass stars they also clear out a low density channel away from the protostar by sweeping up material in their vicinity, allowing radiation to escape. This leads to an anisotropy in the radiation field with the radiation pressure greater along the axis of the outflow than in the radial direction (Yorke & Sonnhalter 2002). This “flashlight” effect reduces the ability of the radiation to overcome gravity in the plane of the accretion disc.

Krumholz & Matzner (2009) simulated the collapse of a prestellar core using 3D coupled radiation-hydrodynamics with grey flux-limited diffusion (FLD). They found that accretion proceeded through a disc even when the radiation pressure was strong enough to prevent spherical accretion. In this work the accretion onto the protostar was mainly via the disc, but due to the combination of the radiation and gravitational forces the disc was unstable, leading to a highly variable accretion rate. The disc itself was fed mainly through radiation-driven Rayleigh-Taylor instabilities in the surrounding envelope. Other simulations of a collapsing mas-

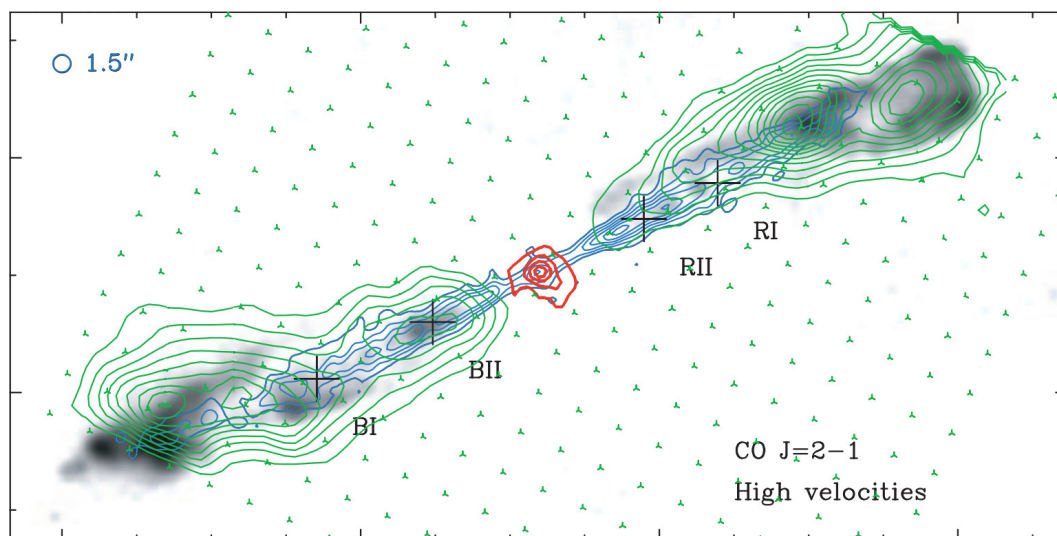


Figure 1.3: H₂ S(5) map (green contours) superimposed on the high velocity CO J = 2-1 map (blue contours) and close to systematic velocity CO J = 2-1 (red contours). Grayscale backgrounds are near-IR 2.12m H₂ images, figure taken from (Dionatos 2010)

sive core have been performed by Kuiper *et al.* (2011), using frequency dependent ray-traced stellar irradiation and gray FLD thermal radiation. This simulation also showed accretion continuing via a disc after the radiation become too intense for spherical accretion. However, they did not observe the unstable disc or radiation driven Rayleigh-Taylor instabilities observed by Krumholz & Matzner (2009). They attribute these differences to differing initial conditions (a $\rho \propto r^{-2}$ density profile in the Kupier paper as opposed to $\rho \propto r^{-1.5}$ in the Krumholz work) and their frequency dependent treatment of the starlight depositing its energy in a thicker shell of material than the gray FLD method.

As previously mentioned, some process is needed for the outward transport of angular momentum in order for accretion to proceed. This can be achieved via viscosity in the disc. It can be shown quite simply (Lodato 2008) that normal

molecular viscosity gives accretion rates many orders of magnitude too slow, and so some sort of anomalous viscosity is needed.

1.3.1 The α disc

Rather than determine exactly what causes this viscosity Shakura & Sunyaev (1973) parameterised the viscosity as

$$\nu = \alpha c_s h, \quad (1.7)$$

where h is the scale height of the disc ($\sim c_s/\Omega$), c_s is the gas sound speed, Ω is the angular speed of the disc and α is a numerical parameter setting the magnitude of the anomalous viscosity and has a value ≤ 1 . In a geometrically thin Keplerian disc the evolution of the mass surface density (Σ) is governed by

$$\frac{\partial \Sigma}{\partial t} = \frac{3}{R} \frac{\partial}{\partial R} \left(R^{1/2} \frac{\partial}{\partial R} (\nu R^{1/2} \Sigma) \right). \quad (1.8)$$

In a steady state accretion disc the product of ν and Σ is constant and so equation 1.8 can be reduced to give the mass transport rate through the disc,

$$\dot{M} = 3\pi\alpha c_s^2 \Omega^{-1} \Sigma, \quad (1.9)$$

(see Lynden-Bell & Pringle 1974; Hartmann *et al.* 1998; Balbus & Papaloizou 1999). The two main contenders for the cause of this anomalous viscosity are MHD instabilities (chiefly the magneto-rotational instability (MRI) - see Balbus & Hawley 1991) and gravitational instabilities (GIs). The MRI instability is caused by the differential rotation of a Keplerian disc in which the magnetic

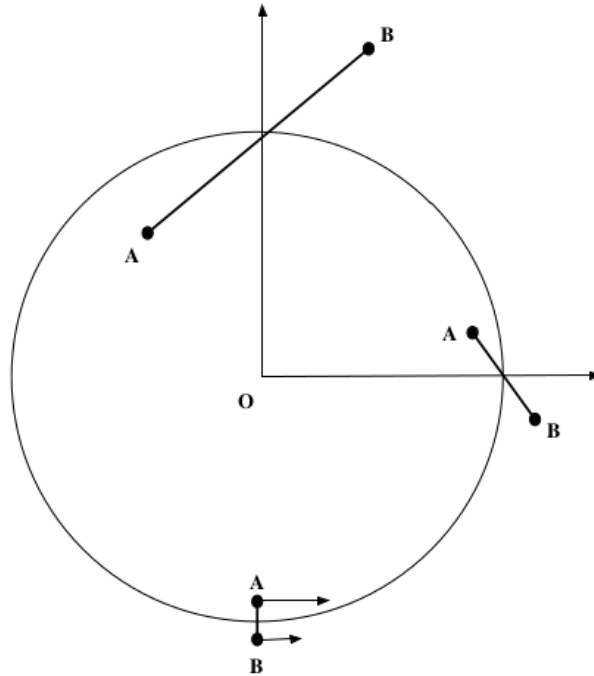


Figure 1.4: A sketch illustrating the geometry leading to the MRI. Two fluid elements A and B are connected by a magnetic field line. Due to differential rotation, the field line stretches and magnetic tension leads to a transfer of angular momentum from A to B causing A to sink further inwards and B to move further outwards, further stretching the field line and leading to a runaway evolution (reproduced from Lodato 2008).

flux is still frozen to the gas. Consider two adjacent fluid elements at the same azimuth connected by a magnetic field line. The inner element orbits faster than the outer. The resulting tension in the magnetic field will be felt as a drag on the inner element and an accelerating force on the outer one, causing angular momentum to be transported outwards (see Figure 1.4).

Gravitational instabilities are another possible source of anomalous viscosity and are the focus of chapter 3 (though the magneto-rotational instability is thought to be important later in the disc's evolution). Regardless of the source of the viscosity, if the accretion rate stays constant we can specify a value for the

viscosity to give the correct accretion rate. This is the so-called α -disc model.

1.3.2 Gravitational instability

If circumstellar discs continue to grow in mass through taking in more mass from the parent core than they feed onto the protostar then they will eventually become massive enough that the disc's own gravity becomes significant. This can be seen as a modification of the Jeans instability so that it is applicable to a rotating frame, where in addition to pressure providing support against gravitational collapse there is also centrifugal support. In order to determine when the disc's own gravity becomes important Toomre (1964) showed that the dispersion relation for perturbations in a geometrically thin disc is of the form of a quadratic equation in k (equation 1.10)

$$\omega^2 = c_s^2 k^2 - 2\pi G \Sigma |k| + \kappa^2 \quad (1.10)$$

Where Σ is the surface density of the disc, c_s is the sound speed and κ is the epicyclic frequency, the frequency of oscillations for small perturbations from circular orbits (equation 1.11), for Keplerian rotation it is equal to the disc rotation speed Ω .

$$\kappa^2 = \frac{1}{r^3} \frac{d(r^4 \Omega^2)}{dr} \quad (1.11)$$

This gives imaginary values for ω , and therefore instabilities, when the Toomre

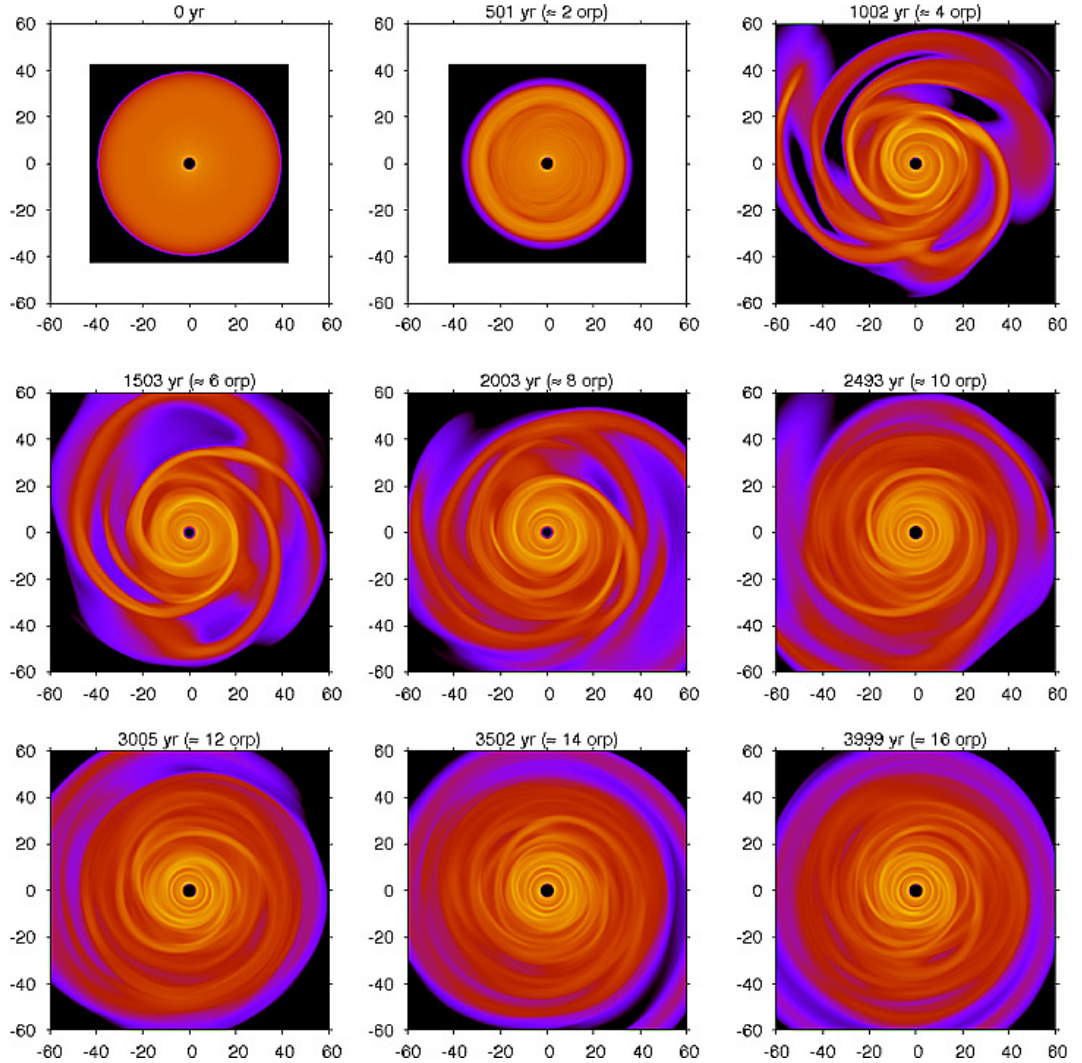


Figure 1.5: Snapshots from a simulation of a circumstellar disc becoming gravitationally unstable from Boley *et al.* (2007a)

stability parameter Q is less than 1,

$$Q = \frac{c_s \kappa}{\pi G \Sigma}. \quad (1.12)$$

These growing perturbations are smeared out by the differential rotation of the disc and result in spiral arms.

Numerical models of 3D discs which are not geometrically thin show that the instability can set in when $Q \lesssim 1.6$ (Durisen *et al.* 2007).

1.3.3 Radiative disc winds

In the high mass regime of star formation, radiation pressure has significant effects on the dynamics of the system. There are two main sources of opacity that the radiation can provide a force against. One source is dust, which provides very large optical depths in the visible and UV spectrum where the peak of emission from a MYSO will be, but is destroyed at high temperatures. The second source is atomic and ionic transition lines which can provide a source of optical depth even in gas totally free of dust. The study of radiation pressure acting on lines rather than dust particles has its origin in the modeling of stellar winds from more evolved massive stars. The model originally proposed by Castor, Abbott & Klein (1975, hereafter referred to as CAK) uses the Sobolev optical depth (equation 1.13) as the basis for the calculation of a line mediated radiation force.

$$\tau = \kappa_{C_s} \left| \frac{dv}{dr} \right|^{-1} \quad (1.13)$$

In the Sobolev approximation the width of the line is assumed to be small compared to the velocity gradient of the wind. This allows us to treat the line profile as a delta-function and the corresponding optical depth as a step function. In this case the optical depth is purely local. At the frequency of the absorbing point, $\nu_0(1 + v/c)$, the optical depth is zero closer to the source and constant further away. In the 1 dimensional case, as with the spherically symmetric wind from a star, this approximation is valid so long as the density and velocity gradient

do not change significantly over a few Sobolev lengths (\mathcal{L}) where:

$$\mathcal{L} = \frac{v_g}{dv/dl} \quad (1.14)$$

and v_g is the Gaussian width of the line expressed in velocity units.

In CAK the radiation force used to fit observational data for stellar winds was calculated using a sum over C⁺⁺ line strengths and they parameterise the resulting force as a function of an optical depth parameter t in the form:

$$F_l = F_e k t^{-\alpha} \quad (1.15)$$

$$t = \sigma_e \rho c_s \left| \frac{dv}{dl} \right|^{-1} \quad (1.16)$$

where F_e is the radiation force from electron scattering alone, t is an optical depth parameter dependent upon the local density, thermal velocity and velocity gradient along the line of sight from the luminosity source, and σ_e is the Thompson scattering cross-section. k and α are co-efficients dependent upon the ensemble of lines used to calculate the driving force. Physically, the k and α parameters are related to the average line strength and the ratio of force coming from optically thick to thin lines. Calculations of k and α using a realistic sum of lines of the elements up to zinc and ionizations up to 5+ were done by Abbott (1982) and the resulting values are used in this work.

Using this parameterisation of the line driving force, Proga *et al.* (1998) investigated the launching of a wind driven from the surface of a geometrically thin disc. They found that the wind could be either steady state or time dependent

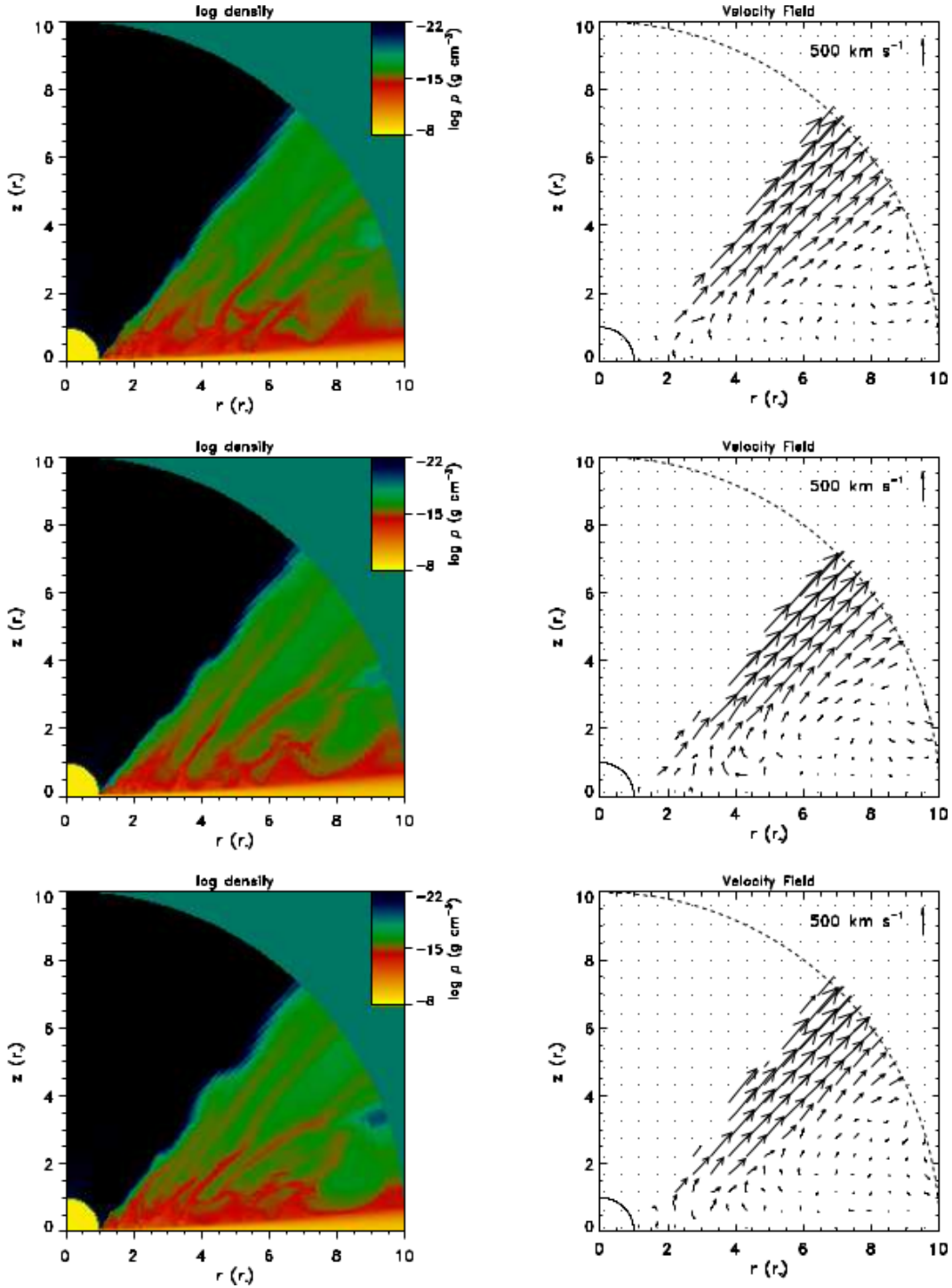


Figure 1.6: Density (left) and velocity (right) distributions of line mediated, radiatively driven disc winds. The top middle and bottom are different time snapshots of a single model of Drew *et al.* (1998) which shows time varying structure.

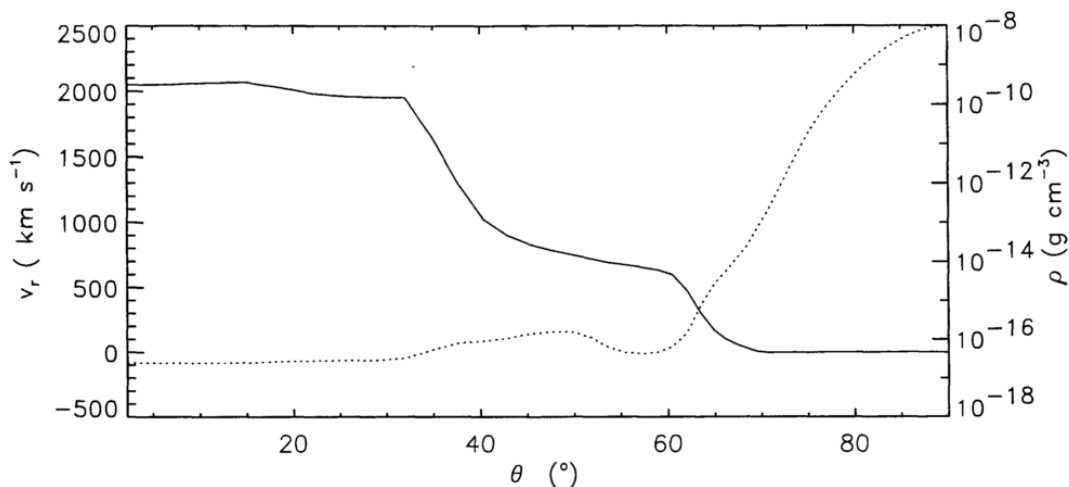


Figure 1.7: The radial velocity (left axis, solid line) and density (right axis, dotted line) of the radiatively driven disc wind simulated by Drew *et al.* (1998). The flow can be seen to split into three parts: a high velocity low density wind at latitudes $<35^\circ$, a static disc with a roughly Gaussian density distribution at latitudes $>65^\circ$ and a low velocity high density wind between these.

depending on the ratio of star and disc luminosity. A brighter central source tended to ‘organise’ the wind into a steady state. Using this model Proga *et al.* were able to reproduce the mass loss rates inferred in cataclysmic variable systems as well as the same general morphology of the outflow (dense slow equatorial wind, fast rarefied polar wind). Drew *et al.* (1998) applied this model to a MYSO with an accretion disc feeding a $10M_\odot$ protostar at a rate of $10^{-6}M_\odot \text{ yr}^{-1}$. These simulations show similar disc wind morphologies to the steady state solutions in Proga *et al.* (1998) again featuring a fast rare polar flow and a dense slower equatorial flow (see figures 1.6 and 1.7)

Ionised disc winds have been tentatively detected around S140 IRS 1 (Hoare 2006). Observations of the source show a dusty disc at millimetre wavelengths (Maud *et al.* 2013), a similarly aligned but more extended ionised wind at 5/GHz (bremsstrahlung emission), and perpendicular to these, a near-IR reflection nebula

showing the excavated cavity from a polar outflow (figure 1.8). The 5/GHz emission perpendicular to the outflow and aligned with, but more extended than, the disc has been interpreted as an ionised wind being driven from the surface of the disc. That it shows time varying structure but not proper motion (Hoare 2006) is consistent with the fact that line driven radiative winds are expected to be unstable.

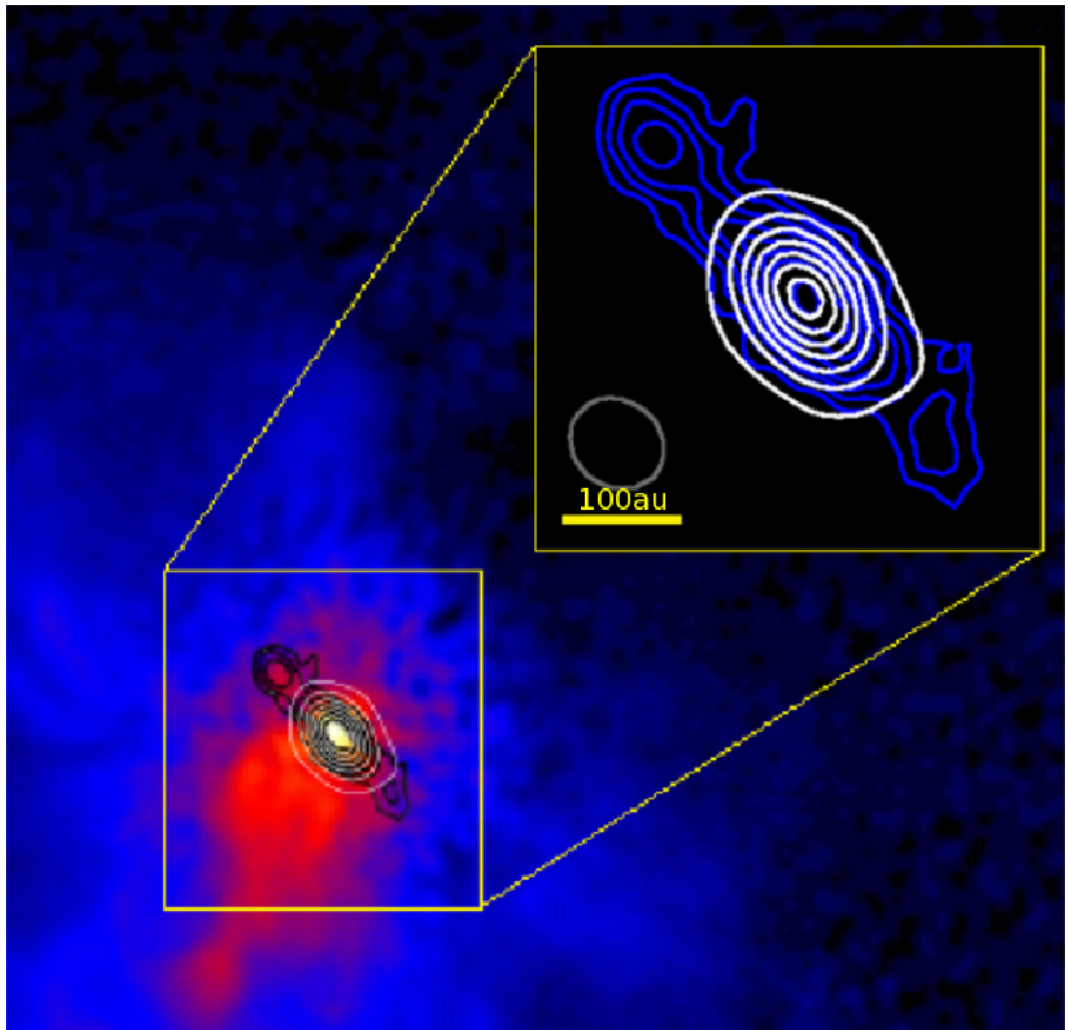


Figure 1.8: The MYSO S140 IRS 1. The White contours shows millimetre dust emission tracing a disc, the blue contours trace 5GHz radio free-free emission showing an ionized disc wind and the colourscale is near-IR reflected light from an outflow cavity. Figure reproduced from Maud *et al.* (2013).

Chapter 2

Numerical Methods

In this chapter I present the Numerical methods used in the remaining chapters of this thesis. Firstly I outline the basic theory of the transfer of radiation through matter with particular focus on the transfer of atomic and molecular line radiation. Secondly I give an overview of the LIME program which I used in order to numerically solve the radiative transfer equations in a gravitationally unstable disc (see chapter 3) and describe the changes I made to it. Finally I outline the equations of hydrodynamics and give a brief overview of their discretisation onto a Eulerian grid using the finite volume method.

2.1 Radiative transfer

2.1.1 Theory

Radiative transfer is the study of how light propagates through matter and can be entirely described by a single equation:

$$\frac{dI_\nu}{ds} = -\alpha_\nu I_\nu + j_\nu, \quad (2.1)$$

where I_ν is the specific intensity and α_ν and j_ν are the absorption and emission coefficients, all for a given frequency. The change in intensity along a line of sight is the difference between the emission coefficient and the product of the absorption coefficient and the intensity. So, in order to know the intensity of light leaving an element of matter, we need to know the intensity, emission and absorption coefficients at each point along the line of sight.

For continuum radiation the absorption and emission coefficients can be dependent upon the local density of matter, the temperature, the composition of dust grains in the material and the ionisation state of metals in the gas (Rybicki & Lightman 1986), but they are not directly dependent upon the intensity of the light propagating through it. For the radiation due to atomic and molecular lines, however, both the absorption and emission coefficients are affected by the intensity of radiation. Incident photons upon an atom or molecule can both excite it to a higher state or stimulate an emission of a photon as it relaxes to a lower state. Both of these effects change that atom's or molecule's contribution to the emission and absorption coefficient. This coupling of the absorption and emission coefficients to the intensity means that an analytic solution to equation

2.1 cannot be obtained and we must resort to numerical methods to solve for the intensity.

In the simplest approximation, one assumes that an atom or molecule has only two significantly populated energy levels. The upper level and the lower one are separated by an energy gap ΔE and have populations of n_u and n_l respectively. The absorption (α_ν) and emission (j_ν) coefficients are related to the Einstein coefficients and the level populations by

$$j_\nu = \frac{h\nu_0}{4\pi} n_u A_{ul} \phi(\nu), \quad (2.2)$$

$$\alpha_\nu = \frac{h\nu}{4\pi} (n_l B_{lu} - n_u B_{ul}) \phi(\nu), \quad (2.3)$$

where A and B are the Einstein coefficients, $\phi(\nu)$ is the normalised probability distribution for a photon of frequency ν to excite/deexcite the molecule, $\Delta E = h\nu_0$ is the energy separation of the energy levels and ν_0 is the frequency of the photon emitted from the transition (van der Tak *et al.* 2007). In steady state equilibrium, the numbers of upwards and downwards transitions are equal and so the level populations satisfy

$$\gamma_{lu} n_{H_2} n_l + B_{lu} \bar{J} n_l = \gamma_{ul} n_{H_2} n_u + B_{ul} \bar{J} n_u + A_{ul} n_u, \quad (2.4)$$

where γ is the collisional (de)excitational coefficient and \bar{J} is related to the mean intensity of the radiation J_ν by

$$\bar{J} \equiv \int_0^\infty J_\nu \phi(\nu) d\nu, \quad (2.5)$$

and J_ν is related to the specific intensity by

$$J_\nu \equiv \frac{1}{4\pi} \oint I_\nu d\Omega. \quad (2.6)$$

In the case of isotropic emission and absorption, which we are assuming here, $J_\nu = I_\nu$.

If the density is high enough that radiative transitions are negligible compared to collisional ones, then $n_u/n_l = \gamma_{lu}/\gamma_{ul}$ and the population distribution is thermalised (Stahler & Palla 2004) resulting in the Boltzmann distribution of particles:

$$\frac{n_u}{n_l} = \frac{g_u}{g_l} \exp\left(\frac{-\Delta E}{k_B T_{kin}}\right), \quad (2.7)$$

where g_i is the degeneracy of the i th level, k_B is the Boltzmann constant and T_{kin} is the kinetic temperature.

When equation 2.7 applies, the gas is in local thermodynamic equilibrium (LTE), and the level populations can be calculated without prior knowledge of the radiation field. The appropriateness of the approximation depends on the ratio of the density of the main collision partner (in molecular clouds this is H_2) to the critical density. In the optically thin limit, the critical density is given by equation 2.8.

$$n_{crit} = A_{ul}/\gamma_{ul}. \quad (2.8)$$

If $n_{H_2} \gg n_{crit}$, then we can say that the gas is in LTE for this transition. If this is not the case then the radiative transfer equation is coupled to the level population equation with too many free variables to solve analytically. In this case

T_{kin} is replaced by T_{ex} in equation 2.7. T_{ex} is the excitation temperature and is a measure of the relative populations of the upper and lower levels and it reduces to the kinetic temperature when $n \gg n_{crit}$ and the radiation temperature when $n \ll n_{crit}$. In the non-LTE case computer programs are used to solve these equations numerically for multi-level systems.

If the optical depth is non-negligible then we need to take into account the reabsorption of emitted photons. We do this by introducing a probability β that an emitted photon escapes the region of optically thick gas.

$$\beta(\mathbf{x}) \equiv \frac{1}{4\pi} \oint \int e^{-\tau_\nu(\mathbf{x}, \mathbf{n})} \phi(\nu) d\nu d\Omega, \quad (2.9)$$

where $\tau_\nu(\mathbf{x}, \mathbf{n})$ is the optical depth at position \mathbf{x} in the direction \mathbf{n} . Given that the three possible outcomes for an emitted photon are 1) absorption then collisional de-excitation 2) absorption then re-emission and 3) escape, we note that the number of photons absorbed minus the number produced by stimulated emission must equal the number of photons emitted that do not escape from the gas. We can then equate the number of net absorptions to the number of photons which do not escape:

$$(n_l B_{lu} - n_u B_{ul}) \bar{J} = n_u (1 - \beta) A_{ul}. \quad (2.10)$$

We can use this to re-write equation 2.4 as

$$\gamma_{lu} n_{H_2} = (\gamma_{ul} n_{H_2} + \beta A_{ul}) n_u, \quad (2.11)$$

showing that absorptions are effectively reducing radiative de-excitation by a factor of β . As $n_{crit} \propto A_{ul}$ we can see that having non-negligible optical depth

decreases the critical density by a factor equal to the escape probability of a photon (Klessen & Glover 2014).

2.1.2 LIME

The radiative transfer program used to solve these equations is LIME (Line Modelling Engine; Brinch & Hogerheijde 2011), which calculates line intensities based on a weighted sample of randomly chosen points in a continuous 3D model. The method of selecting these points is given in section 2.1.3. At each point, the density of the main collision partner (H_2), gas and dust temperatures, velocity, molecular abundances and unresolved turbulent velocity are specified. These points are then smoothed by Lloyd’s algorithm (Lloyd 1982). This works by repeatedly moving each of the selected points to the centroids of their Voronoi cell (the volume of space closer to the point than any other point) then recomputing the Voronoi cells. Smoothing the point distribution in this way minimises the local variation in separation between points whilst preserving the average point density. These points are then connected by Delaunay triangulation (see figure 2.1). In three dimensions this is the set of points and connections such that for any four points connected in a tetrahedron, the sphere enclosing these points contains no other point. This has the effect of maximizing the sum of the smallest angle in each triangle of connected points, and therefore minimizing their irregularity. It is between the points connected by this method that photons are allowed to propagate (figure 2.2). The level populations of the selected molecules are calculated at each of these points from collisional and radiative (de)excitation and the local radiation field is calculated and propagated for the next iteration.

This is repeated 20 times with the populations of each level converging towards a single value. This number of iterations is sufficient for the signal to noise ratio of the level populations (defined as the number of atoms in a particular level divided by the standard deviation of the number of atoms in that level over the past 5 iterations as in Brinch & Hogerheijde 2011) to exceed 1000 for 99% of the points, ensuring that the simulation has converged on a stable level population. After 20 iterations the model is ray-traced in order to produce synthetic brightness maps.

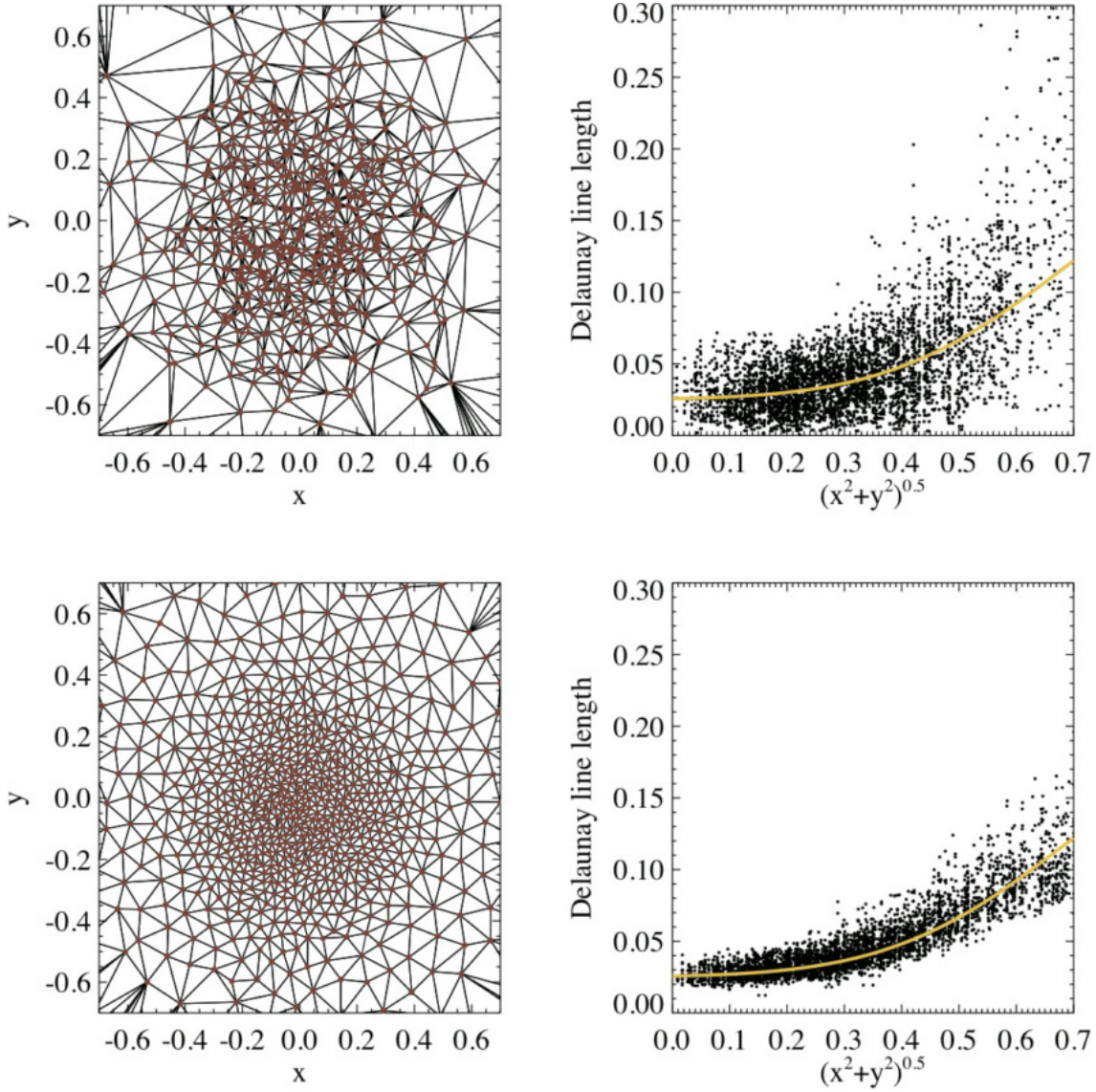


Figure 2.1: Delaunay grids based on the same Gaussian density distribution before (top) and after (bottom) smoothing by Lloyd's algorithm. The right hand column shows the length of the Delaunay edges as a function of radius. The yellow lines are a Gaussian that describes the underlying density distribution, from Brinch & Hogerheijde (2011).

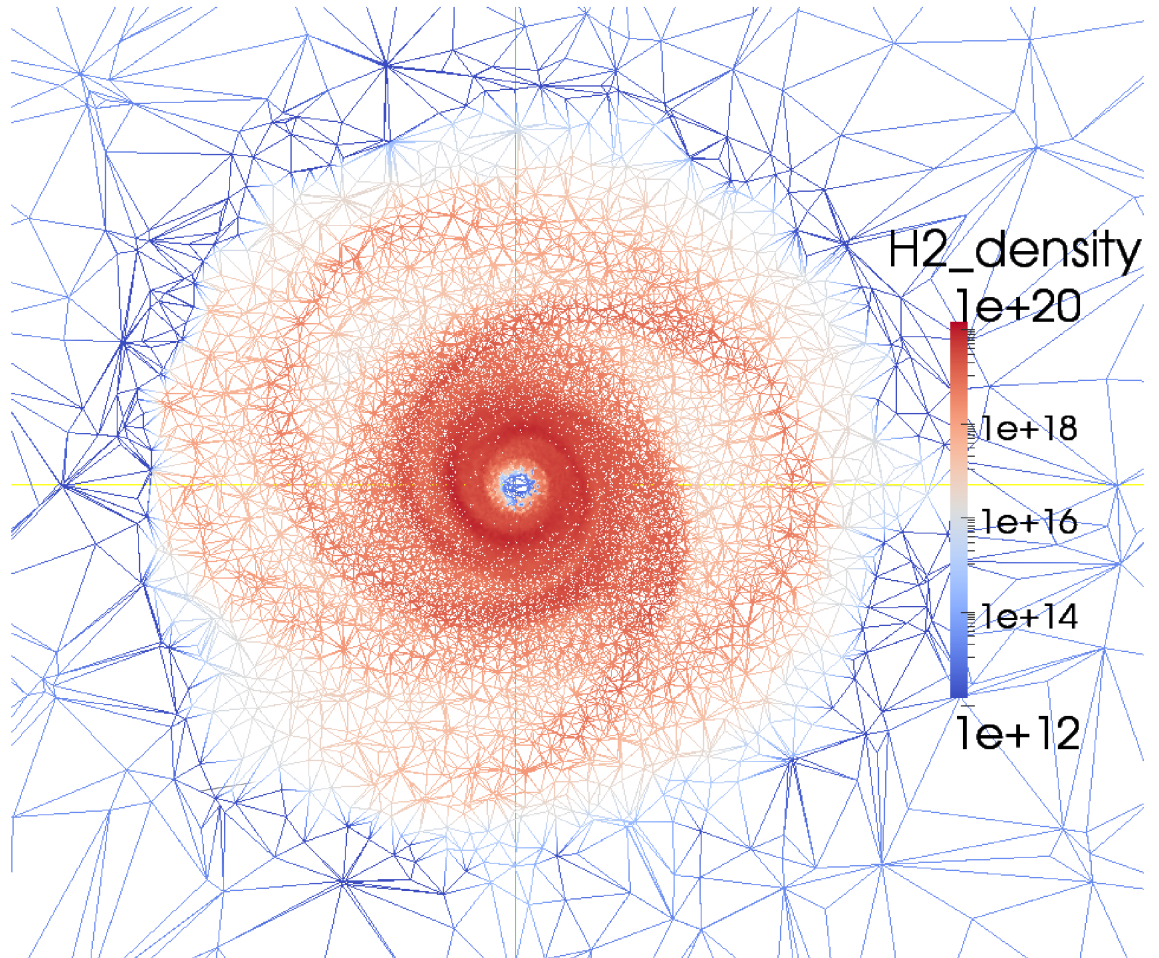


Figure 2.2: A plot of the points selected by the gridding process and the paths down which photons can propagate for points in the central r, θ plane. The points are colour coded by the density distribution (in m^{-3} , as used in LIME) and are more concentrated at small radii and in the most dense regions. The circular high density region with spiral arms in the centre is the disc model and is 128 au in diameter.

2.1.3 Grid construction

In order to construct the grid for the gravitationally unstable disc models, candidate points are randomly selected from the volume to be simulated. These candidate points are associated with values of the H_2 number density and the number density of the molecular species being simulated at the position of the point in the underlying model. These are then compared against the H_2 and molecular density of a reference point in order to decide if they will be included in the grid.

Candidate grid points are selected at random in a cylindrical coordinate system that is linearly spaced in z and θ and logarithmically spaced in r . For each point to be selected, a random number α is drawn from the semi-open set $[0, 1)$ to be used as a threshold. After selection of random coordinates, the hydrogen density and molecular density at the candidate point (n and m , respectively) are compared against the densities of a reference point on the inner edge of the disc (n_0 and m_0). If $\alpha < \left(\frac{n}{n_0}\right)^{0.3}$ or $\alpha < \left(\frac{m}{m_0}\right)^{0.3}$ then the point is selected for use. Otherwise another (r, θ, z) co-ordinate is selected and it becomes the candidate point. 20% of these selected points are forced to be at radii greater than $\sqrt{R_{min}R_{max}}$ ($\sim 200 au$ for the gravitationally unstable disc model, where R_{min} and R_{max} are the inner and outer radii of the model) in order to stop too many of the selected points clustering in the high density disc and leaving the envelope under sampled. In addition to this method of selection, 5% of the points are linearly distributed in x , y and z with no bias with regards to density or abundance. This provides a minimum level of sampling for the large low density regions in the outer regions of the simulated volume. See figure 2.3 for an example of the

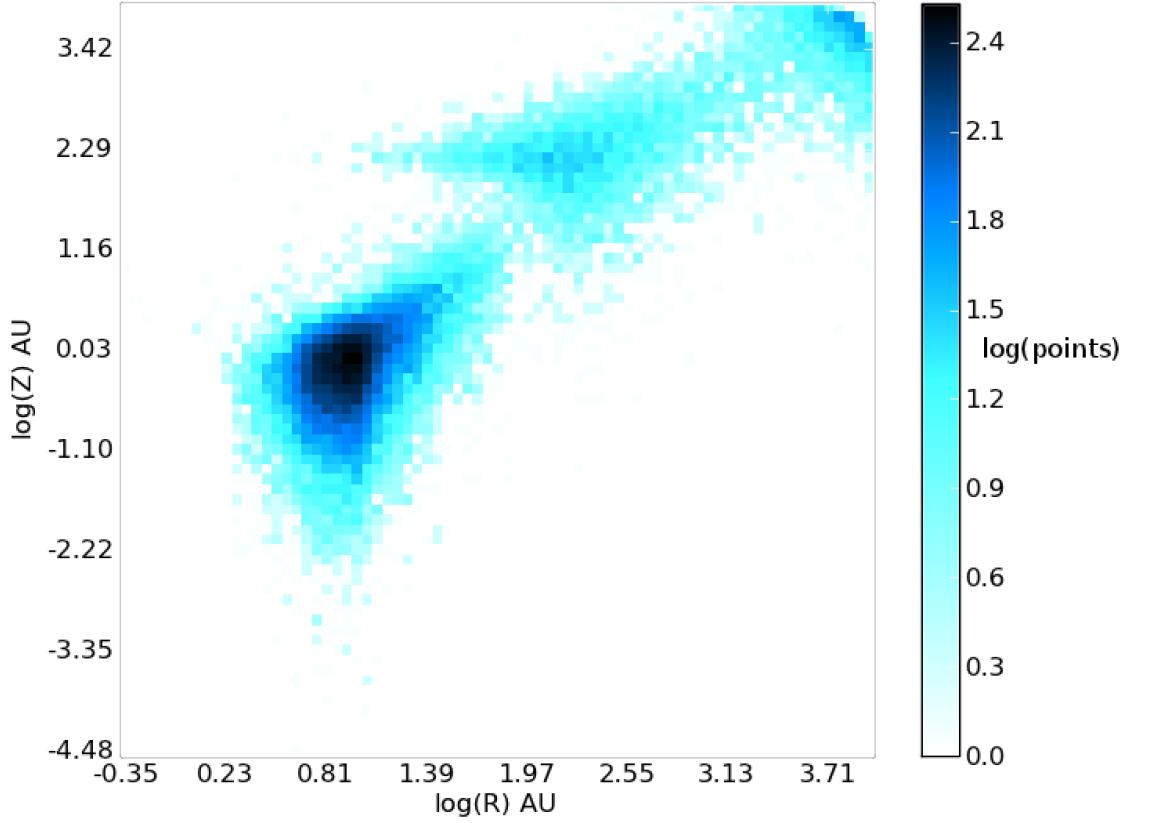


Figure 2.3: A 2D histogram of the point distribution throughout the model. The disc and envelope can be seen as two separate entities which have to be sampled using different point distributions.

points distribution in (r, z) . The function comparing the candidate point to the reference point and the candidate point distribution were selected empirically to sample all scales while ensuring that the majority of points are located in the inner disc where the density is higher.

This method of selecting points is different to the default methods in LIME where points can only be distributed linearly in x, y, z or logarithmically in r and linearly in θ and ϕ , and the only selection criterion is $\alpha < \left(\frac{n}{n_0}\right)^{0.5}$. As the systems under consideration are broadly axis-symmetric (excepting the spiral arms in the

gravitationally unstable discs) a cylindrical co-ordinate system is the most natural to select points in. Also, given the large variation in molecular abundance as a function of position, basing the selection criterion on that as well as H_2 density allows points to be focused in the regions where the molecules being simulated are.

Increasing the number of points in the model increases the resolution of the output image (figure 2.4). However calculating the molecular level populations using N points has a computational cost scaling as N^2 , as each additional point needs to have its own level population calculated and also emits radiation which needs to be accounted for in all the other points' level calculations. As can be seen from figure 2.4 the increase in image fidelity appears to tail off after 20,000 points. In the models being used here a total of 24,000 points were used and the simulation ran ten times with different seeds to the random number generator used to create the grid. The output ray-traced images for these 10 runs were then averaged together in order to create the final image (figure 2.5).

Table 2.1 gives the parameters used in the grid construction for LIME. The values marked with an asterisk for the disc-wind model are typical values, as the actual value varies from model to model.

Table 2.1: LIME gridding parameters

Parameter	GI disc model	Disc-wind model
n_0 (m^{-3})	10^{19}	* 10^{17}
m_0 (m^{-3})	5×10^{10} (for C^{17}O)	* 3×10^{11} (for C^+)
R_{min}	1.5 au	0.95 R_*
R_{max}	0.1 pc	300 au

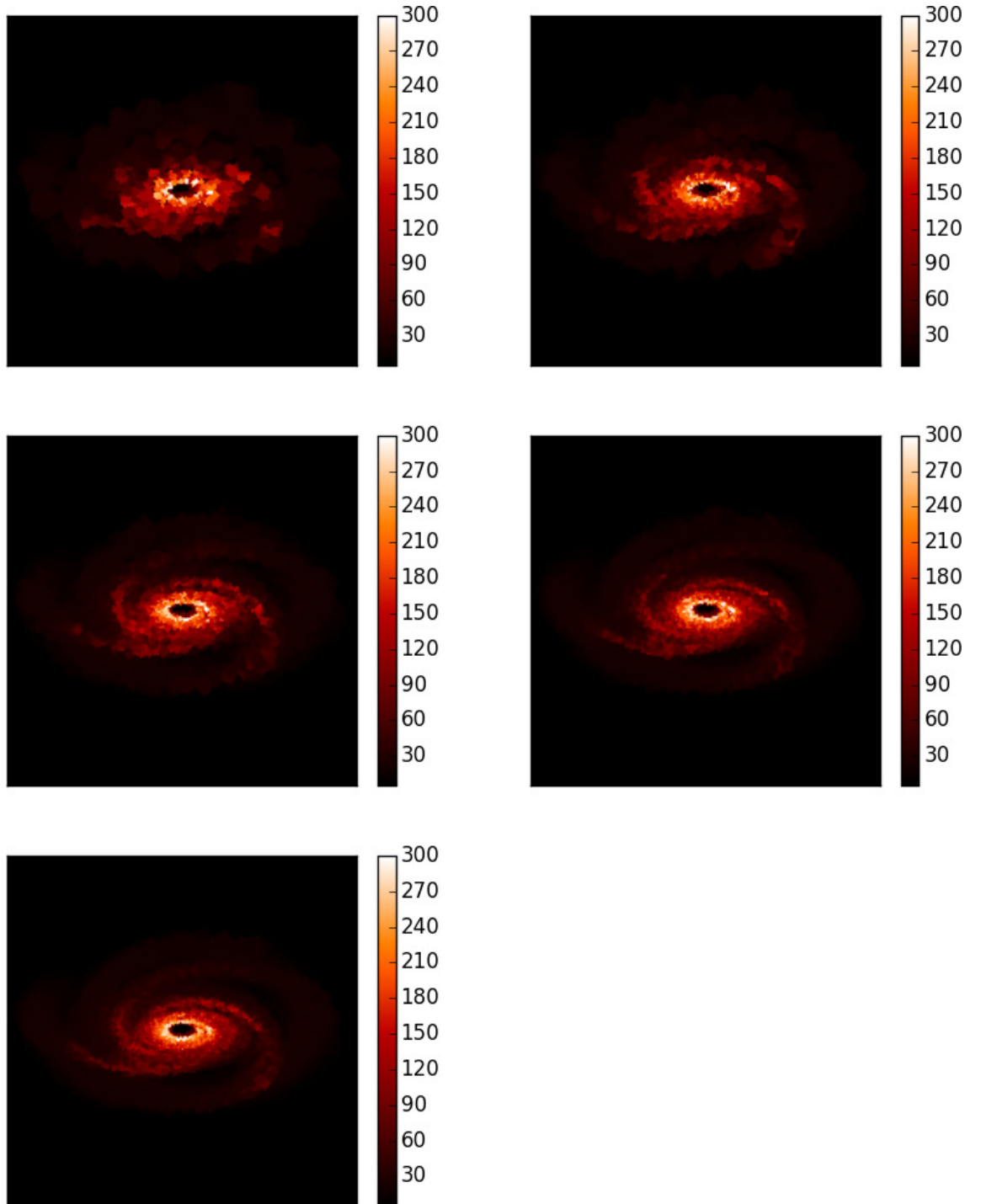


Figure 2.4: 300GHz output images from LIME using 4, 8, 16, 24 and 32 thousand model points. The colour scale shows the surface brightness of the emission in Kelvin.

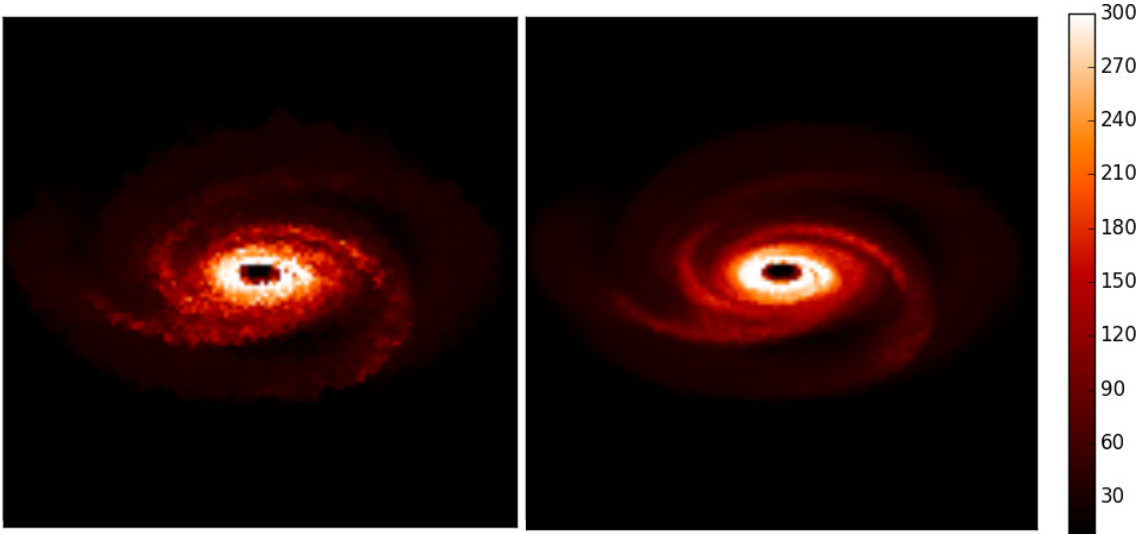


Figure 2.5: **Left:** The output of a single radiative transfer simulation, with artefacts due to finite gridding **Right:** A 300 GHz continuum image of the model, created from the average of ten LIME runs. The colour scale shows the surface brightness in Kelvin.

2.2 Hydrodynamics

The hydrodynamic simulations presented in chapter 4 were carried out using the (magneto-)hydrodynamics code *MG*. This section outlines the basic equations of hydrodynamics with an emphasis on their numerical implementation in *MG*.

2.2.1 Equations of Hydrodynamics

The equations governing the flow of compressible fluids are Euler’s equations (equation 2.12 - 2.14) for an inviscid flow or the Navier-Stokes equations for a viscous flow. These equations can be used to describe the changes in state at either fixed points in space or in a reference frame co-moving with the mass of the fluid, these are referred to as Eulerian and Lagrangian formulations. In this section I deal only with the Eulerian formulation of the hydrodynamic equations

as *MG* uses a Eulerian formulation. In Cartesian co-ordinates the Euler equations are the continuity equation:

$$\frac{\partial \rho}{\partial t} + \nabla \cdot (\rho \mathbf{u}) = 0, \quad (2.12)$$

the momentum conservation equations:

$$\frac{\partial \rho u}{\partial t} + \nabla \cdot (\rho u \mathbf{u}) + \frac{\partial P}{\partial x} = \rho a_x, \quad (2.13a)$$

$$\frac{\partial \rho v}{\partial t} + \nabla \cdot (\rho v \mathbf{u}) + \frac{\partial P}{\partial y} = \rho a_y, \quad (2.13b)$$

$$\frac{\partial \rho w}{\partial t} + \nabla \cdot (\rho w \mathbf{u}) + \frac{\partial P}{\partial z} = \rho a_z, \quad (2.13c)$$

and the total energy equation:

$$\frac{\partial e}{\partial t} + \nabla \cdot ((e + P)\mathbf{u}) = \rho (\mathbf{a} \cdot \mathbf{u}), \quad (2.14)$$

where ρ is the mass density, \mathbf{u} is the velocity (with components u , v and w), P is the pressure, \mathbf{a} is the acceleration due to non-hydrodynamic forces (i.e. gravity and radiation pressure), e is the total (thermal + kinetic) energy given by the equation of state:

$$e = \frac{\rho \mathbf{u} \cdot \mathbf{u}}{2} + \frac{P}{\gamma - 1}. \quad (2.15)$$

and γ is the adiabatic index of the gas and is equal to 5/3 for an ideal monoatomic gas.

In order to obtain solutions to these equations they must be discretised and

solved numerically. One method of performing this discretisation is the finite-volume method. In this approximation the volume over which the calculations are to be performed is divided into cells with single values for the conserved quantities (density, momentum, energy and advected scalars) and the hydrodynamic equations (equations. 2.12 - 2.14) are integrated over the volume of the cells. Taking the mass conservation equation (2.12) and integrating it over a cell we get:

$$\iiint_V \frac{\partial \rho}{\partial t} dV + \iiint_V \nabla \cdot (\rho \mathbf{u}) dV = 0. \quad (2.16)$$

This can be re-written using Gauss's theorem as

$$\frac{\partial \rho V}{\partial t} + \oint_A \rho (\mathbf{u} \cdot \hat{\mathbf{n}}) dA = \frac{\partial \rho V}{\partial t} + F(\rho) = 0, \quad (2.17)$$

where V is the cell volume and A is the area bounding the cell. This states that over a time interval dt the change in mass of a cell is equal to the net mass flux through its surface ($F(\rho)$). As the mass that flows out of one cell is flowing into another we can see that this formulation of the mass equation is conservative (except at the edges of the simulated region where, depending on the choice of boundary conditions, mass maybe be permitted to flow into or out of the system).

If time is split into discrete steps we can calculate the mass in a cell at the next step using the current state of the cell with:

$$\rho_{ijk}^{n+1} = \rho_{ijk}^n - \int_{t_n}^{t_{n+1}} F_{ijk}(\rho) dt, \quad (2.18)$$

where n is the index of the time step and i, j and k are the indices of the spatial

co-ordinates and are integers at cell centres. If we consider cubic cells with edges of length l and assume that the velocity is constant across the face of a cell then the total flux in the x direction is the difference between the fluxes of the left and right faces:

$$F_i(\rho) = F_{i-0.5}(\rho) - F_{i+0.5}(\rho) \quad (2.19)$$

and

$$F_{i\pm 0.5} = l^2 (\rho u)_{i\pm 0.5}. \quad (2.20)$$

In order to complete the discretisation of the equations the time integral of $F_i(\rho)$ needs to be replaced with an average value so that

$$\int_{t_n}^{t_{n+1}} F_i(\rho) dt = \Delta t \bar{F}_i(\rho). \quad (2.21)$$

This gives the final form of the mass advection step in the x direction

$$\rho_{ijk}^{n+1} = \rho_{ijk}^n + \frac{\Delta t}{l^3} (\bar{F}_{i-0.5}^n(\rho) - \bar{F}_{i+0.5}^n(\rho)). \quad (2.22)$$

Similarly the advection of momentum and energy are:

$$(\rho u)_{ijk}^{n+1} = (\rho u)_{ijk}^n + \frac{\Delta t}{l^3} (\bar{F}_{i-0.5}^n(\rho u) - \bar{F}_{i+0.5}^n(\rho u)), \quad (2.23a)$$

$$e_{ijk}^{n+1} = e_{ijk}^n + \frac{\Delta t}{l^3} (\bar{F}_{i-0.5}^n(e + P) - \bar{F}_{i+0.5}^n(e + P)). \quad (2.23b)$$

The average fluxes \bar{F} are calculated by solving the Riemann problem across each cell face.

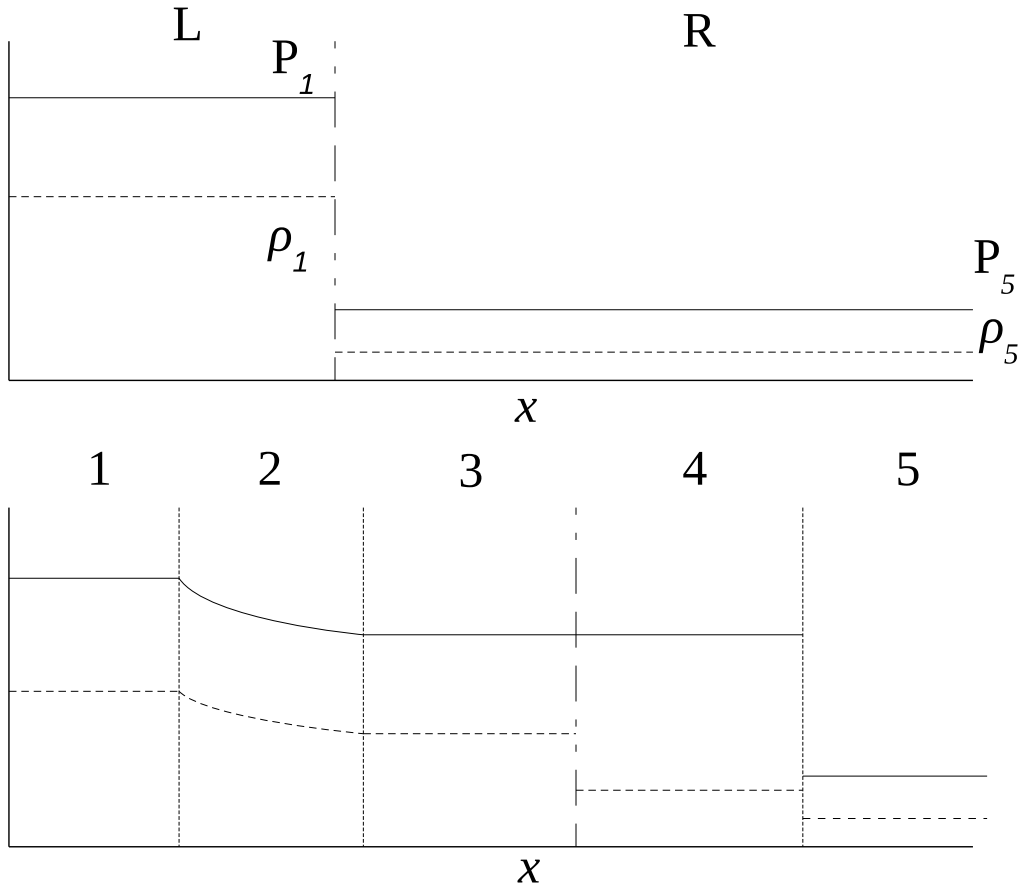


Figure 2.6: A shock tube before (top) and after (bottom) the partition between left and right sections is removed. In order to calculate the density, pressure and velocity, and therefore the mass flux, the Riemann problem is solved.

The Riemann problem is defined as follows: given P_1, ρ_1 and P_5, ρ_5 for two regions separated by an impermeable membrane (top panel of figure 2.6) find the P, ρ and v for the other three regions as functions of position and time (Bodenheimer *et al.* 2007). Using the fact that the flux of mass, momentum and total energy must be equal on both sides of a shock (the Rankine-Hugoniot conditions) and the fact that pressure and velocity are constant across the contact discontinuity,

ity between regions 3 and 4, a sequence of non-linear equations can be constructed and solved in order to calculate the flux across the cell boundary during the time step (Hawley *et al.* 1984). This method assumes that the conserved quantities are constant within cells (piece-wise constant spatial reconstitution) and is first order accurate. In order to improve on this *MG* uses a piece-wise linear fit, which gives second order accuracy at the expense of additional computational requirements. Piece-wise linear spatial reconstitution assumes that the conserved values in cells are averages over the cell and that the values vary linearly across them.

In order to solve the Riemann problem across a cell face, *MG* firstly calculates a linear approximation to the Riemann problem. Using equations 2.24 an approximation for the velocity and pressure over the contact discontinuity is calculated.

$$p_3 = \frac{C_R p_L + C_L p_R - C_R C_L (u_R - u_L)}{C_R + C_L}, \quad (2.24a)$$

$$u_3 = \frac{C_R u_R + C_L u_L - (p_R - p_L)}{C_R + C_L}. \quad (2.24b)$$

Here C is the product of the density and the sound speed ρc_s and the subscripts L and R refer to the left and right cells of the face. If the pressure calculated here differs from the pressures in the left and right cells by no more than 10% then these values for the pressure and velocity are used, if not then an iterative method is used to get an accurate pressure value. Once these values have been determined the fluxes are calculated using a piecewise linear method. This uses the average density of the upstream cell if the absolute value of u_3 is greater than

the sound speed in the upstream cell, if not then an interpolated value is used:

$$\rho = \frac{C_{\text{up}}\rho_{\text{up}}}{C_{\text{up}} \pm \rho_{\text{up}}(u_3 - u_{\text{up}})}, \quad (2.25)$$

where the subscript up denotes the value in the upstream cell and the \pm is $+$ if the upwind cell is on the left and $-$ if it is on the right.

The fluxes are calculated separately in each dimension by solving the Riemann problem across each face. After calculating all of the fluxes the conserved quantities are updated using the net flux into each cell.

2.2.2 Source terms

In equations 2.13 and 2.14 the right hand sides are non-zero. This represents a change in the total momentum and energy of the system due to non-hydrodynamic forces accelerating the gas and doing work on it. In the simulations presented in this thesis the force is composed of a gravitational term and a radiative term

$$\mathbf{a} = \sum \mathbf{a}_{\text{rad}} - \nabla\Phi. \quad (2.26)$$

$\nabla\Phi$ is the gradient of the gravitational potential and is assumed to be solely due to a single mass at the origin, while $\sum \mathbf{a}_{\text{rad}}$ is the vector sum of the accelerations from each radiation source included in the model.

In order to calculate \mathbf{a}_{rad} without ray-tracing the model at each time step and incurring significant computational costs, the radiation forces are based on the Sobolev optical depth approximation using the method for line driven winds outlined by CAK. As this method is purely local (relying only on density, temperature and velocity gradients) it removes the need for ray-tracing the model.

In this method the radiation force used is of the form

$$F_l = F_e k t^{-\alpha}, \quad (2.27)$$

$$t = \sigma_e \rho c_s \left| \frac{dv}{dl} \right|^{-1} \quad (2.28)$$

and F_e is the radiation force from electron scattering alone, t is an optical depth parameter dependent upon the local density, thermal velocity and velocity gradient along the line of sight from the luminosity source and σ_e is the Thompson scattering cross-section. k and α are co-efficients dependent upon the ensemble of lines used to calculate the driving force and are taken from tabulated values in Abbott (1982). These are functions of both the effective temperature of the radiation doing the acceleration and the ionisation state of the gas.

In a 2D axis-symmetric system strict conservation of momentum is not possible as one of the quantities being followed is radial momentum, which is not a conserved quantity. In order to compensate for this a geometric source term is included for the radial momentum so that momentum conservation equations (2.13) in 2D cylindrical co-ordinates become:

$$\frac{\partial \rho u_R}{\partial t} + \nabla \cdot (\rho u_R \mathbf{u}) + \frac{\partial P}{\partial R} = \rho a_R + \frac{P}{R}, \quad (2.29a)$$

$$\frac{\partial \rho u_z}{\partial t} + \nabla \cdot (\rho u_z \mathbf{u}) + \frac{\partial P}{\partial z} = \rho a_z, \quad (2.29b)$$

where R is the cylindrical radius (Falle 1991).

2.2.3 Adaptive mesh refinement

In many astrophysical problems there are large regions of smoothly changing fluid variables bordered by shocks and/or turbulent regions. In these cases the numerical resolution needed varies greatly one from one region to another and in order to maximize the accuracy for a given amount of computational time the grid should be finer where high resolution is needed and coarser elsewhere. This could be done by having multiple static grids if it is known in advance where the higher resolution will be needed and that it will not move. However in general this is not the case and an adaptive method for increasing and decreasing the resolution is desirable.

Adaptive mesh refinement (AMR) uses a hierarchy of grids with each level containing cells a factor of 2 smaller in each direction and the two lowest resolution grids covering the entire simulated volume. For each of the cells in a level the values of the conserved variables are compared against the interpolated value from the level above. If the difference between the two is greater than a defined threshold (defaulting to 1%) then the cell is refined to the next level down. Finally a diffusion operation is applied to the refinement criteria in order to prevent steep jumps in the resolution which would interfere with the interpolation routine. An example of an AMR grid with five levels of refinement can be seen in figure 2.7.

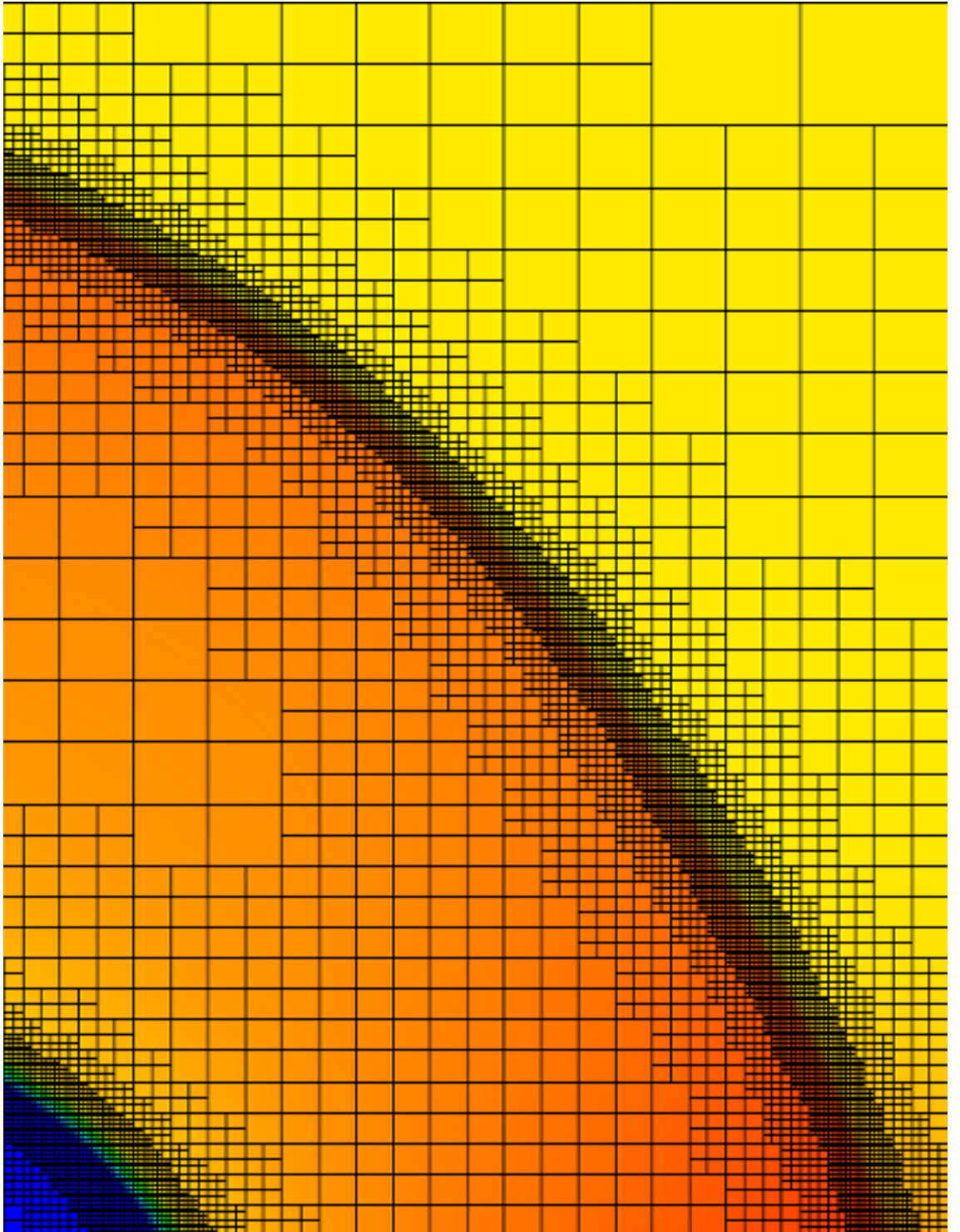


Figure 2.7: An example of an AMR grid using five levels of refinement. The colour scale shows the density. Regions of large density gradients are refined to higher resolution.

Chapter 3

Simulated observations of gravitationally unstable young protoplanetary discs

3.1 Introduction

Currently few observations constrain the formation and early evolution of protoplanetary discs around solar-type and low-mass protostars, despite the rapidly growing list of theoretical models of the dynamical evolution of star forming dense cores (e.g. Krasnopolsky *et al.* 2011; Machida *et al.* 2011b; Braiding & Wardle 2012; Joos *et al.* 2013). The reason for this is that young protostars are surrounded by thick envelopes and power energetic outflows. Thus, observations of the young discs, predicted to have sizes of about 100 au and masses as large as 10 percent the original core mass (e.g. Joos *et al.* 2012; Hayfield *et al.* 2011b; Machida *et al.* 2011b), are challenging. Sensitive interferometers are needed to

achieve high angular resolution and spatially/spectrally disentangle the various disc, envelope and outflow components as well as to filter out the extended emission tracing the envelope material.

After the pioneering work of, e.g., Chandler *et al.* (1995); Brown *et al.* (2000); Looney *et al.* (2000), recent interferometric observations have discovered compact embedded discs in a sample of Class 0 sources (as defined by André *et al.* 1999), with masses between 0.4 and $>1 M_{\odot}$ (Jørgensen *et al.* 2007, 2009; Enoch *et al.* 2011). A 130 au disc was revealed in NH_3 emission toward a Class 0 source in Perseus, with the Jansky Very Large Array (JVLA) (Choi *et al.* 2007). Pineda *et al.* (2012) observed methyl formate (HCOOCH_3) with the Atacama Large Millimetre/sub-millimetre Array (ALMA) and found evidence of rotation toward one of the proto-binary Class 0 sources embedded in IRAS 16293-2422. These observations are consistent with an almost edge-on disc. Persson *et al.* (2012) observed H_2^{18}O with ALMA toward the same source and found evidence of ~ 100 K excitation temperatures. Zapata *et al.* (2013) used ALMA to observe a disc of size ~ 50 au in the other Class 0 source in IRAS 16293-2422 and detected inverse P-Cygni profiles in HCN and CH_3OH which indicate infall towards the disc. When ALMA is completed spatially resolving these young discs will be possible. For the first time stringent constraints will be placed on the theoretical models mentioned previously.

Simulated observations of gravitationally unstable discs have already been performed to study the continuum emission, measure the structure and investigate possible fragmentation (Cossins *et al.* 2010; Ruge *et al.* 2013). Molecular line emission from massive discs has been simulated by Krumholz *et al.* (2007), who assumed local thermodynamic equilibrium (LTE). The focus of the work is on

the self-gravitating discs of Boley & Durisen (2008), in which episodic heating induced by spiral shocks is present. This may be a good representation of the earliest phases of protoplanetary discs and an alternative to the young “static” discs studied by, e.g. Visser *et al.* (2009, 2011). As shown by Ilee *et al.* (2011), hereafter I2011, the spiral shocks cause desorption of volatiles from the icy mantles of dust grains and trigger gas-phase chemical reactions with activation energies too high to occur in a quiescent disc. These processes produce clear chemical signatures of the disc dynamics. With the use of non-LTE 3D radiative transfer modelling, ALMA observations of the disc studied by I2011 have been simulated and the best tracers of the physical structure of a self-gravitating disc identified. The physical, chemical and radiative transfer models are described in section 3.2. Radiative transfer results are presented in section 3.3, while ALMA simulated observations are treated in section 3.4. Discussions and conclusions can be found in section 3.5.

3.2 Description of the Model

3.2.1 Physical structure

To appropriately describe the environment within which a young protoplanetary disc is embedded, the disc model from I2011 was combined with a model of a dense core with characteristics similar to the well-studied pre-stellar core L1544 (Keto & Caselli 2010, hereafter KC2010). Although L1544 does not appear to contain a central protostar and disc, it is very similar in structure to L1521F, another dense core in Taurus which hosts a low mass protostar and possibly a

disc (Bourke *et al.* 2006). The KC2010 model follows the dynamical, chemical and thermal evolution of a contracting Bonnor-Ebert sphere (Bonnor 1956; Ebert 1957) with a total mass of $10 M_{\odot}$, until it reaches the density, temperature and velocity profiles that best match observations. The pre-stellar core model adopted here contains slight modifications compared to KC2010 due to the inclusion of oxygen cooling in the outer regions of the cloud (Keto *et al.* 2014), where CO is mostly photodissociated (Caselli *et al.* 2012). Figure 3.1 shows the physical parameters of the core model adopted here.

The pre-stellar core structure is maintained down to a radius of 80 au, within which the model of the young protoplanetary disc is used. The disc structure is taken from the same hydrodynamical simulation of a $1 M_{\odot}$ protostar surrounded by a $0.39 M_{\odot}$ disc described in I2011. Figure 3.2 shows the azimuthally averaged rotational velocity in the disc plane, together with the best fit curve, which is used in section 3.4 to compare with position velocity diagrams. The system is envisaged to be at a very early stage of evolution and embedded in an envelope. The still growing protostar will eventually become an F type star through accretion of most of the disc's mass. The hydrodynamic simulation is run with a proper equation of state for molecular hydrogen (Boley *et al.* 2007b). The protostar is allowed to move freely in response to disc torques, and radiative cooling is included (Boley 2009). The self-gravitating disc exhibits prominent spiral structure, with H_2 number densities in the disc ranging from 10^4 - 10^{13} cm^{-3} and temperatures from 30-400 K (fig. 3.3). The disc model does not include magnetic fields, which may suppress gravitational instability and spiral wave formation by retarding or even preventing early disc growth in the case of sufficient magnetisation and alignment between the parent cores rotation axis and magnetic field direction (Joos *et al.*

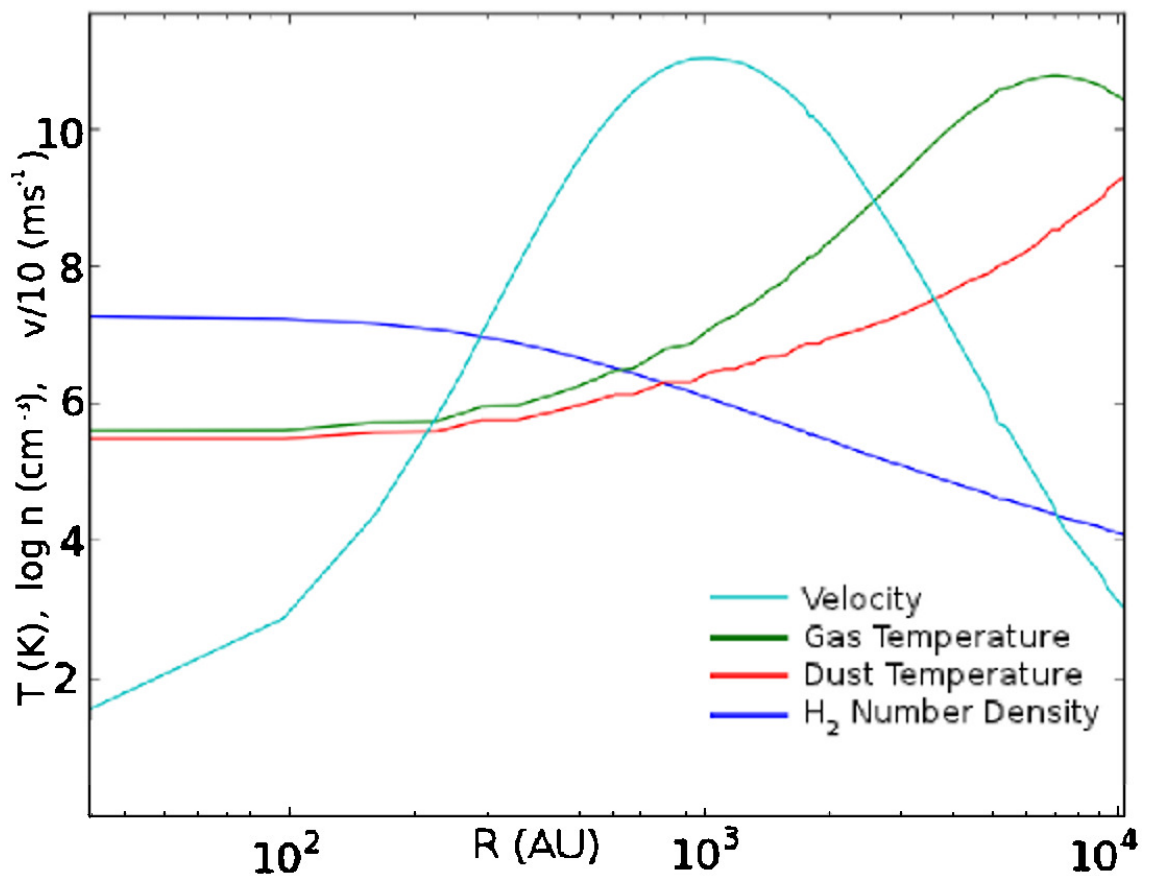


Figure 3.1: The spherically symmetric model of the pre-stellar core L1544 used as the envelope of the young protoplanetary disc in the hybrid model. Gas (green) and dust (red) temperature in Kelvin, log number density (blue) in cm^{-3} and inward velocity / 10 (cyan) in ms^{-1} are shown. Adapted from KC2010 and Keto *et al.* (2014).

2012; Li *et al.* 2013). Thus, the observation of spiral structure would provide strong constraints on the dynamical state of discs.

For the non-LTE 3D radiative transfer modelling presented here, the I2011 simulation output was interpolated on to a $256 \times 256 \times 64$ Cartesian grid with spatial resolution of 0.5 au in x , y and z and sample from this to create the unstructured radiative transfer grid (see section 2.1.3). As in the hydrodynamical simulation, the dust and gas temperatures are assumed to be in equilibrium within

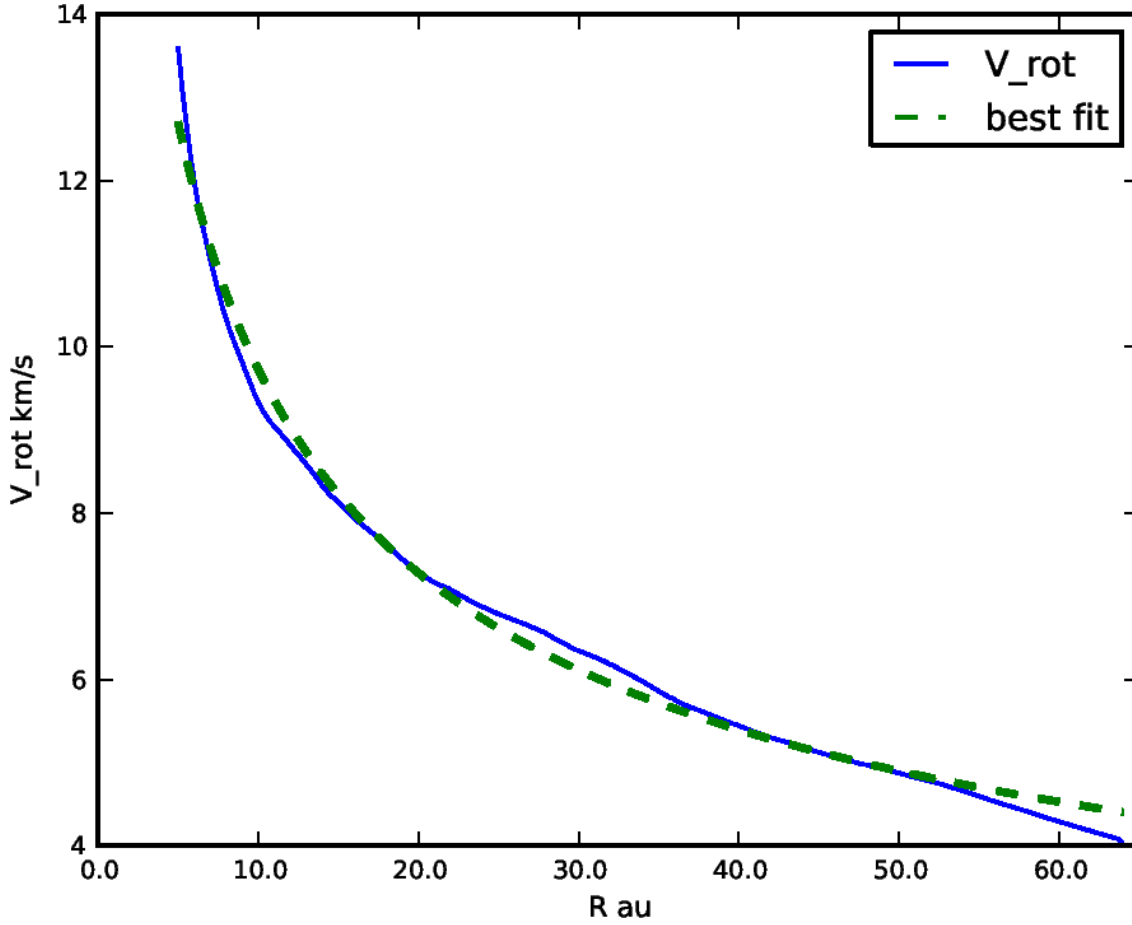


Figure 3.2: Azimuthally averaged rotational velocity in the disc mid-plane. The best fit curve follows the equation $V_{\text{rot}} = \frac{31.5}{\sqrt{R+1.68}} + 0.518$.

the disc and a gas to dust mass ratio of 100 is used. The dust opacities were adopted from Ossenkopf & Henning (1994) and are appropriate for dust grains with thick icy mantles and a 10^6 yr coagulation history. Although dust grains within the protoplanetary disc are expected to coagulate further, significantly affecting the opacity, grain growth was not taken into account in the model. The dust opacities used in the radiative transfer are not the same as the ones used in the hydrodynamical model (which used the dust opacities of D'Alessio *et al.* 2001). However, the results described here do not depend on the details of the

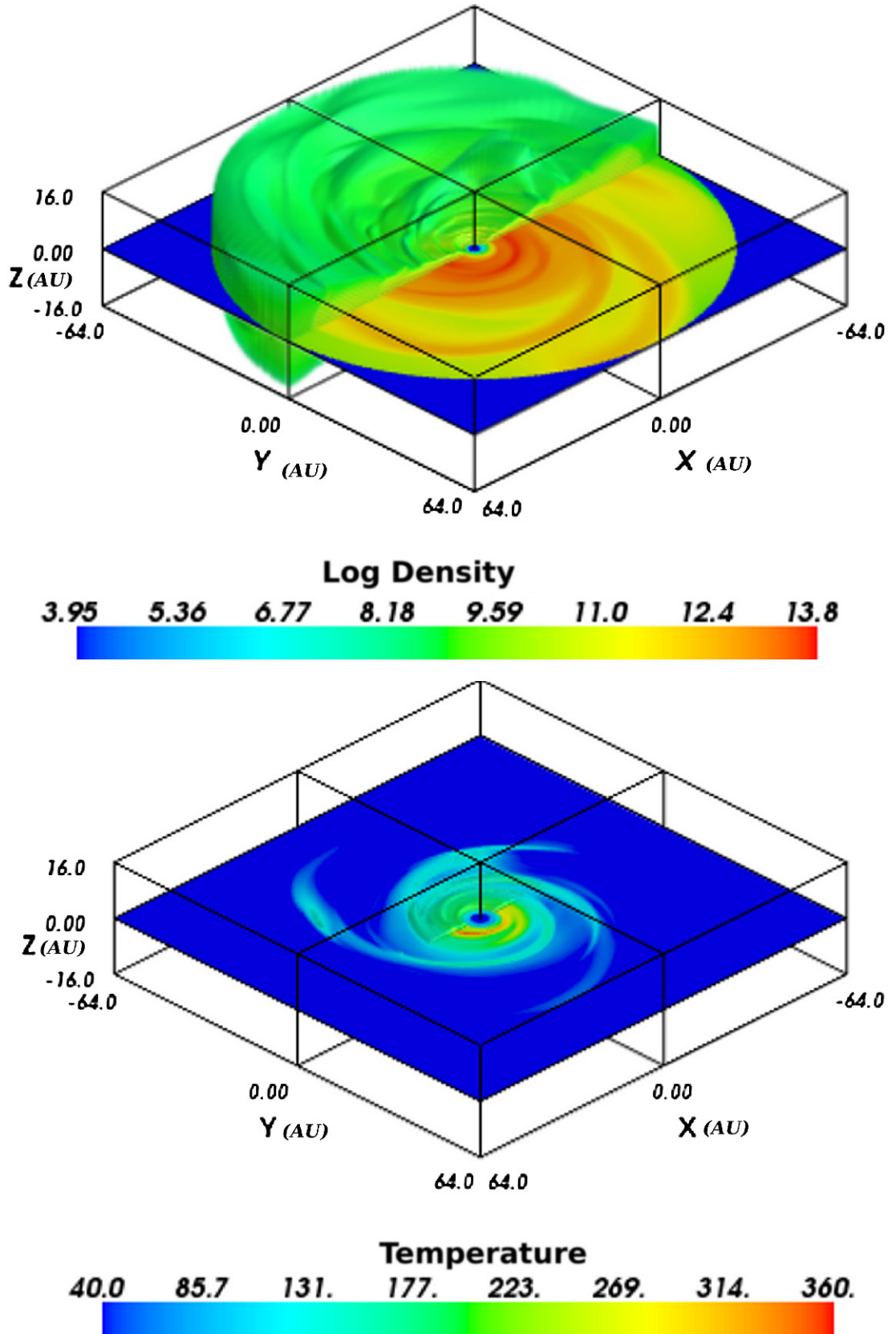


Figure 3.3: **Top:** A 3D plot of log number density (cm^{-3}) showing the spiral structure in the xy plane and scale height of the disc. **Bottom:** The 3D temperature (K) structure of the disc; regions cooler than 40 K are not shown in 3D, in order to highlight the narrow central region containing hot material.

dust opacity used during the hydrodynamic evolution.

3.2.2 Chemical structure

Chemical abundances in the disc were taken from I2011, who followed gas-grain chemical processes during the dynamical evolution of the disc. Photochemistry (other than cosmic ray induced photo-emission) is not taken into account, which is consistent with the assumption that in the early (Class 0, early Class I) stages of protostellar accretion and evolution considered here, the protostar/disc system is heavily embedded in a thick envelope of gas and dust. The combination of envelope infall onto the disc and powerful outflows (see e.g. Machida & Hosokawa 2013) may drastically limit the illumination of the upper layers of young discs by the central protostar and interstellar UV field. Observations are needed to establish the importance of photochemistry at these early stages.

As described in I2011, the hydrodynamical simulation included Lagrangian tracer fluid elements in addition to the solution of the equations of hydrodynamics on an Eulerian grid. These fluid elements were used to record the thermal and density histories of the gas as material passed through and between the spiral structure. I2011 used this time evolution information from the fluid elements to calculate the abundances of 125 species, related by 1334 reactions. These abundances were then interpolated by I2011 on to a Cartesian grid with cell sizes $2.2 \times 2.2 \times 0.22 \text{ au}^3$ in x , y and z . From these the four species which appear to trace different regions of the disc were selected: OCS (the inner 30 au), H_2CO (the inner 40 au), HCO^+ (the region between $\simeq 40$ and 60 au) and C^{17}O (the entirety of the disc) (see figure 3.4). As the I2011 chemical model did

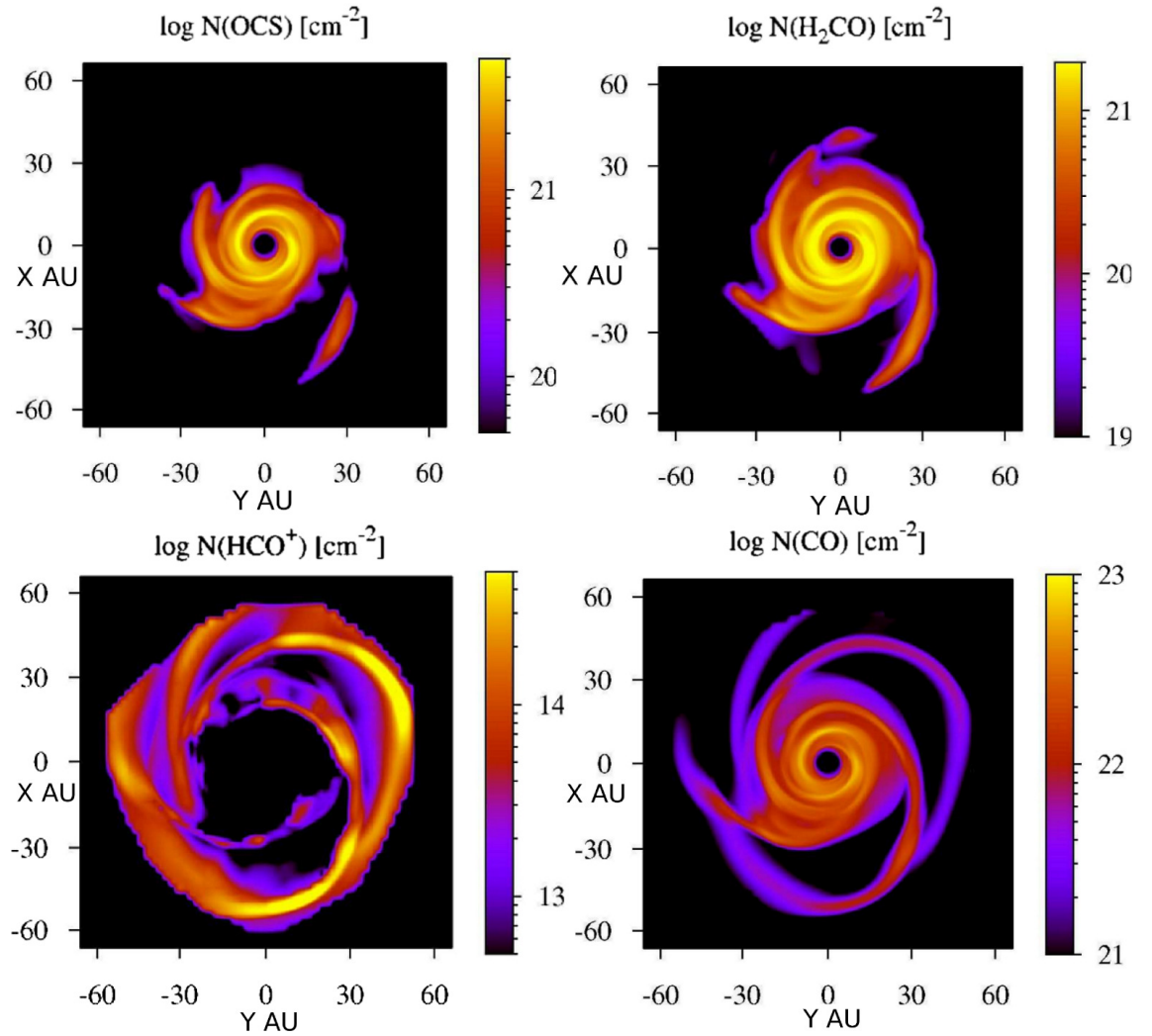


Figure 3.4: Column density distributions of OCS, H_2CO , HCO^+ and CO across the disc, as calculated by I2011. Note the different zones traced by the various species, with OCS mostly tracing the inner regions and HCO^+ probing the gas at larger radii.

not explicitly include reactions of CO isotopologues, the abundance model used for C¹⁷O was the ¹²C¹⁶O abundance reduced by a factor of 1792, the ratio of ¹⁶O to ¹⁷O in the local ISM (Wilson & Rood 1994). As explained by I2011, H₂CO and OCS mostly probe the central warm regions, where icy mantles evaporate, whereas HCO⁺ preferentially traces the outer spiral pattern as in the central region it is destroyed by water molecules and transformed into H₃O⁺ and CO. The simple chemistry in the KC2010 model, adopted here for the envelope of the protoplanetary disc, does not provide detailed abundances of molecular species (besides CO and H₂O, see also Caselli *et al.* 2012). As discussed in section 3.3, the envelope abundances are based on values measured toward similar objects. The molecular data used here for the radiative transfer are taken from the Leiden Atomic and Molecular DAtabase (LAMDA) (Schöier *et al.* 2005 <http://home.strw.leidenuniv.nl/~moldata/>, Botschwina *et al.* 1993, Flower 2001, Green & Chapman 1978, Troscompt *et al.* 2009 Wernli *et al.* 2006, Yang *et al.* 2010)

3.3 Model Results

Simulations are limited to molecules for which abundances in both the disc and envelope can be obtained, and also have reliable Einstein and collisional coefficients. In the envelope, the HCO⁺ abundance profile follows the H₂O profile of L1544 (Caselli *et al.* 2012), scaled so the maximum is 1×10^{-8} . For H₂CO, a step profile was considered, with a fractional abundance of 1.5×10^{-8} at radii greater than 0.04 pc and 1.5×10^{-9} at smaller radii (Young *et al.* 2004). For OCS a constant abundance of 1.9×10^{-9} (Ren *et al.* 2011) was adopted. The C¹⁷O

abundance profile in the envelope follows the CO profile calculated for L1544 by KC2010, scaled by the $^{17}\text{O}/^{16}\text{O}$ isotope abundance. These estimates for the abundances in the envelope are simplistic. However, as seen in section 3.4, the envelope contribution to the line is very limited in velocity and can be spectrally disentangled from the disc contribution.

The focus for simulated observations was on the frequency range available with ALMA, with particular attention to band 7, which offers the compromise between resolution and sensitivity. The results presented in this section are limited to those lines with detectable emission/absorption which can be used to trace either spiral structure or rotation, though other molecules, such as HCN, HNC, HNO, SO and SO₂ were simulated and lines in the ALMA bands were checked to see if they would be observable. Thus, C¹⁷O(3→2), HCO⁺(3→2), OCS (26→25) and H₂CO(4₀₄ →3₀₃) were chosen. The frequencies and upper level energies of these transitions are given in table 3.1. All the models used were simulated in LIME with 30,000 model points and 8,000 sink points on the outer edge of the simulated region.

To simulate observations, the model was placed at roughly the distance of nearby low-mass star forming regions (100 pc). The inclination angle was varied from 15° to 75° relative to the edge on case. From these simulated observations, integrated intensity maps, intensity weighted velocity maps and position velocity diagrams were created. The integrated intensity and intensity weighted velocity maps (figs. 3.5, and 3.10) are integrated from -12.5 to -0.5 km s⁻¹ and +0.5 to +12.5 km s⁻¹ to avoid domination by the contribution from the envelope, which can be seen in some PV diagrams as the strong absorption feature at all positions around zero velocity (see section 3.4). Intensity weighted velocity maps are shown

with a cut-off of 3σ as described in section 3.4.

OCS $26\rightarrow 25$ traces only the innermost 20 au of the disc and can be used to examine the central regions (fig. 3.5). As OCS is not usually seen in outflows (e.g. Stanke & Williams 2007, van der Tak *et al.* 2003), it can be used to measure the rotation of the central part of the disc without contamination from shocked material along the outflow. The OCS lines are unique amongst the lines simulated in that they trace only radii < 16 au, even smaller than the extent of the OCS column density distribution shown in fig. 3.4. This is because the OCS line, which has the highest upper energy level among the selected transitions, traces only the hottest and densest regions of the disc, where the high energy states are populated. As a result, the innermost spiral structure is best seen in OCS ($26\rightarrow 25$), as shown in fig. 3.5. The OCS line is mostly seen in absorption against the bright continuum emission from the disc mid-plane. The exception to this is towards the centre of the disc, where the hole in the hot, dense mid-plane produces little continuum to be absorbed. However, this may be an artefact of our treatment of the inner hole, given that the presence of the protostar and other hot material within the central 2 au is neglected. Therefore, absorption is expected to also be observed toward the central region of the disc.

The abundance of the H_2CO molecule traces the spiral structure of the inner ~ 40 au of the disc, which can be seen in the integrated intensity map, and its rotation is detected out to larger radii compared to the OCS line (fig. 3.5). As with the OCS line, the H_2CO $4_{04}\rightarrow 3_{03}$ line is mostly seen in absorption against the disc mid-plane continuum, with the central region seen in emission. However, unlike the OCS, the H_2CO extends out to large enough radii to trace the voids between the outer spiral arms. In these regions, H_2CO line emission can be seen.

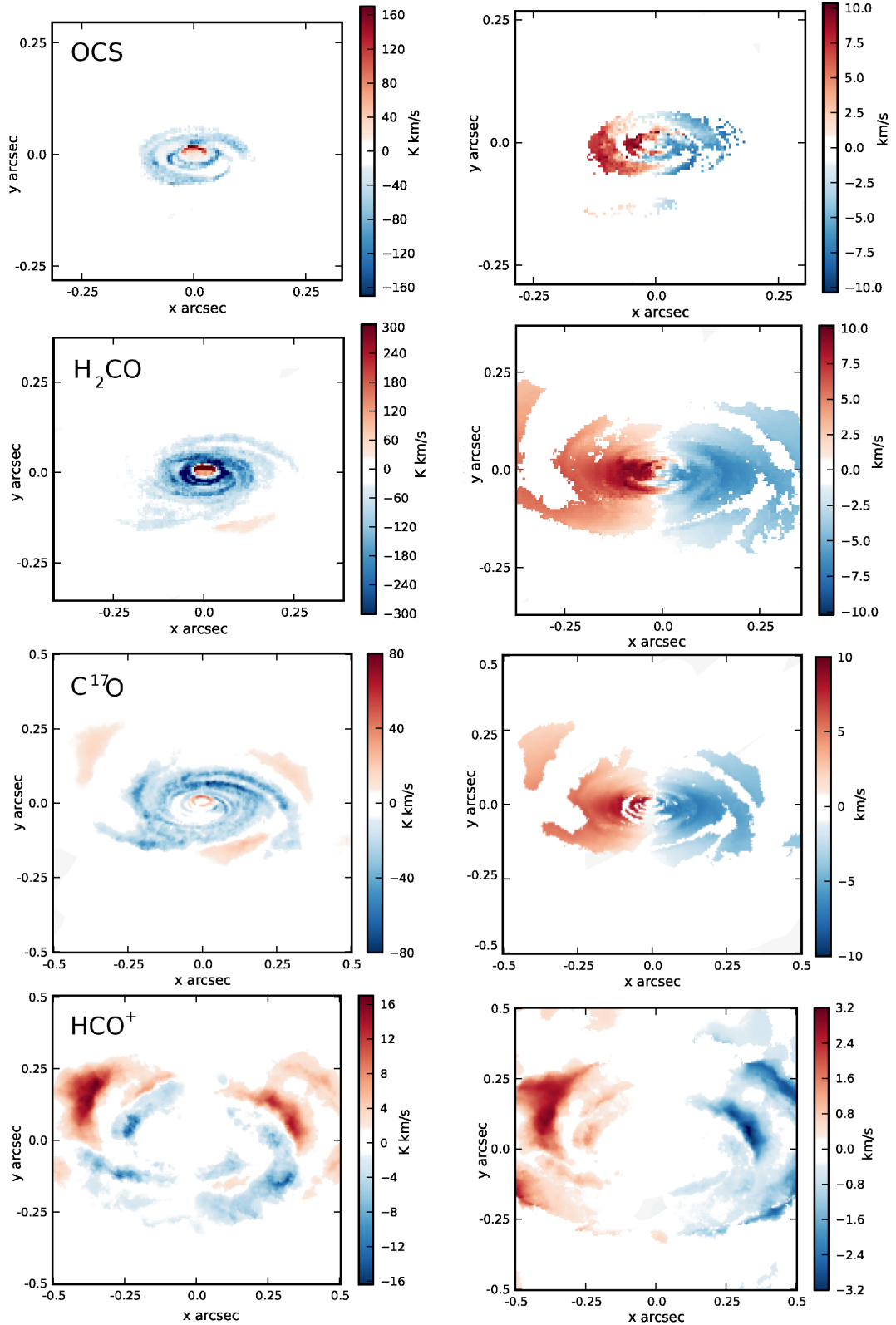


Figure 3.5: **Left:** Continuum subtracted integrated intensity maps. **Right:** Intensity weighted velocity maps. The spiral structures in different regions of the disc are highlighted by different molecular lines. From top to bottom the lines displayed are: OCS ($26 \rightarrow 25$), H₂CO ($4_{04} \rightarrow 3_{03}$), C¹⁷O ($3 \rightarrow 2$) and HCO⁺ ($3 \rightarrow 2$). All maps are obtained from integration over -12.5 to -0.5 and 0.5 to 12.5 km s⁻¹ in order to avoid the envelope contribution.

The fractional abundance of C^{17}O is constant at 2×10^{-8} across the disc, so that the selected C^{17}O line is the most accurate in reproducing the physical structure of the disc. Like H_2CO , C^{17}O shows emission in voids between spiral arms. The C^{17}O line is visible from the inner edge of the disc to its outer edge. Like OCS, C^{17}O is not seen in outflows (Yıldız *et al.* 2012), so contamination is not expected.

The HCO^+ line only traces the outer regions of the disc. In fig. 3.5 it can be seen that the HCO^+ line shows the outer edges of the spiral arms in absorption, but it also shows emission from the diffuse gas further out in the disc. This allows the velocity structure of the disc to be measured out to larger radii, allowing constraints to be placed on the rotation of the disc out to larger radii than with other molecules.

Simulations at inclinations other than 30° were also performed with C^{17}O . Figure 3.6 shows the C^{17}O 3 \rightarrow 2 line in the same physical model but at 15° , 30° , 45° and 75° to edge on. At 15° to edge on, some structure in the integrated intensity map is still observable and the spiral pattern is clearly seen in the position velocity diagram. At larger inclinations it gets more difficult to obtain any kinematic information but the physical structure of the disc becomes clearer.

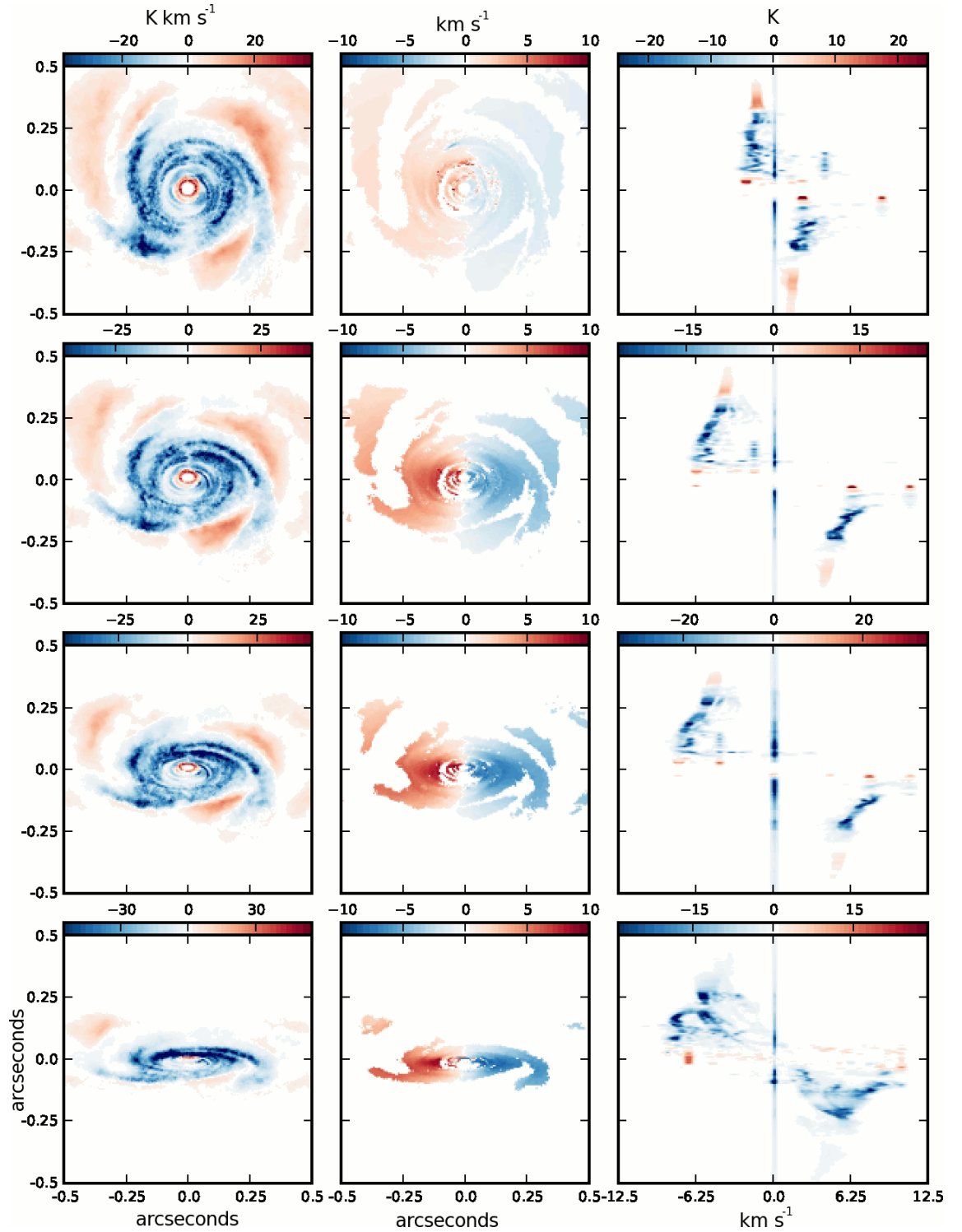


Figure 3.6: $C^{17}O$ 3 \rightarrow 2 **left:** Continuum subtracted integrated intensity map (in $K \text{ km s}^{-1}$). **Centre:** Intensity weighted velocity map (in km s^{-1}). **Right:** Position-velocity diagram along the $y=0$ line, with intensities in K . The inclinations for which results are shown from top to bottom are: 75° , 45° , 30° and 15° to edge on.

3.4 Predictions for ALMA

In order to make predictions of the observability of the features for which synthetic brightness maps were constructed, the Common Astronomy Software Applications package (CASA) was used to simulate observations with the completed ALMA in the 26th most extended configuration (out of a total of 28). The longest baseline of this configuration is 14.4 km and the beam sizes range between 0.02 and 0.03 arcseconds at the selected frequencies. This angular resolution is close to the size of the spiral structure in the disc. As the weakest lines studied in the model are of the order of $0.1\text{--}0.2\text{ mJy beam}^{-1}$ at this resolution, Band 7 sensitivities of the order of $0.02\text{ mJy beam}^{-1}$ are required. This implies around 6 hours of integration time. The exact sensitivities are given in Table 3.1. In order to clean the images which featured mainly absorption, the sky model used was the output of the LIME simulations with the continuum subtracted and then the spectrum inverted. The simulated images were “CLEANed” down to a 3σ level with σ (the sensitivity) given in Table 3.1.

Figure 3.7 shows the 1 mm continuum emission as observed with the chosen

Table 3.1: Line sensitivities obtained with ALMA after 6 hours integration time with velocity resolution of 400 m s^{-1} , obtained with the ALMA on-line sensitivity calculator.

Species	Transition	Frequency (GHz)	Upper energy level (K)	Sensitivity (mJy beam ⁻¹)
C ¹⁷ O	3→2	337.06	32.3	0.0270
OCS	26→25	316.15	205	0.0275
H ₂ CO	4 ₀₄ → 3 ₀₃	290.62	34.9	0.0228
HCO ⁺	3→2	267.56	25.7	0.0176

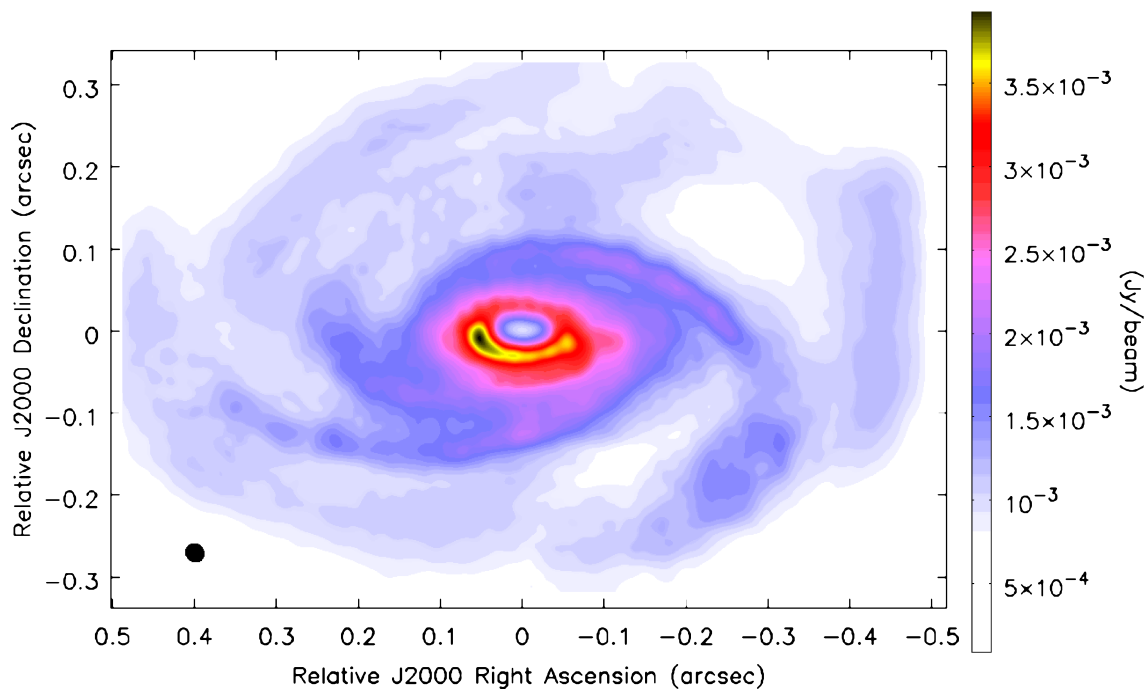


Figure 3.7: CASA simulation of the continuum emission of the model at 300GHz, using the same ALMA configuration as used for the molecular lines. The size of the beam at 300GHz is shown in the lower left corner.

ALMA configuration. The spiral structure of the disc is clearly visible at this inclination and it becomes clearer at angles closer to face-on. A mass estimate for the disc was calculated using the equation $M = gS_\nu d^2 / \kappa_\nu B_\nu(T_d)$ where g is the gas/dust mass ratio, S_ν is the integrated flux, d is the distance to the source, κ_ν is the dust opacity and $B_\nu(T_d)$ is the black body function for a given dust temperature (Beltrán *et al.* 2006). Using the above equation and integrating the flux from $y=0.2$ to -0.2 and from $x=0.4$ to -0.4 , a disc mass of between 0.1 and $0.005 M_\odot$ was obtained, if the dust temperature is fixed at 40 and 400 K, respectively. This shows that the disc is optically thick at millimetre wavelengths and millimetre observations underestimate the disc mass significantly, by factors of 4 or more (see also Forgan & Rice 2013). For young, massive discs such as

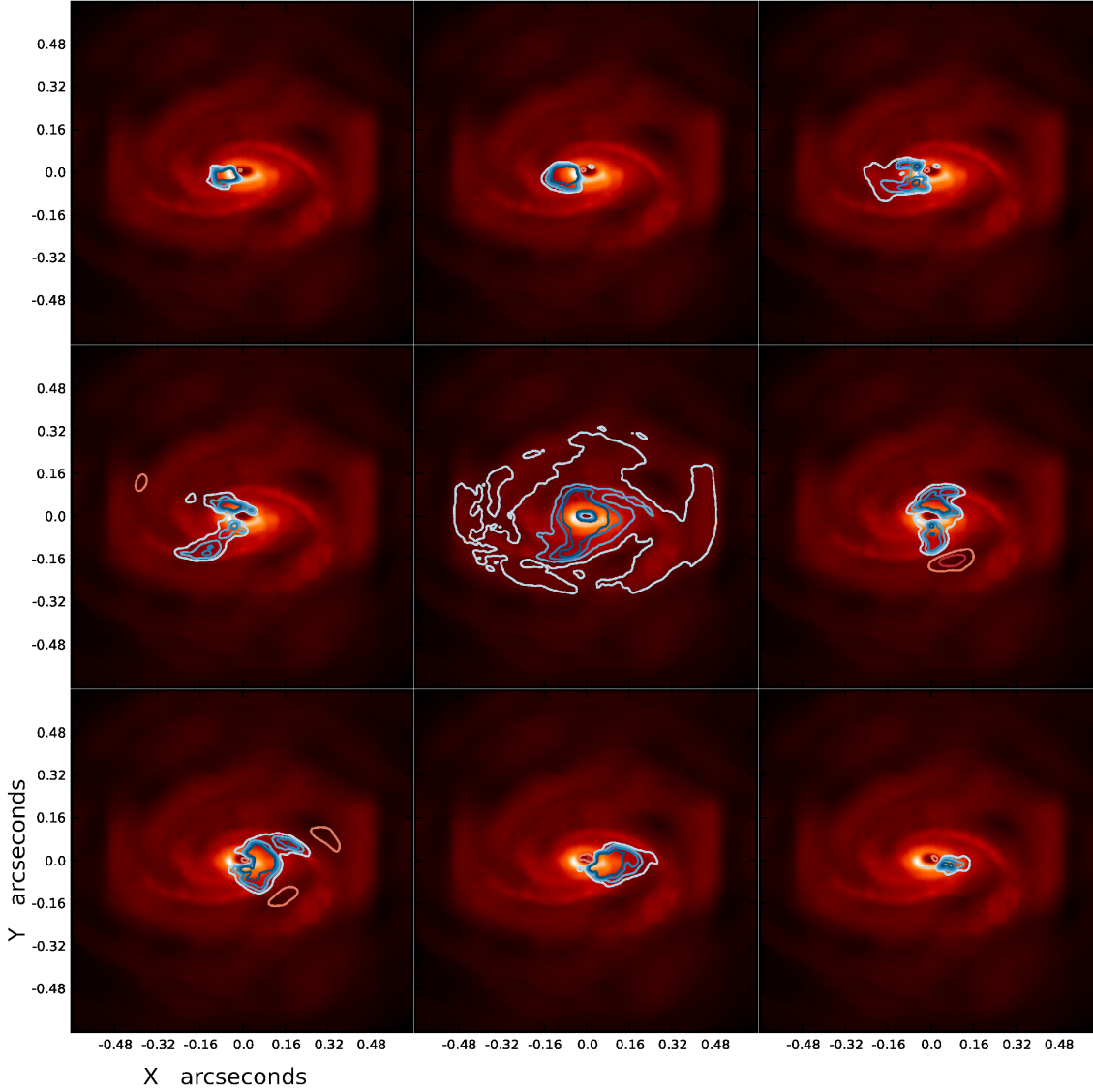


Figure 3.8: H₂CO 4₀₄ → 3₀₃ channel maps as simulated with CASA. The contours start at 0.35 mJy beam⁻¹ km s⁻¹ and are in steps of 0.35 mJy beam⁻¹ km s⁻¹ (absorption in blue, emission in red). Overlaid on the 1mm continuum emission. The integration range for each map is 2.4 km s⁻¹, for the top left the range is from -10.8 to -8.4 km s⁻¹ and for the bottom right the range is from 8.4 to 10.8 km s⁻¹.

those being investigated, longer wavelength continuum observations are necessary for determining the disc mass.

Figure 3.8 shows a channel map of the $\text{H}_2\text{CO } 4_{04} \rightarrow 3_{03}$ line overlaid on the 1 mm continuum emission. From this it can be seen that the absorption features trace the disc spiral structure whilst the line emission emanates from gaps in the outer disc, where there is less continuum to be absorbed. The central panel is dominated by the envelope contribution, causing strong absorption throughout the disc. The other panels show the line following a rotation pattern distorted by the presence of the spiral arms.

Figure 3.9 shows the CASA simulation of the $\text{C}^{17}\text{O } 3 \rightarrow 2$ integrated intensity and PV diagram for an inclination angle of 15° to edge on. Spiral structure can be clearly seen in the position velocity diagram even at low inclinations. The “finger-like” structures in the PV diagram are similar to those seen in observations of the Milky Way and in simulations of spirals in the Milky Way (e.g. Bissantz *et al.* 2003). Although the detail of the spiral structure (number of arms, pitch angle etc.) is difficult to gauge from such a PV diagram, high spectral and angular resolution observations can definitely unveil their presence and thus be used to find gravitationally unstable discs.

Figure 3.10 shows the simulated integrated intensity maps of the disc in the four selected molecular transitions. As expected from the radiative transfer results, observations of these transitions can probe different regions of the disc, from the OCS line tracing the innermost regions, to the HCO^+ line showing the outer regions. Thus, the high sensitivity and angular resolution of ALMA will allow detection of spiral structure both in the continuum emission as well as in

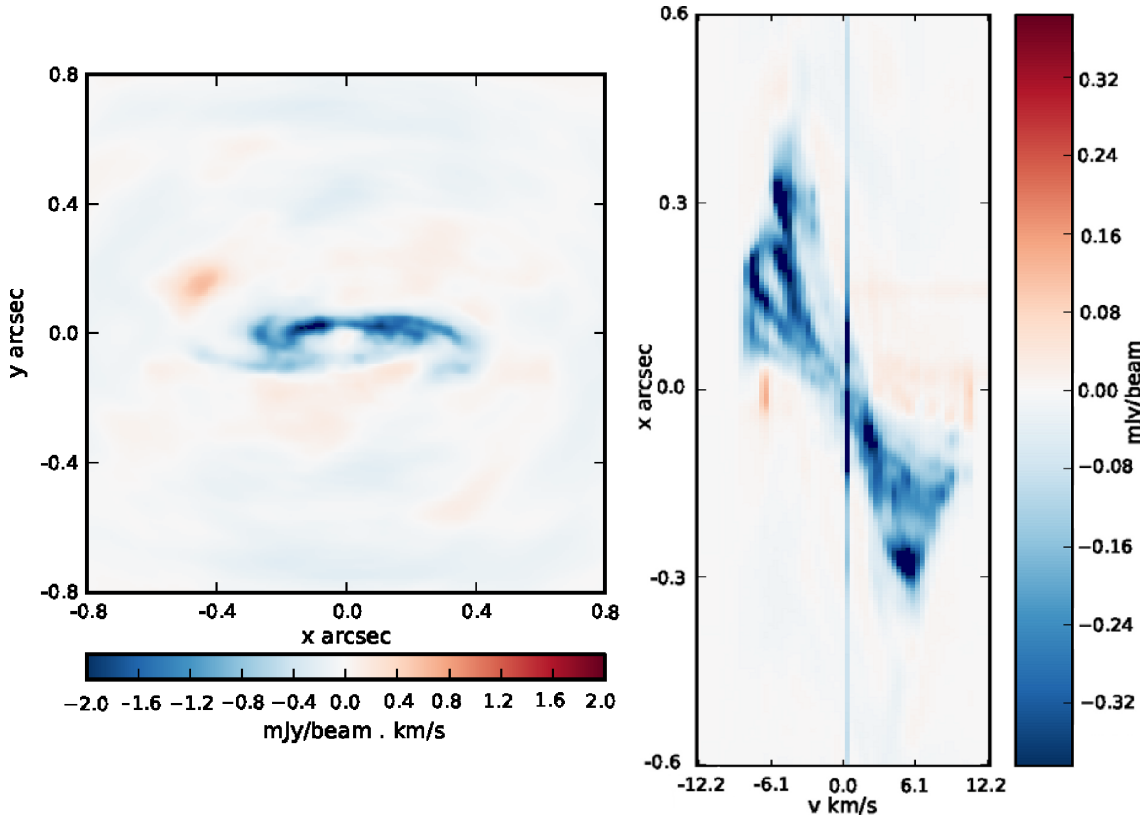


Figure 3.9: CASA simulation of the C^{17}O $3 \rightarrow 2$ line with the disc inclined at 15° to edge on. **Left:** Integrated intensity map. **Right:** Position velocity diagram across the $y=0$ line, where the spiral structures can be seen as narrow finger-like structures extending from the origin.

appropriately selected molecular transitions.

Position-velocity diagrams are shown in fig. 3.11. These diagrams can be used to reconstruct the rotation of the disc. The green curves in each panel of fig. 3.11 display the best fit rotation curve for the physical model (see fig. 3.2), showing that the rotation profile of the disc can be constrained by kinematic information gathered from species tracing different regions of the disc.

The spectra presented in figure 3.12 were extracted from the maps in fig. 3.10 for the positions indicated by the corresponding coloured dots along the $Y=0$

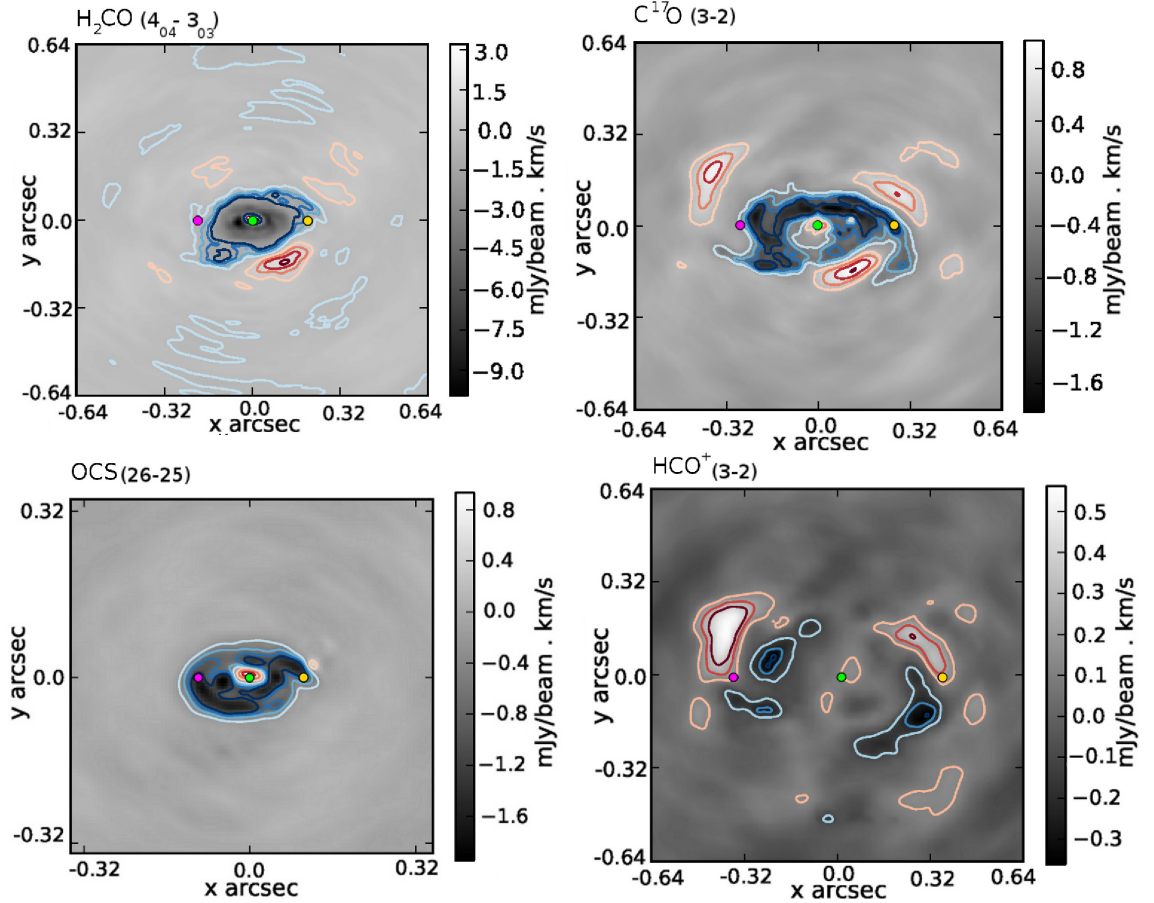


Figure 3.10: Integrated intensity maps for the simulated observations of: **Top Left:** $\text{H}_2\text{CO} 4_{04} \rightarrow 3_{03}$, **Top Right:** $\text{C}^{17}\text{O} 3 \rightarrow 2$, **Bottom Left:** $\text{OCS} 26 \rightarrow 25$ and **Bottom Right:** $\text{HCO}^+ 3 \rightarrow 2$. Contours start at 3σ and increase in intervals of 3σ for each of the maps except the H_2CO contours, which start at the 5σ level and increase in intervals of 5σ . Emission is in red contours, absorption in blue. The coloured dots refer to the positions from which the spectra shown in fig. 3.12 are taken.

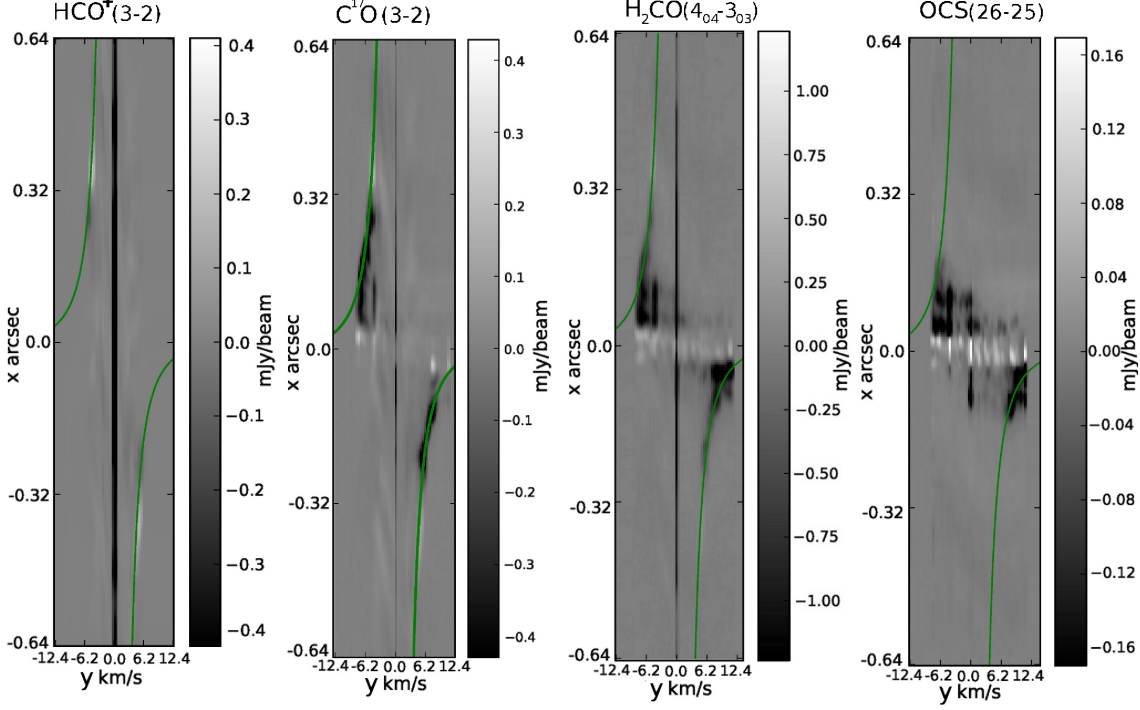


Figure 3.11: Position velocity diagrams for each of the lines simulated with CASA. The green curve on each diagram is the best fit curve to the azimuthally averaged rotation profile from fig. 4.

axis. As with all the CASA simulated images, these spectra were obtained with an ALMA window with total bandwidth 938 MHz, giving velocity resolutions between 418 and 527 ms^{-1} . Very notably, these spectral features are not symmetric about the disc centre. For example, C¹⁷O(3-2) has a significantly stronger blueshifted absorption, due to the presence of a spiral arm along the same line of sight. In the OCS lines, the two sides are not moving with equal velocities and the line widths and shapes are markedly different. These can be attributed to the non-axisymmetric nature of the model.

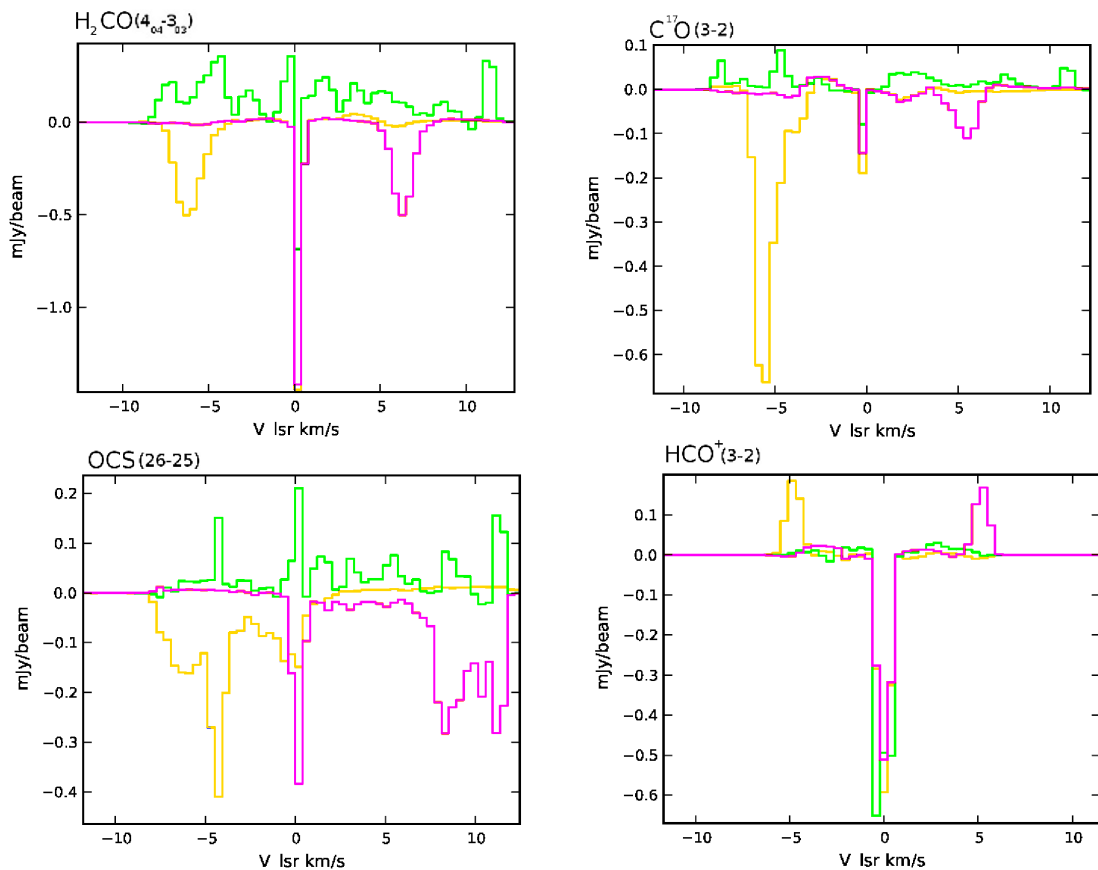


Figure 3.12: Simulated spectra for each of the selected transitions at the positions indicated by the coloured dots in figure 3.10 (the pink, green and yellow curves are taken from the locations marked by the dots of the same colour). In each diagram, the three spectra are taken from three positions on the $Y=0$ axis, one is at $X=0$ (green) and the other 2 are from $x=\pm N$ (plus yellow, minus pink) where N is the distance from the centre: 10 au for OCS, 20 au for H_2CO , 28 au for C^{17}O , 38 au for HCO^+ .

3.5 Conclusions and further work

In this chapter I have presented radiative transfer simulations of a hybrid model comprising a $0.39 M_{\odot}$ self gravitating disc with a radius of 64 au and spiral density waves, surrounded by an envelope that is a contracting $10 M_{\odot}$ BE-sphere. The main results of these simulations are as follows:

- CASA simulations of this model show that at a distance of 100 pc, extraction of kinematic and structural information from the continuum and molecular lines is possible with ALMA band 7.
- Our simulations show that molecular features are predominantly seen in absorption against the hot mid-plane of self-gravitating protoplanetary discs, with emission only being seen where voids in the structure of the disc do not provide a bright continuum source to be absorbed.
- The quiescent nature of the envelope around such discs only affects lines within $\pm 0.5 \text{ km s}^{-1}$ of the LSR velocity.
- The lines studied (OCS (26 \rightarrow 25), H₂CO (4₀₄ \rightarrow 3₀₃), C¹⁷O (3 \rightarrow 2) and HCO⁺ (3 \rightarrow 2)) taken together allow all regions of the disc to be sampled and the rotation of the disc to be constrained from the inner edge to the outer edge.
- Spiral structures in young embedded discs are detectable at a wide range of inclination angles. They can be resolved spatially at angles close to face on and can be inferred from position velocity diagrams at low inclination angles.
- The dust continuum emission at millimetre wavelengths is optically thick and millimetre observations lead to significant underestimates of the disc mass, by a factor of 4 or more.

One assumption underpinning this model is that the gas and dust are in thermal equilibrium in the disc. If they are not and the dust is significantly cooler than the gas then transitions may not show up in absorption. However, the large volume densities are expected to provide efficient dust-gas coupling. Outflows could contaminate line profiles of those species which commonly trace outflows, such as CO and HCO⁺. In these cases, a detailed study of their line profiles using high spectral resolution should help to disentangle the various kinematic

components.

These results demonstrate that ALMA will be able to probe the very earliest stages of circumstellar discs which feed the growing protostar, and which eventually will evolve in a planetary system. My results show that ALMA observations in band 7 will allow the assessment of whether or not these young discs are gravitationally unstable and test theories of pre-stellar to protostellar core evolution. If such gravitational instabilities exist, they will have significant implications for the evolution of the disc. For example, they will affect fragmentation, planetesimal formation (Boley 2009; Johnson & Li 2013; Gibbons *et al.* 2012) and the chemical evolution in the disc (I2011).

Chapter 4

Hydrodynamic simulations of line mediated radiatively driven disc winds

4.1 Introduction

The details of massive star formation are still unclear at this time. There are both issues with their observation (relative scarcity and embedded nature) and with the theoretical understanding of their formation (overcoming the radiative barrier, whether or not they form from a single collapsing massive core or not). There has however been recent work suggesting that discs around MYSOs may play a crucial role. Kraus *et al.* (2010) observed a ~ 15 au disc around a $20M_{\odot}$ MYSO perpendicular to a large scale outflow. Maud *et al.* (2013) detected a disc in millimetre continuum emission in the MYSO S140-IRS1. This disc is aligned with radio bremsstrahlung emission thought to be from an ionised disc wind and

is perpendicular to an outflow cavity. Also Ilee *et al.* (2013) inferred the presence of discs around 20 MYSOs via the detection and profile of the carbon monoxide ro-vibrational bandhead data. These observations corroborate recent theoretical work showing that disc accretion allows MYSOs to carry on accumulating mass even after they become luminous enough that the radiation pressure can overcome their gravity (Krumholz & Matzner 2009; Kuiper *et al.* 2010, 2011).

If massive stars do have accretion discs surrounding them, their combined stellar and accretion luminosity should drive outflows from these discs. Proga *et al.* (1998) showed that the CAK formulation of line driven winds could be applied to geometrically thin discs in the context of cataclysmic variable stars. They found that in the presence of significant luminosity from the central star ($\simeq 3$ times the disc accretion luminosity) a steady state, high density, low velocity wind could be driven from the disc. In models with less central luminosity than this, a wind could still be driven in most cases but these are complex time varying winds. These types of wind are unlikely to occur in the presence of a highly luminous MYSO.

This approach was adapted to model a $10M_{\odot}$ MYSO by Drew *et al.* (1998) showing that a radiatively driven disc wind could be driven from a disc around a MYSO. However, this work only modeled the inner 0.25au of a geometrically flat disc around a $5.5R_{\odot}$ star. In order to make observational predictions for these winds, models on the order of ~ 100 au are needed and on this scale the disc cannot be considered to be infinitely thin.

This chapter presents models of line driven disc-winds from a range of models simulating a $10M_{\odot}$ star, resolving the inner edge of the disc and extending out

to 300au. Section 4.2 describes the setup of the models and the parameter range explored, with section 4.2.2 describing the hydrodynamics used and section 4.2.3 detailing the method for calculating the radiation forces. Section 4.3 describes the methods used to analyse the models, section 4.4 describes the findings of these simulations and these are summarised in section 4.5.

4.2 Description of the Models

The method of modeling radiatively driven disc winds used here is as follows. Firstly a 2D axis-symmetric simulation of the inner 7.5 au of the star-disc system is set up with a stationary hydrostatic disc and a radial stellar wind above six disc scale heights. The time averaged results of this model are then used as an input to a second larger model extending out to ~ 300 au. For the outer model, regions in $r < 7.5$ au (i.e. the area simulated in the inner model) are fixed to the time average of the inner model.

The model is split into separate inner and outer models for two reasons. The first is computational: in order to have a single model extending out to 300 au and simultaneously resolving the inner edge of the disc would require spanning 6 orders of magnitude in cell length, requiring too many levels of AMR refinement. Secondly, the inner region of the disc can be assumed to be in thermal equilibrium with the protostar and so we use an isothermal equation of state (e.g. Drew *et al.* 1998). At greater distance away from the protostar, however, this assumption becomes less valid and an adiabatic equation of state is more appropriate. As *MG* hydrodynamics code does not support multiple equations of state within a single model, splitting the model into two allows this limitation to be overcome.

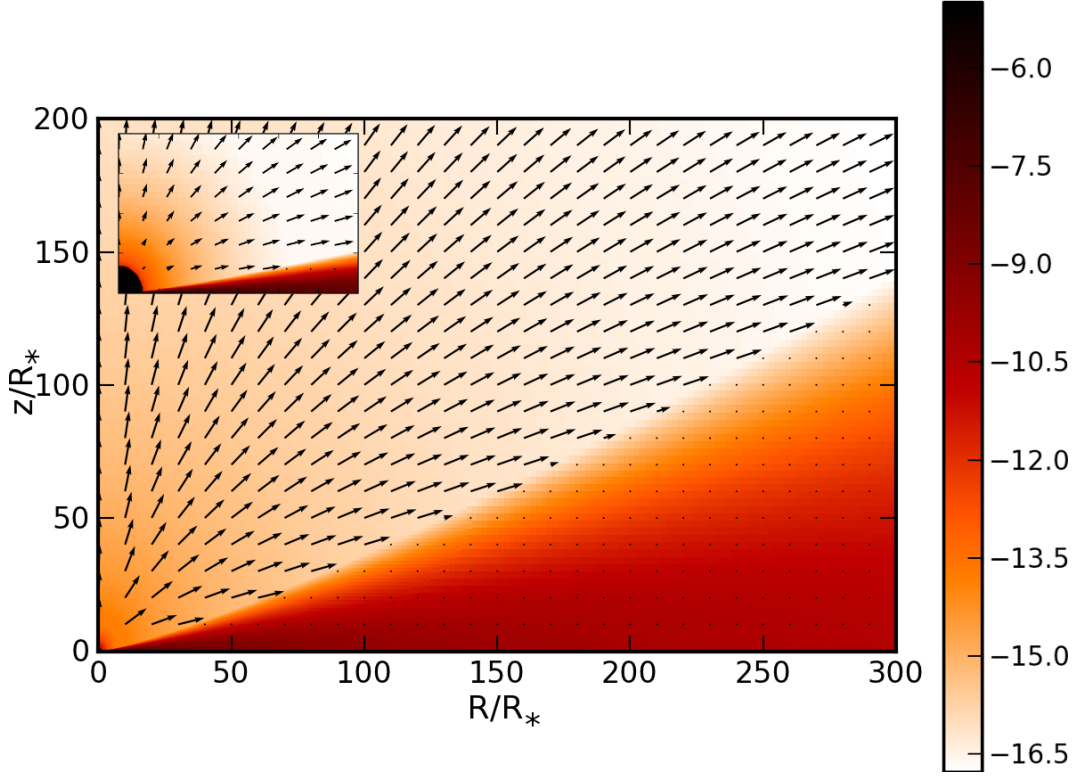


Figure 4.1: The initial density (in kg/m^{-3} and velocity (scaled so the largest arrow is $2000 km s^{-1}$) distribution for one of the models simulated. Inset: inner region ($R = 0 - 10 R_*$) of the model.

4.2.1 Model initial and boundary conditions

The initial setup for the inner model is a 2D axis-symmetric model 7.5au in radial extent by 5au in vertical. At the origin of the model, the protostar is modeled as a sphere of constant density (ρ_0) and temperature (T_*), which is not subject to time evolution. ρ_0 i.e. the disc midplane and photosphere density at $R=R_*$ is $10^{-5} kg/m^3$ for the model with a protostellar radius of $5.5 R_\odot$ and scales as $\left(\frac{r_*}{5.5 r_\odot}\right)^{-3}$. This scaling is based assumption the density of the inner edge of the disc matches that of the photosphere. With a $10 M_\odot$ of material in each protostar, we assume that the density of the photosphere is inversely proportional to the

stellar volume.

The disc is in hydrostatic equilibrium with an advected scalar representing angular momentum providing support against the gravity of the star. At heights above the disc greater than six scale heights the model is filled with the spherically symmetric line driven wind calculated in a 1D model using the same stellar parameters. Figure 4.1 shows the initial model setup for one of the models, and figure 4.2 shows the result of the 1 dimensional model for the same parameters whose results are used as the initial conditions above the disc and compares them to a semi-analytic spherically symmetric solution to the CAK equations. The numerical model shows good agreement with the semi-analytic models but with a slightly steeper density gradient, this is likely due to the finite resolution of the numerical model struggling to resolve the sharp transition at the stellar surface. The boundary conditions are symmetric at the inner edge of the R co-ordinate and fixed at the lower edge of the z coordinate. Both outer edges are outflowing boundaries.

The scale height of the hydrostatic disc is given by:

$$H = \frac{c_s}{\Omega}. \quad (4.1)$$

For a hydrostatic accretion disc with a radial temperature profile set by the balance of stellar irradiation to flux emitted the temperature is proportional to $R^{-1/2}$ (Chiang & Goldreich 1997). This gives a disc scale height of

$$H = \frac{c_s}{\Omega_K} = \frac{c_{s,0} (R/R_*)^{-1/4}}{\sqrt{M_* G/R^3}} = \frac{R_*^{1/4} c_{s,0}}{\sqrt{M_* G}} R^{5/4}, \quad (4.2)$$

where $c_{s,0}$ is the sound speed of gas in the disc at $R=R_*$ and is such that the tem-

perature of the gas at R_* is equal to the effective temperature of the protostellar surface and Ω_K is the angular velocity for a Keplerian orbit at a given radius.

If we assume that both the accretion rate and the Shakura & Sunyaev α are constant throughout the disc we can see from equation 1.9 that

$$\begin{aligned} T_{(R)}\Sigma_{(R)} &\propto \Omega_{(R)} \\ T &\propto R^p, \Sigma \propto R^q \\ &\rightarrow p + q = -3/2, \end{aligned} \tag{4.3}$$

and so Σ is set to be proportional to R^{-1} in each of the models, except one model which features an exponential cutoff in density after 75 au.

In order to balance the star's gravity, the specific angular momentum of the gas is tracked as an advected scalar. In tracking the angular momentum this way it is assumed that the angular momentum is both conserved and not transferred from one element of mass to another. The first of these assumptions is consistent with the use of axis-symmetry in the model and the neglecting of ϕ terms in the disc flux (see section 4.2.3), while the second is consistent with assuming that there are no global torques in the disc. The initial setup of the model has the specific angular momentum ($\frac{J}{\rho}$) of the material in the disc equal to that of a Keplerian orbit

$$\frac{J}{\rho} = \sqrt{RM_*G} \sin(\theta). \tag{4.4}$$

Material not in the disc is assumed to have angular momentum decreasing

rapidly with increasing height above the disc. This is modeled as a Gaussian decrease in the specific angular momentum with disc scale height above 4 disc scale heights so that

$$\frac{J}{\rho} = \sqrt{RM_*G} \sin(\theta) \exp \left[-\frac{(z - 4H)^2}{2H^2} \right]. \quad (4.5)$$

This was chosen so that that the material in the radial stellar wind far away from the disc contains practically no angular momentum, and that there are no discontinuities in the centrifugal force for the initial model setup. The density and velocity structure of the stellar wind were determined by performing 1D simulations using the same k and α parameters to be used in the 2D simulations.

The maximum resolution used in all the inner models is $R_*/64$. This is sufficient to resolve the innermost region of the disc to greater than 1 cell per scale height and convergence testing shows that global parameters are not affected by further increasing the resolution (figure 4.4). However, with this cell size the stellar surface is insufficiently resolved to launch a spherically symmetric wind. The effect of trying to resolve a circle of constant density which has large density and velocity gradients on its boundary is that the staircase shape of the edge of the star gets transmitted to the wind and amplified by the driving forces. In order to prevent this the region of the model that is time independent is extended out past the stellar surface to $1.1R_*$. In the region between 1 and $1.1R_*$ the density, pressure and velocity are set to the same 1D spherical wind solution that is used as the initial condition above the disc. This prevents the staircasing effect that is otherwise seen (figure 4.3). However this has the effect of fixing the structure

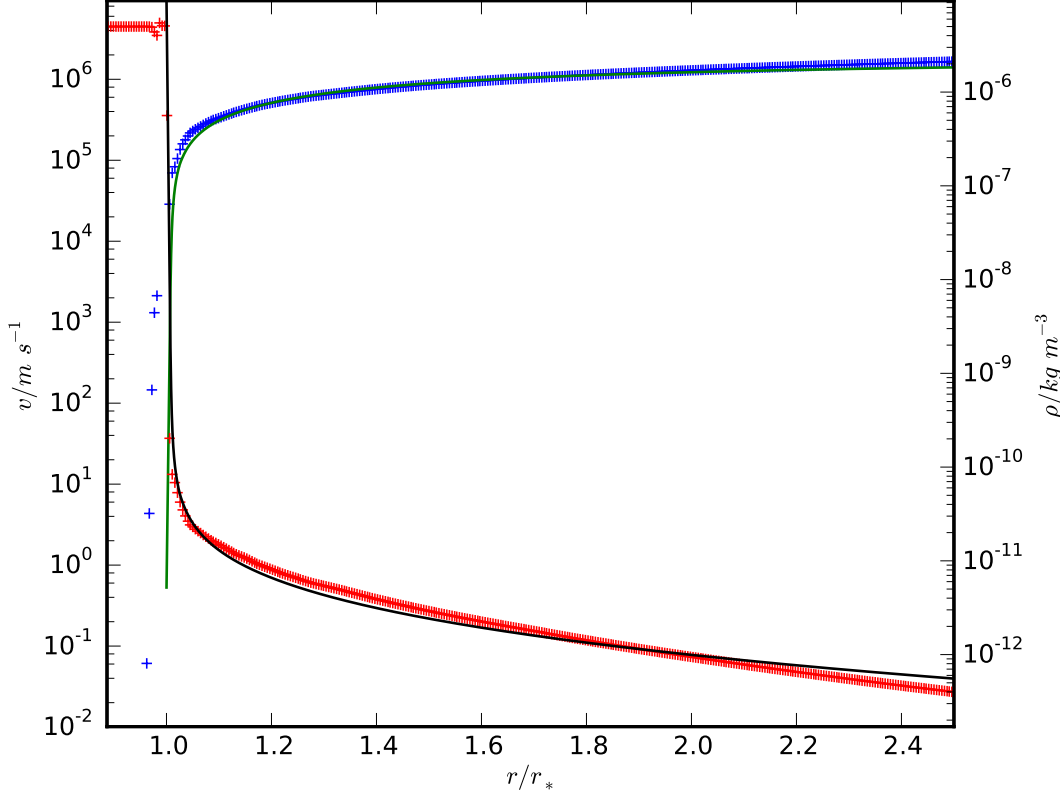


Figure 4.2: The density (black line red crosses, right axis) and velocity (blue crosses green line, left axis) of the 1D spherical model for a $10 M_{\odot}$, $8500 L_{\odot}$ $5.5 R_{\odot}$ star. The crosses show the values of the 1D hydrodynamic model and the lines show the results of a semi-analytic solution to the CAK model for the same stellar parameters.

of the polar wind as the sonic point of the wind and a significant portion of the region between the sonic and singular points are fixed to the predetermined values rather than being self-consistently calculated. In the outer model the temperature, density and angular momentum follow the same profiles, except for the region of $r < 1620 R_{\odot}$ where the model is initialised to the time average of the inner model.

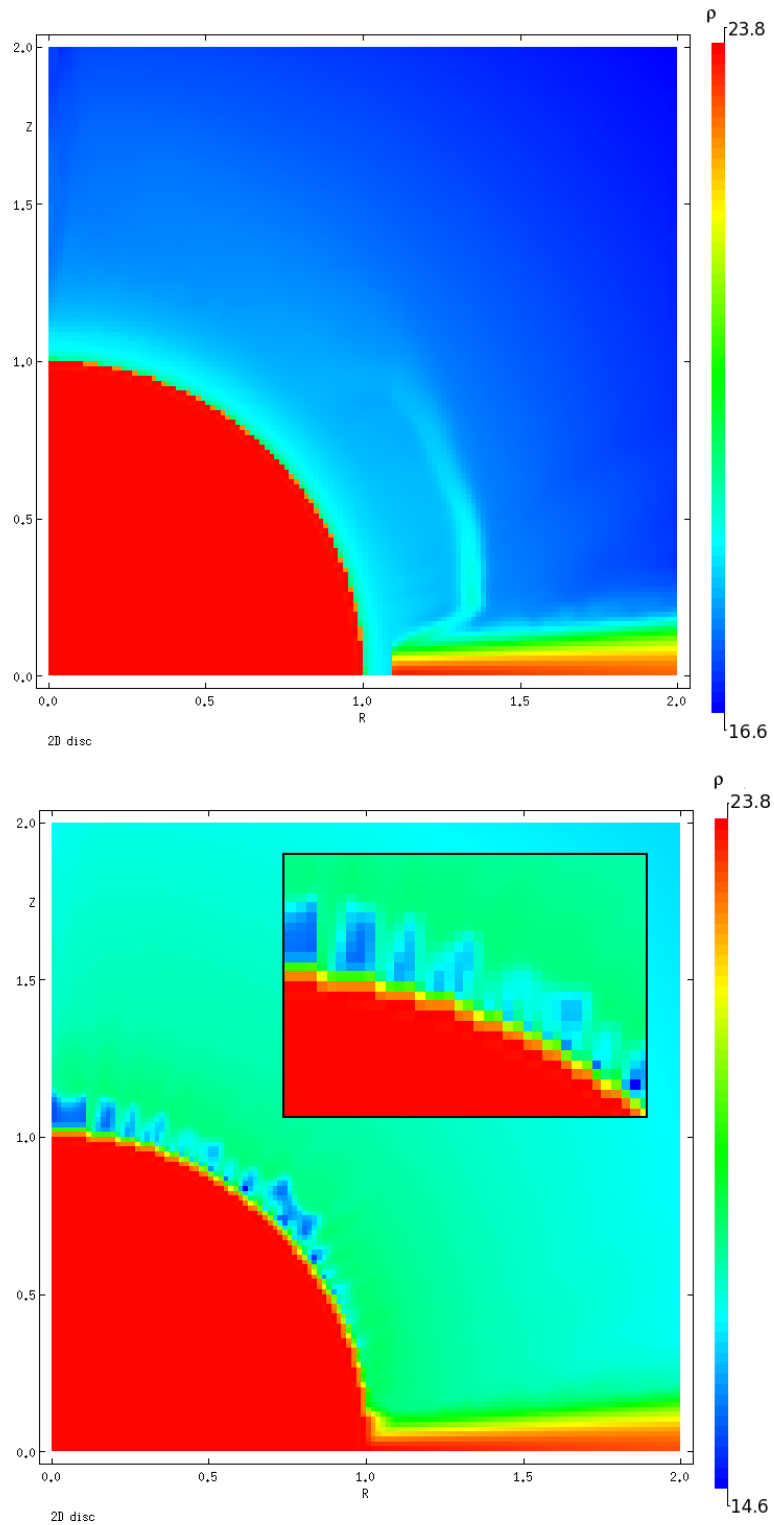


Figure 4.3: The log of the density (in code units) around the star’s surface for a model with a fixed region out to $1.1R_*$ (**top**) and without a fixed region outside of the star (**bottom**) a short time after the start of the model ($\sim 3000s$). Without a region where the transition from star to wind is fixed into the model the “staircase” shape of the star’s boundary is replicated in the wind.

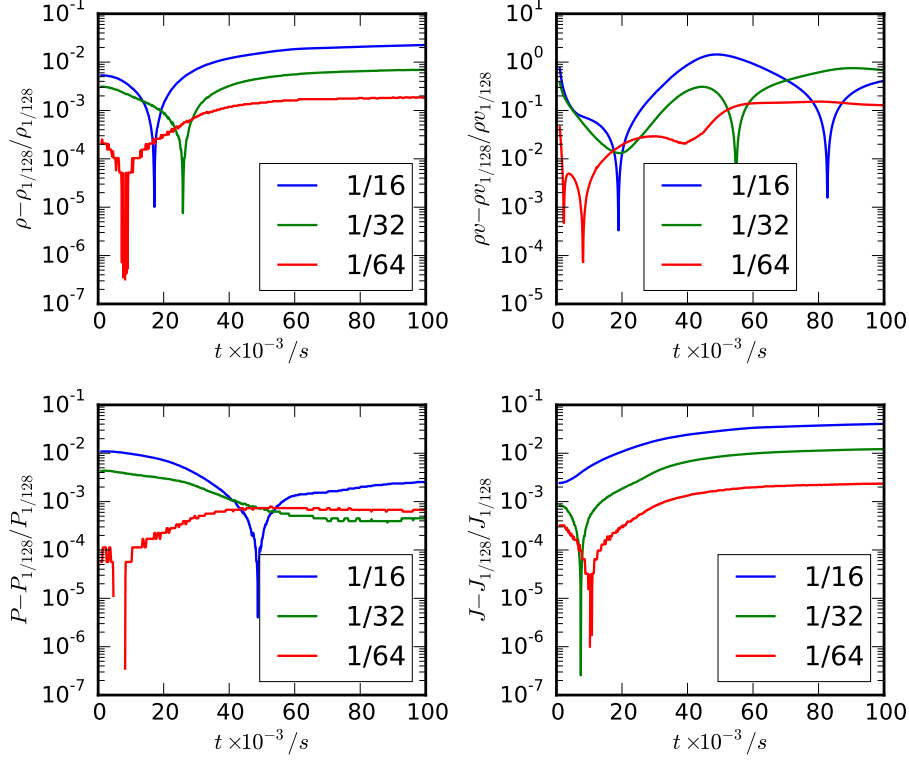


Figure 4.4: The fractional difference of the sum of the density, momentum, pressure and angular momentum for different maximum resolutions. Each resolution is compared against a run with a maximum resolution of $1/128R_*$ and the values are summed over a model extending out to $12 R_*$ in R and z.

The range of model parameters (shown in table 4.1) used are based on the protostellar tracks of Hosokawa & Omukai (2009). In these models a protostar accreting mass at $10^{-4} M_\odot \text{yr}^{-1}$ reaches $10 M_\odot$ with a photospheric radius of $16.2 R_\odot$ and a luminosity of $8200 L_\odot$. Models R11.7, R10.0, R7.7 and R5.5 represent this protostar isoluminantly contracting towards the main sequence (though to make comparisons between models clearer, the disc accretion luminosity has been kept as would be expected from an accretion rate of $10^{-4} M_\odot \text{yr}^{-1}$). For an accretion rate of $10^{-3} M_\odot \text{yr}^{-1}$ the protostar reaches the same mass with a radius of $145 R_\odot$. A luminosity of $8500 L_\odot$ rather than $8200 L_\odot$ has been used in all models to allow

Table 4.1: Model parameters

Model Name	M_* (M_\odot)	L_* (L_\odot)	R_* (R_\odot)	T_* (10^3K)	$T_{disc} \propto$	$\Sigma_{disc} \propto$	\dot{M}_* (M_\odot/yr)
R5.5	10	8500	5.5	23.7	$R^{-1/2}$	R^{-1}	10^{-4}
R7.7	10	8500	7.7	20.0	$R^{-1/2}$	R^{-1}	10^{-4}
R7.7_cut	10	8500	7.7	20.0	$R^{-1/2}$	$R^{-1} \exp[-R/75au]$	10^{-4}
R10.0	10	8500	10.0	17.5	$R^{-1/2}$	R^{-1}	10^{-4}
R11.7	10	8500	11.7	16.2	$R^{-1/2}$	R^{-1}	10^{-4}
R16.2	10	8500	16.2	13.8	$R^{-1/2}$	R^{-1}	10^{-4}
R145.0_1e-3	10	8500	145.0	4.6	$R^{-1/2}$	R^{-1}	10^{-3}

for comparisons with Drew *et al.* (1998) who modeled the wind up to a radius of $10 R_*$ of a $5.5R_\odot$, $8500L_\odot$, $10M_\odot$ protostar accreting at a rate of $10^{-6}M_\odot\text{yr}^{-1}$.

4.2.2 Hydrodynamic equations & source terms

As described in chapter 2, the hydrodynamic equations being solved in this model are:

$$\frac{\partial \rho}{\partial t} + \nabla \cdot (\rho \mathbf{u}) = 0 \quad (4.6a)$$

$$\frac{\partial \rho \mathbf{u}}{\partial t} + \nabla \cdot (\rho \mathbf{u} \mathbf{u}) + \nabla P = \rho \mathbf{a}, \quad (4.6b)$$

$$\frac{\partial e}{\partial t} + \nabla \cdot ((e + P) \mathbf{u}) = \rho (\mathbf{a} \cdot \mathbf{u}). \quad (4.6c)$$

where ρ is the mass density, \mathbf{v} is the velocity, e is the total energy per unit volume and \mathbf{a} is the vector sum of the acceleration due to the gravity, centrifugal force and the individual radiative forces from each disc point and the star (see section 4.2.3).

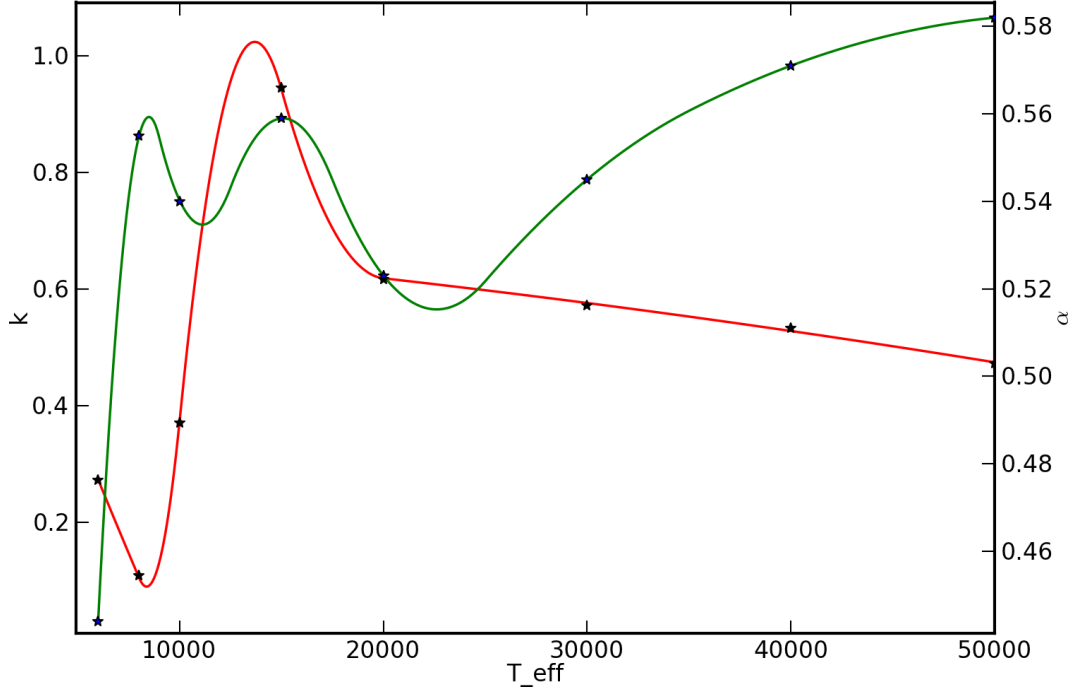


Figure 4.5: The values of the k (red line, black points) and α (green line, blue points) parameters used in this model as functions of effective stellar temperature (in Kelvin). The points correspond to the literature values of Abbott (1982) and the lines are the second order splines used to interpolate between the values.

The hydrodynamics code *MG* has been used in order to solve the mass, momentum and energy conservation equations with momentum source terms $p_{\text{source}} \propto kt^{-\alpha}$ where k and α are constants dependent upon the surface temperature of the star (interpolated from Abbott (1982), see figure 4.5) and t is an optical depth parameter assuming large velocity gradients $t = \sigma_e n v_{th} \left(\frac{d(\mathbf{v} \cdot \mathbf{l})}{dl} \right)^{-1}$, where σ_e is the Thompson scattering cross section for an electron, v_{th} is the thermal velocity of the gas and l is a line from the photon source to the fluid element (see section 4.2.3 for a detailed description of the geometry and method of calculation of the line forces).

The radiation forces are calculated along lines from 225 point sources in the

disc (distributed logarithmically in R from 1 to $10 R_*$ and linearly in ϕ from 0 to π) with intensities equivalent to a flat, optically thick disc accreting at $10^{-4} M_\odot \text{yr}^{-1}$, and one line from the origin for the stellar flux, taking into account the correction for the flux coming from a finite stellar disc rather than a point source.

4.2.3 Calculation of the line driving force

The acceleration due to the scattering of lines in the wind (mainly C, N and O atomic and ionic forbidden lines Puls *et al.* 2000) can be estimated by multiplying the acceleration due to Thomson scattering by a multiplier dependent upon the line optical depth:

$$\mathbf{a} = \frac{1}{\rho} \sum_i \left(\mathbf{F}_i \frac{\sigma_e}{c} M(t) \right) - \nabla \phi + \frac{J^2}{\rho^2 R^3} \hat{R}, \quad (4.7)$$

where σ_e is the Thomson scattering cross-section of an electron, \mathbf{F}_i is the vector flux given by

$$\mathbf{F}_i = \mathbf{r}_i \frac{a}{4\pi |\mathbf{r}_i|^3} \int I_\nu d\nu, \quad (4.8)$$

a is the radiating area of the luminosity source, \mathbf{r} is the displacement from the luminosity source to the cell under consideration, $\nabla \phi$ is the gradient of the protostar's gravitational potential, J/ρ is the specific angular momentum and $M(t)$ is the line force multiplier:

$$M(t) = \max(1000, k t^{-\alpha}) = \max \left(1000, k \left| \frac{\sigma_e v_{th} \rho}{\mu^{dv/dl}} \right|^{-\alpha} \right), \quad (4.9)$$

where v_{th} is the thermal velocity and μ is the mean atomic mass (the gas is assumed to be all atomic and 0.908 hydrogen, 0.091 helium by number with the remainder carbon Wilson & Rood 1994). t is calculated individually for each disc component and the star. The resultant momentum source terms are added into the solver along with a corresponding $\rho(\mathbf{a} \cdot \mathbf{v})$ energy source term. $M(t)$ is capped to a maximum of 1000 representing the optically thin limit of the force in a B type star (Drew *et al.* 1998).

In order to calculate the vector flux from the disc it was discretised into a number of regions and each of these are individually treated as a point source (note that throughout this section R and z refer to the cylindrical co-ordinates used in the hydrodynamic simulation and (r, θ, ϕ) refer to the 3D spherical co-ordinates used in calculating the luminosities - see figure 4.6). For each disc model the flux was calculated at 120 points in r (logarithmically spaced between 1 and $10 R_*$) by 60 points in ϕ (linearly spaced between 0 and π) in the plane of the disc. Using the method outlined in equations 4.10 the flux from each discretised point was calculated for $100 \times 100 R, z$ positions. At each of these points we have a 120×60 array of R and z flux components, one from each discretised disc point. In the hydrodynamic simulation each cell looks up the closest point to its position in the 100×100 array and then calculates a velocity gradient along the line of sight to each disc point in order to calculate $M(t)$. However calculating 7200 velocity gradients and line force multipliers for each hydrodynamic cell at each timestep would be prohibitively computationally expensive. Before the simulation begins the flux component arrays are averaged by a factor of 8 in the radial direction and 4 in the ϕ direction (i.e. for the first element in the final array the fluxes from the first 8×4 elements of the array are summed and assumed to come from

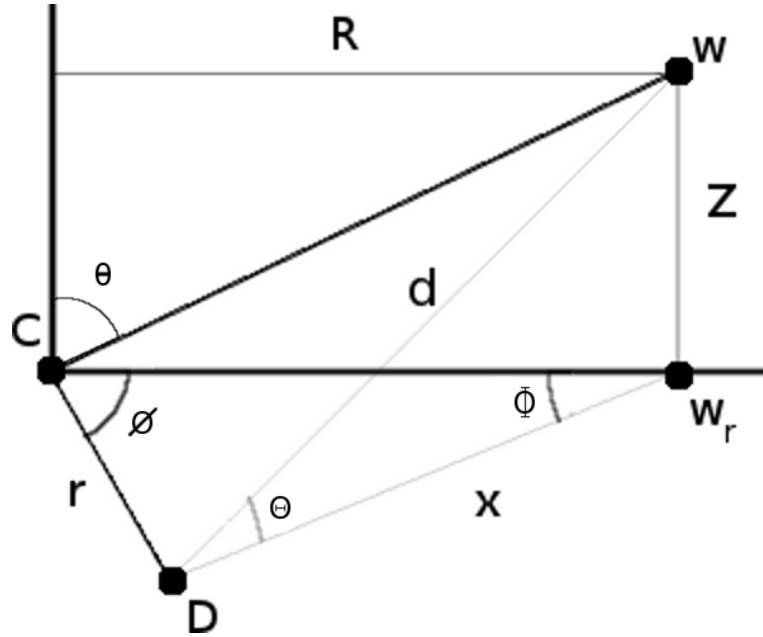


Figure 4.6: The geometry used in the pre-calculation of the disc fluxes. R and z are the cylindrical co-ordinates in the plane of the simulation. r and ϕ are the polar co-ordinates of disc points in the mid-plane of the disc. w is the point in the simulation (wind point) that the flux is being calculated for and D is the disc point whose flux component is being calculated. w_r is the projection of w onto the r, ϕ plane, x is the distance between D and w_r , Θ is the inclination of w from D and d is the distance between D and w .

the center of these points). This means that only a 15×15 array of fluxes is stored for each of the 100×100 simulation plane co-ordinates.

In the pre-calculation of the disc fluxes we make the assumption of axis-symmetry, meaning the R and z components of the flux from a point at ϕ are equal to that of a point at $2\pi - \phi$ and that the ϕ components of the flux cancel. This allows us to not store the ϕ component of the flux and store a value of twice the calculated values for the R and z components, representing both the flux from the point and from its mirror on the other side of the disc. Figure 4.7 shows flux vectors for a single point of the discretised disc, i.e. the field of the vector flux

from one of the 15x15 array of pre-calculated flux fields. Figure 4.8 shows the magnitude of the total flux from all disc points with the arrows showing the vector direction, notably this vector field has a significant θ component in comparison to the purely radial stellar field. Finally figure 4.9 shows the total star + disc flux vectors, showing a much more radial field than figure 4.8, but still with a significant θ component near the star/disc boundary at (1,0) (this does not take into account the shadowing of the disc by the star, so that disc elements of the opposite side of the protostar are contributing to the flux at the stellar surface. However, this shadowing is calculated at runtime in the hydrodynamics step).

Equations 4.10 describe how the disc's component fluxes are calculated before the simulation is started (see figure 4.6 for reference to the geometry). The intensity of the disc at a given radius, $I(r)$, is the sum of the accretion luminosity of the disc and the incident stellar radiation upon it (assuming the disc is geometrically flat and that all the energy from the starlight is absorbed and re-emitted locally). In equation 4.10e the terms in the brackets are for the intrinsic accretion luminosity of the disc and the luminosity due to reflected starlight respectively and x is the ratio of stellar luminosity to accretion luminosity, see Proga *et al.* (1998) for the derivation.

$$\Theta = \arctan(z/x) \quad (4.10a)$$

$$x = R^2 + r^2 - 2Rr \cos(\phi) \quad (4.10b)$$

$$r/\sin(\Phi) = x/\sin(\phi) \rightarrow \quad (4.10c)$$

$$\Phi = \arcsin[r.\sin(\phi)/x] \quad (4.10d)$$

$$I(r) = \frac{3GM_*\dot{M}}{8\pi^2r_*^3} \times \left[(r_*/r)^3 \times (1 - \sqrt{r_*/r}) + \right. \\ \left. x/3\pi \left(\arcsin(r_*/r) - (r_*/r)\sqrt{1 - (r_*/r)^2} \right) \right] \quad (4.10e)$$

where $x = L_*/L_{acc}$

$$F_R = I.a.\cos(\Phi).\cos(\Theta)/d^2 \quad (4.10f)$$

$$F_z = I.a.\sin(\Theta)/d^2 \quad (4.10g)$$

In addition to the flux from the disc, the stellar flux is included in the source terms as coming from a point source at the origin, with a correction made to the force multiplier to account for the fact that the flux from the star is not all in the radial direction:

$$\tilde{M}(t) = M(t) \frac{2}{1 - \mu_*^2} \times \int_{\mu_*}^1 \frac{(1 - \mu^2)v_r/r + \mu^2 dv_r/dr}{dv_r/dr} \mu d\mu \quad (4.11)$$

where $\mu_* = \sqrt{1 - (r_*/r)^2}$ is the cosine of the opening angle of the cone whose base is the visible portion of the protostar and whose point is at the hydro cell (see Pauldrach *et al.* (1986) for details and derivation).

In regions of the model greater than $10R_*$ from the centre, the line driving force

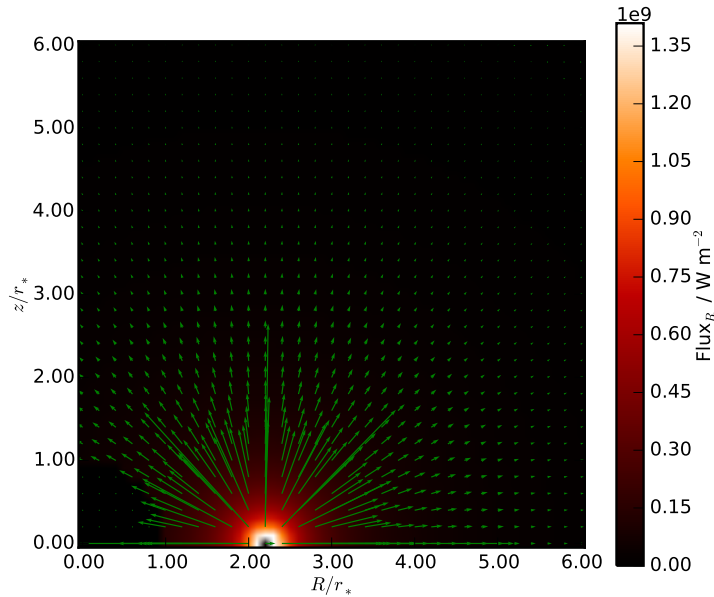


Figure 4.7: The flux vectors from a single point of the discretised disc of the R5.5 model.

is simplified in order to speed up the calculations. Instead of calculating individual lines of sight to elements within the disc and taking the velocity gradient along that line to get individual force multipliers, the luminosity of the disc and star are summed together and a single force multiplier is calculated assuming all the flux comes from a point source at the origin of the model (see fig. 4.10). In the region of the simulation up to $30r_*$ tested, the difference between the two line force calculation methods differed by at most a factor of $\lesssim 2$ per cell. However the simplified method does not systematically give larger or smaller accelerations, and we find that the sum of the accelerations over this region with the simplified method was within 1% of the full calculation. Thus this approximation does not introduce any significant error. However, we use it as it speeds up the calculation by a factor of ~ 5 in the cells where it is used.

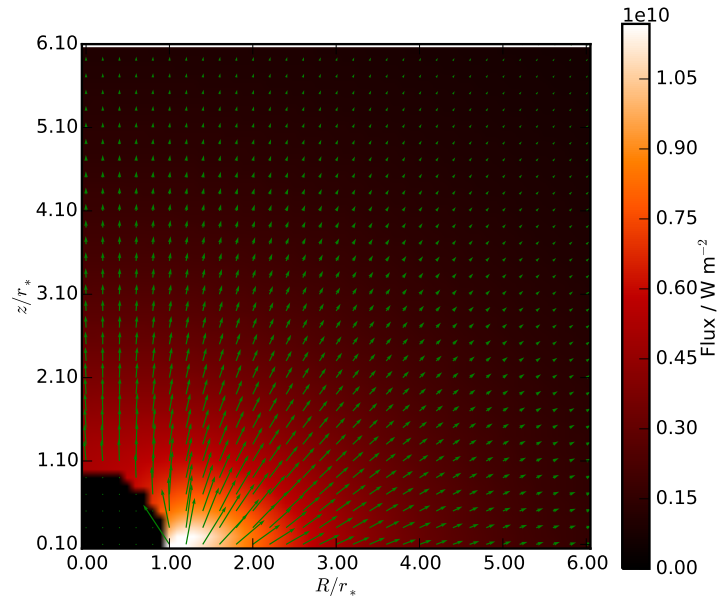


Figure 4.8: The total disc flux vectors from reflected/reprocessed starlight and accretion heating for the R5.5 model.

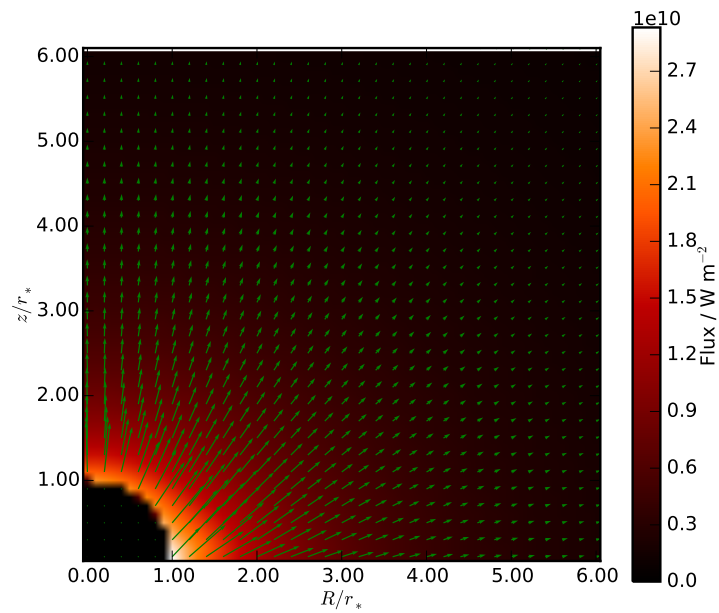


Figure 4.9: The total flux vectors including disc and stellar contributions for the R5.5 model.

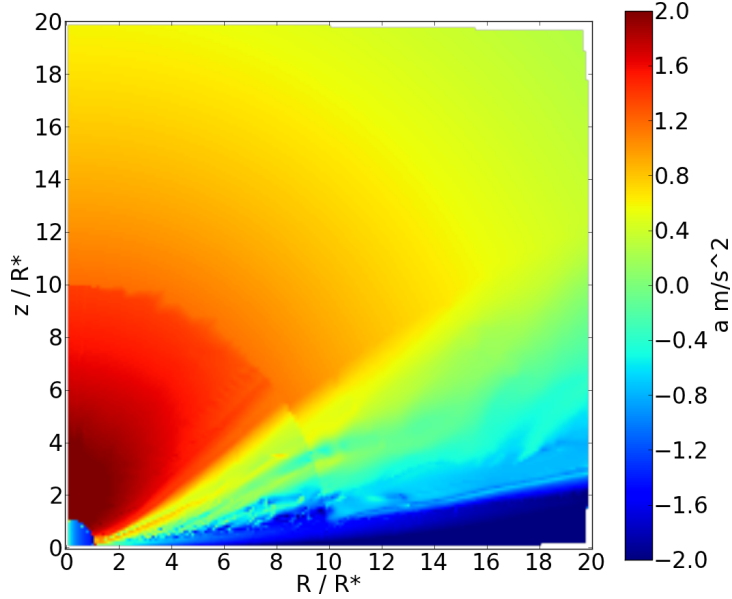


Figure 4.10: A snapshot of the total non-hydrodynamic acceleration (line driving force + gravity + centrifugal force) in $\log(\text{ms}^{-2})$. The change in radiation force calculation method at $10 R_*$ is noticeable but not pronounced.

4.3 Analysis

In order to perform analyses of the simulation results, a snapshot of the models at $t=2 \times 10^8 \text{s}$ were linearly interpolated onto regular $1500 \times 1000 R, \theta$ grids. All results and graphs throughout this section and the following results section are taken from these interpolated grids.

As the main way discs such as these and their winds are observed is through bremsstrahlung and recombination line emission, it is important to work out which regions of the system will be ionised and therefore visible. In order to calculate the ionization of the gas in the model a simple prescription was used where the gas is fully ionized up to the point where the total number of hydrogen recombinations along a column of material equals the number of ionizing photons

entering it. The gas is assumed to be partially ionised after this point, with the fraction ionised equal to the fraction of atoms with energy $>13.6\text{eV}$ for the temperature of the cell. The number of ionizing photons emitted per square metre is given by

$$n_\gamma = \int_{3.3 \times 10^{15}}^{\infty} \frac{B(\nu, T)}{h\nu} d\nu, \quad (4.12)$$

where B is the black body function evaluated at the effective surface temperature of the protostar and $h\nu$ is Planck's constant times the frequency, which is the energy of a single photon at that frequency. The interval starts from the frequency of a photon with energy equal to the ionisation potential of hydrogen (13.6eV) and goes to infinity.

In the first cell to have a greater number of recombinations in the column than ionizing photons emitted, we set the ionization fraction to the ratio of photons entering that cell to the number of recombinations within it. This gives an ionization fraction of the j^{th} cell in the r direction along a line of constant θ as:

$$I_j = \begin{cases} 1 & \text{if } \sum_{i=0}^j (n_i^2 r_i^2) drX \leq n_\gamma, \\ \frac{n_\gamma - \sum_{i=0}^{j-1} (n_i^2 r_i^2) drX}{n_j^2 r_j^2 drX} & \text{if } \sum_{i=0}^j (n_i^2 r_i^2) drX > n_\gamma \text{ and } \sum_{i=0}^{j-1} (n_i^2 r_i^2) drX < n_\gamma, \\ 0 & \text{elsewise,} \end{cases} \quad (4.13)$$

where n_i and r_i are the number density and spherical radius for the i^{th} cell, dr is the width of the cells, X is the Hydrogen recombination coefficient taken at 10^4K and n_γ is the number of photons with energy $>13.6\text{eV}$ emitted per square meter

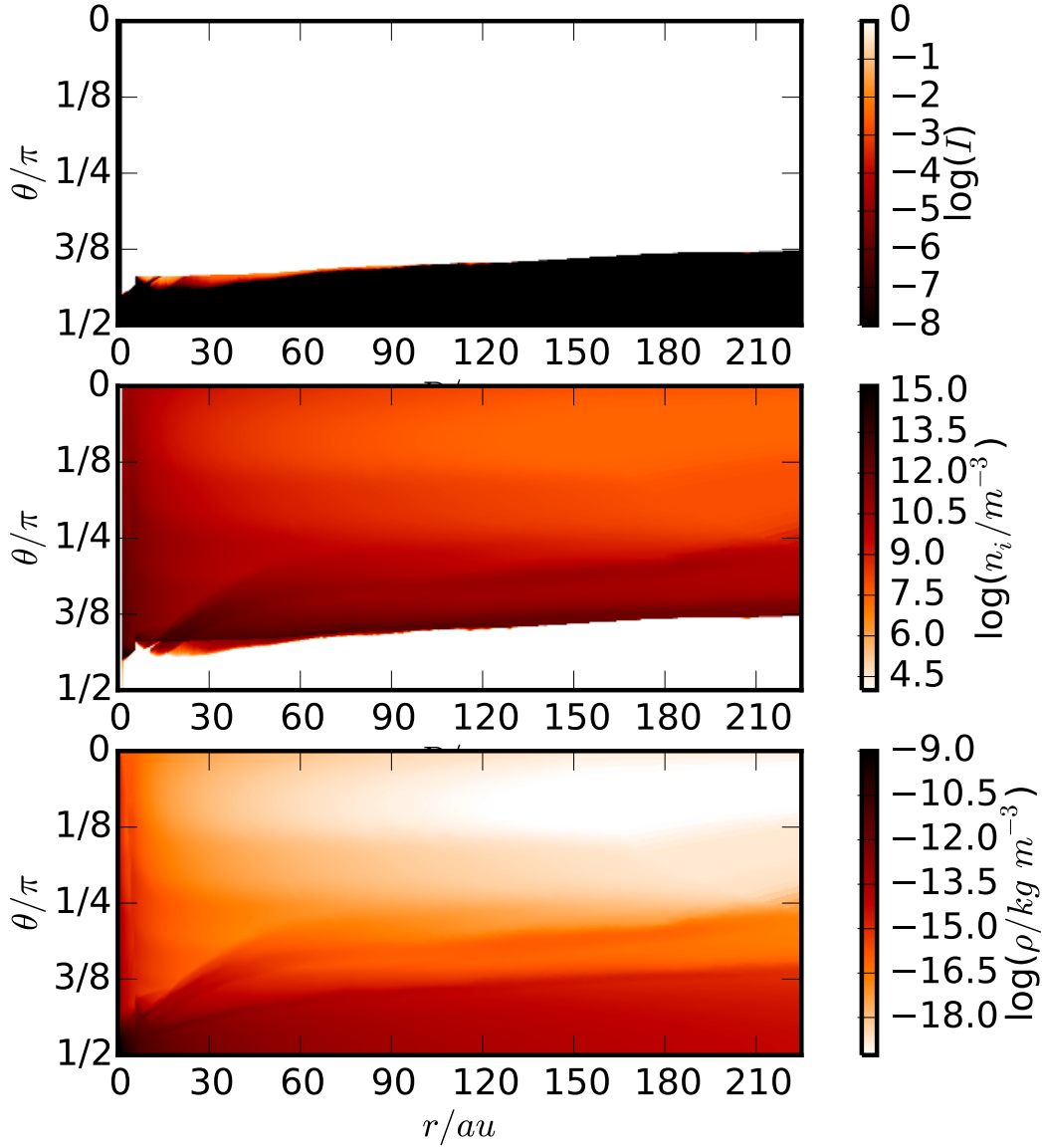


Figure 4.11: The ionisation fraction (top), mass density (bottom) and their product divided by the mean atomic mass, the number density of ions (middle), for the R5.5 model.

from the star's surface (calculated using equation 4.12). In addition to this, the column of recombinations is reduced by the fraction of atoms expected to have energies greater than 13.6eV owing to their thermal energy,

$$I_{i,th} = \exp(-13.6\text{eV}/k_B T). \quad (4.14)$$

Taking this into account n_i is replaced by $n_i(1 - I_{i,th})$ in equation 4.13 and the ionisation fraction becomes $I_{i,th}$ in cells where it would otherwise be zero (see figure 4.11).

4.4 Model Results

Figure 4.12 shows the final density distributions for each of the large scale models after 2×10^8 s (~ 6.3 yrs) of evolution. This is roughly equal to 10 crossing times of the fast component of the wind and in all the models it is sufficient for the model to settle down to a steady state. Figure 4.13 shows the density, rotational velocity (v_ϕ), wind velocity ($v_w = \sqrt{v_R^2 + V_z^2}$) and emission measure ($n_i^2 V$) for each of the models as a function of the polar angle theta ($\theta = \arctan(R/z)$, see figure 4.6) at a constant radius $r=270$ au. In each of the models where a wind is driven the system can be split up into 3 regions: a bound disc with a nearly Gaussian density distribution, Keplerian (or close) rotational velocity not changing quickly with θ and negligible wind velocity (roughly between $\theta = 3\pi/8 - \pi/2$); a disc wind with density decreasing and velocity increasing at higher latitudes and rotational velocity nearly constant close to Keplerian ($\theta \simeq \pi/4 - 3\pi/8$); and a polar wind with little variation in density or wind velocity and rotational velocity quickly dropping to zero. In each case we can see that the bulk of the emission is coming from a region of the disc wind slightly above where the material becomes gravitationally unbound.

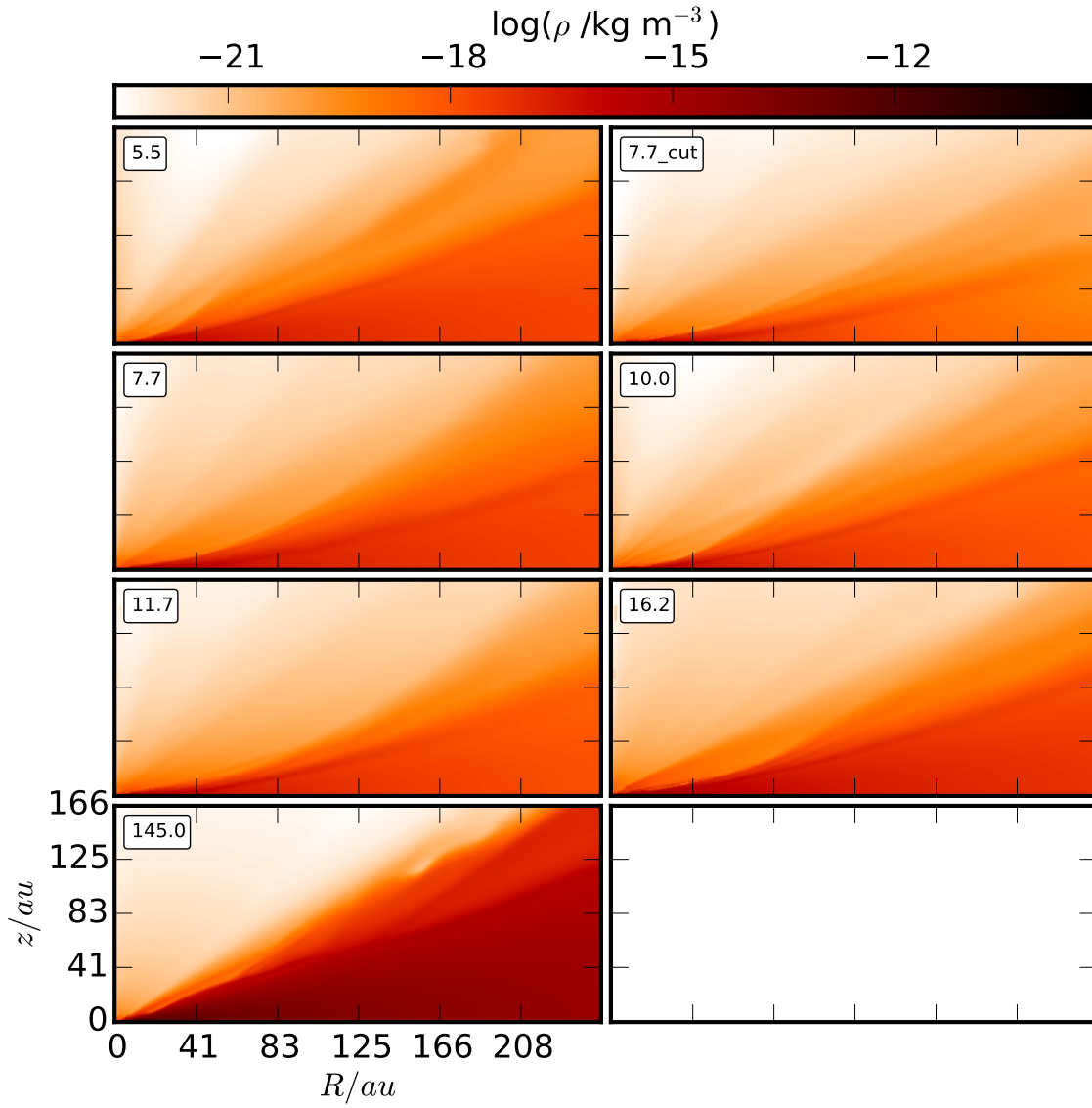


Figure 4.12: Density distributions of the models after 2×10^8 s (~ 6.3 yrs).

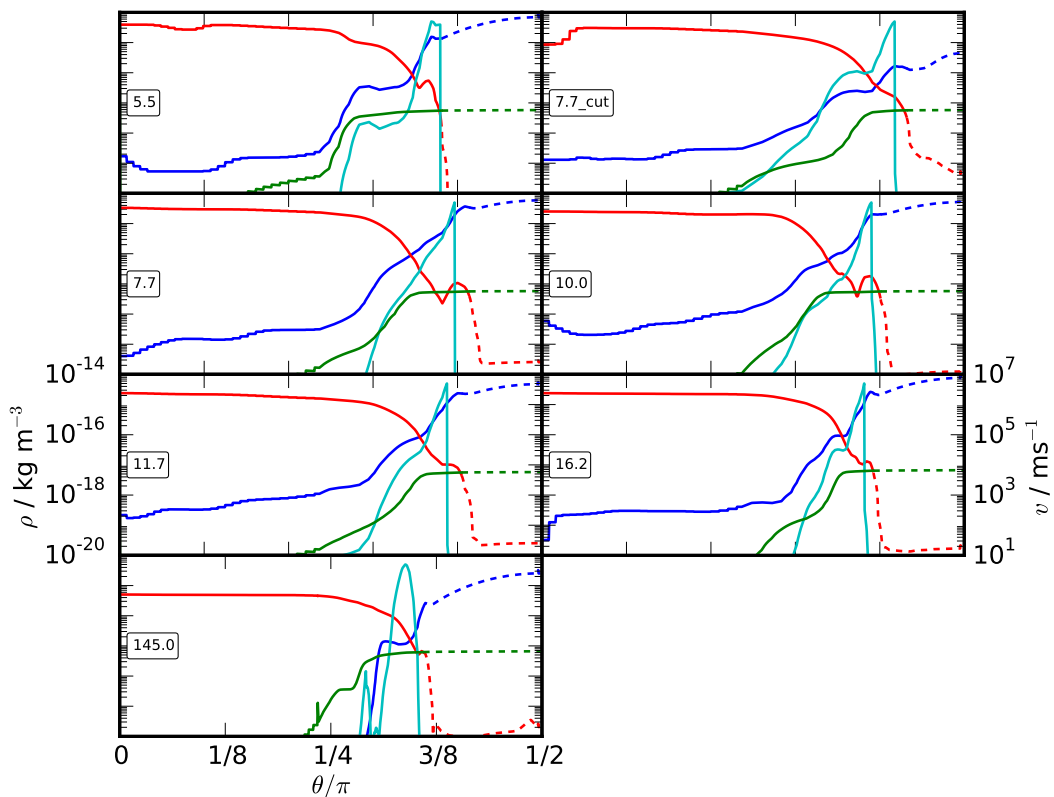


Figure 4.13: Densities (blue line, left axis), velocities in the plane of the simulation (red line, right axis) and in the ϕ direction (green line, right axis) and emission measure (cyan line, arbitrary units) for each of the models as a function of the polar angle θ at a spherical radius of 270 au. Dashed lines indicate regions of the model which are gravitationally bound to the central star.

In order to consistently divide the models into these regions, the following criteria are adopted for them: the disc is defined as the mass which is gravitationally bound to the star, assuming no further radiative acceleration (i.e. $\frac{J^2}{2\rho R^2} + P + \rho v^2/2 \leq \frac{GM_*\rho}{r}$). This also includes some material close to the star which has not yet been driven high enough out of the star's potential well to be unbound - however this region is small ($\lesssim 10$ au), and no further analysis is done on the bound material; the disc wind is defined as unbound material which has at least $1/10^{\text{th}}$ of the specific angular momentum required to be in a Keplerian orbit

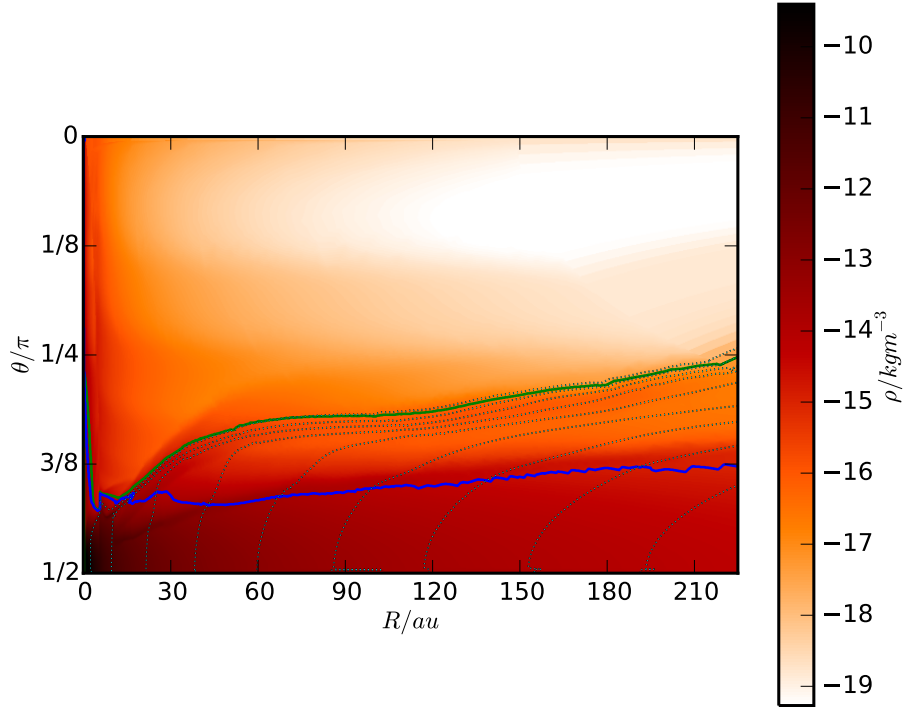


Figure 4.14: The regions of the model used in the analysis. Material below the blue line is bound to the star (assuming no further radiative acceleration). Material between the blue and green lines is unbound but has significant angular momentum and this is referred to as the “disc wind”. Material above the green line is the polar wind. The dotted lines show lines of constant specific angular momentum.

in the disc mid-plane at that radius; and the polar wind is defined as unbound material with less angular momentum than this. Figure 4.14 shows an example of these regions and figure 4.15 shows the regions for each model. In some of the models there is a noticeable discontinuity at $R=7.5$ au, which is where the input from the inner model is used as a boundary condition to the outer model. Due to the two having different equations of state, there will be a mismatch between either the temperatures or the pressures on either side of the fixed region, causing a slight discontinuity in the disc at this point.

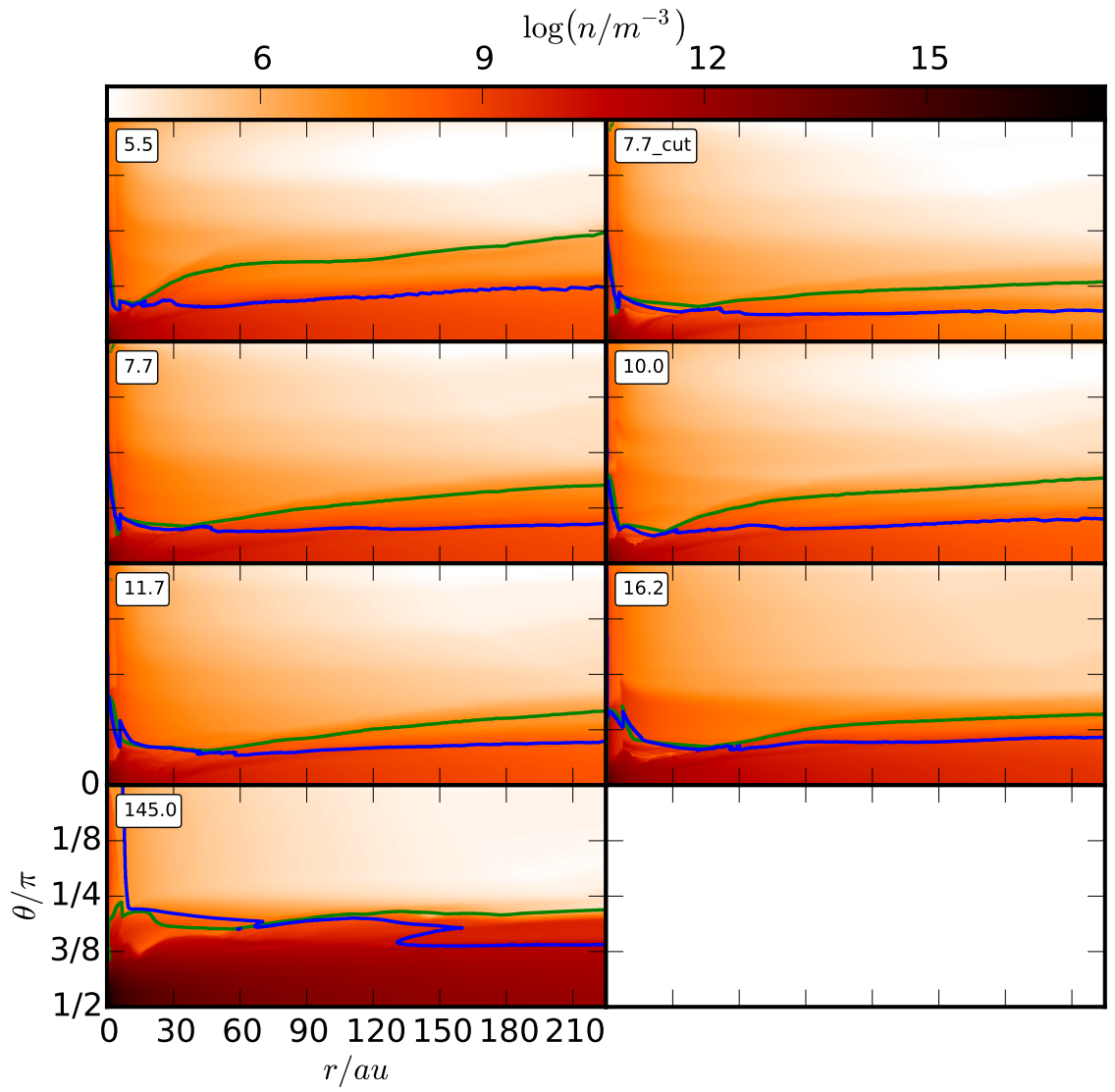


Figure 4.15: as fig 4.14 for each model.

Figure 4.16 shows the total mass loss rate for each of the models and the division of the mass loss between the disc wind and the polar wind, as a function of stellar radius. There is a general trend that the models with smaller stellar radii have greater outflow rates. Also the amount of mass outflow in the disc rather than the polar wind increases for smaller stellar radii. For the range of stellar temperatures between the R11.7 model and the R5.5 model (16200K to 23700K) both the k and α line driving parameters decrease (see figure 4.5), which is seemingly at odds with the increased mass loss seen. However for the smaller protostar there is also more accretion luminosity from the disc itself. For a protostar with mass M_* , luminosity L_* and radius R_* the ratio of stellar to accretion luminosity is:

$$x = \frac{L_*}{L_{disc}} = \frac{2R_*L_*}{GM_*\dot{M}_{acc}}. \quad (4.15)$$

For a $5.5R_\odot$, $8500L_\odot$, $10M_\odot$ star accreting mass at $10^{-4}M_\odot\text{yr}^{-1}$ this ratio is ~ 3 increasing to ~ 9 for a star with a radius of $16.2R_\odot$. The mass flux in the R7.7_cut model (the lower of the two points at $r_* = 7.7$ with a density profile $\propto R^{-1}e^{-R/75\text{au}}$) has $\sim 2/3$ of the mass flux for the R7.7 model. This is despite the total mass in the disc for the R7.7_cut model being less than a quarter of that in R7.7 model and the density at 270 au being a factor of 37 less. This suggests that the majority of the mass in the disc wind is launched from the inner regions of the disc and is not mass stripped from the outer disc.

Figure 4.17 shows the mass and energy distribution between the polar and disc winds. As with the mass fluxes we see a general trend towards the system being more disc dominated for smaller stellar radii. Together these suggest that the

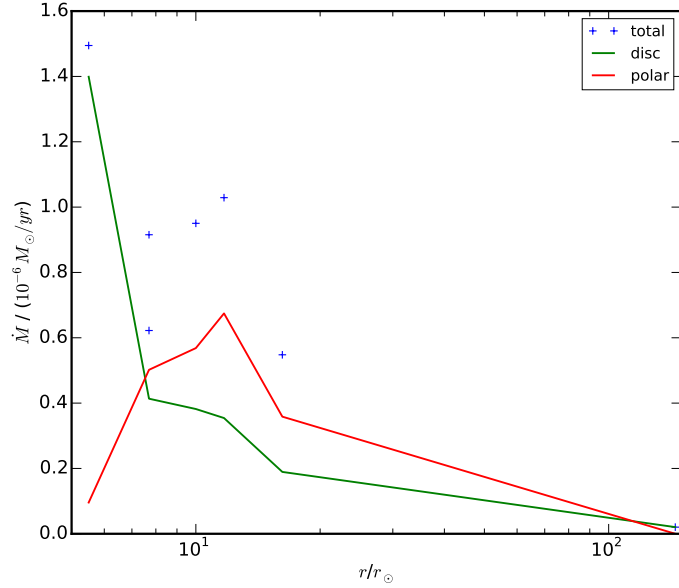


Figure 4.16: The total outwards mass flux from the models and the split between mass lost in the disc wind and that lost in the polar wind, as a function of stellar radius (N.B. the lower of the two points at $7.7r_{\odot}$ is the R7.7.cut model).

increasing disc luminosity for smaller protostars should drive a stronger equatorial disc wind.

Figure 4.18 shows the mass loss rate of the disc and the mean of the disc radiation flux magnitude (within the inner $10r_{*}$). This shows that the total disc flux and mass loss rate follow similar power law profiles. The mean disc radiation flux goes as $R_{*}^{-2.3}$ and the mass loss goes as $R_{*}^{-1.7}$. The remaining discrepancy between these two power laws is likely a mixture of the decreasing k and α for larger radii and the fact that for larger radii protostars the mass is being driven from higher up in the star's gravitational well. The dependence of mass flux from the disc with respect to disc luminosity is

$$\dot{M}_D \propto L_D^{0.7}. \quad (4.16)$$

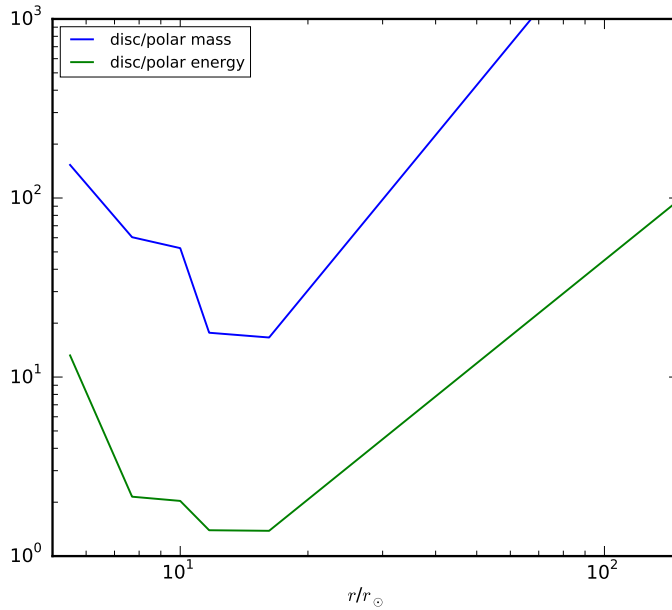


Figure 4.17: The ratio of mass and energy of unbound material in the polar wind and disc-wind regions

This is a significantly weaker than the $L_D^{1.5}$ dependence reported by Proga *et al.* (1998). However the models of Proga *et al.* (1998) were only varying accretion rate and the split of the luminosity between the star and the disc. In the models presented in this work, the stars with higher accretion luminosities, have smaller radii, denser inner discs and hotter inner disc temperatures. Each of these differences can lead to a decrease in the mass loss rate. The smaller radius of the protostar means that the mass in the inner edge of the disc (where much of the mass is launched from) is deeper in the star's gravitational well, and correspondingly needs more acceleration to be launching into the wind. The denser and hotter material also feels less line acceleration (see equation 4.9).

Figure 4.19 shows the cumulative distribution of the mass flux as a function of angle. We can see that the spread of angles over which the mass loss is greatest

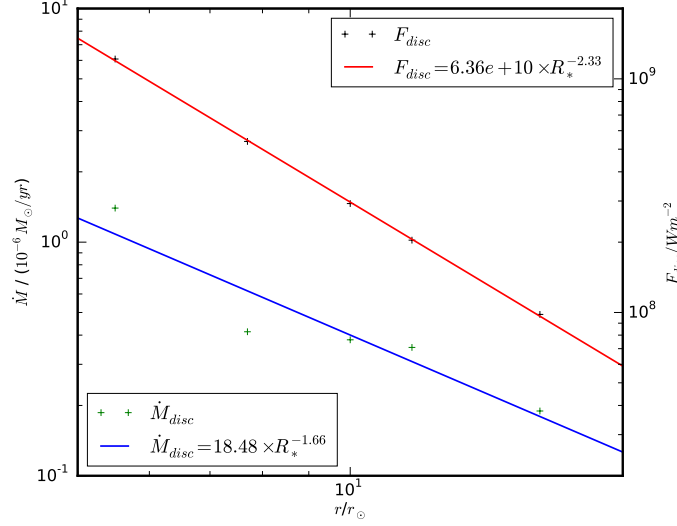


Figure 4.18: The mass loss rate of the disc wind (green points, blue line) and the mean radiation flux from the disc (for $R < 10r_*$).

(i.e. the place where the gradient of these lines is the highest) is limited to between $\theta \simeq 2\pi/5$ and $3\pi/10$, and that the profiles are similar, with the possible exception of the R5.5 model being sharper and having less of a tail at high latitudes than the rest.

Figure 4.20 shows the wind performance parameter, given by

$$Q = \frac{c}{L_*} \oint \rho v_r^2 dA, \quad (4.17)$$

where ρ and v_r are the interpolated density and radial velocity at $270 au$ from the protostar and L_* is the stellar luminosity. This quantity is equal to the ratio of the mass flux driven off the star and disc to the mass flux that would be expected if the momentum from each photon leaving the star were deposited into the wind. That we see values of Q greater than 1 for every model except model R145.0 shows that each photon leaving the star must scatter off multiple lines in the wind in order to

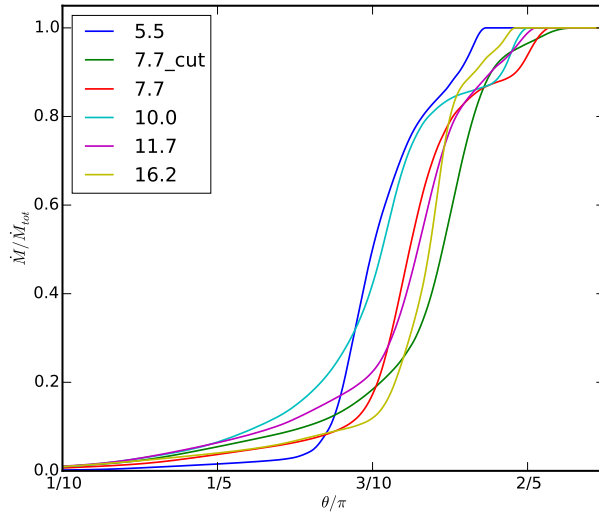


Figure 4.19: Cumulative mass fluxes as a function of latitude angle

drive such mass loss rates. This is similar to Wolf-Rayet stars which show large values of Q , attributed to the layered ionisation structure allowing each photon to scatter multiple times (Abbott & Lucy 1985). This multiple scattering of photons is not possible in spherical winds with homogeneous ionisation structure as there are no two points along a line of sight from the star with the same velocity for a single photon to scatter off. However this is not the case with a wind driven from a disc where a single photon can encounter gas at the same velocity multiple times along its path.

Figures 4.21, 4.22, 4.23 and 4.24 show the total and rotational velocity for material in either the disc or polar wind using different weighting functions. The value given for a set of weights w is:

$$v = \sum_i \left(\frac{v_i w_i}{\sum_j w_j} \right), \quad (4.18)$$

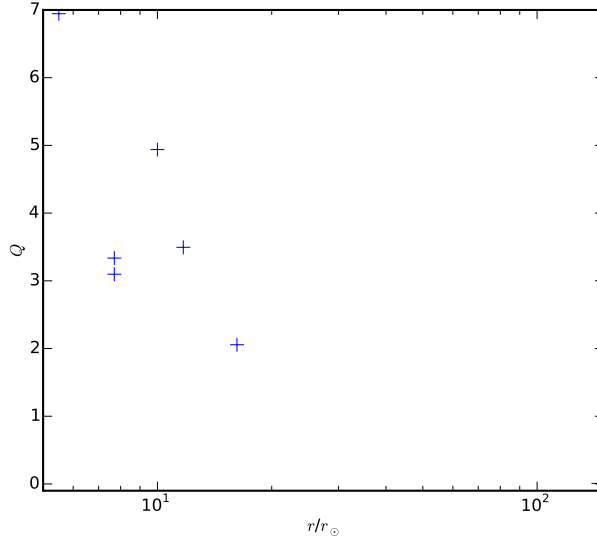


Figure 4.20: The wind performance parameter for each of the models.

and the weights used are the cell volume (V), the cell mass (ρV) and emission measure ($V\rho^2 I^2$), where I is the ionisation fraction as defined in equation 4.13. The emission measure is proportional to the amount of free-free emission that would be emitted from the cell if we assume the model is optically thin.

Though little trend with R_* is seen in the volume weighted velocities of the disc wind (figure 4.21), in the emission weighted ones (which take into account the ionisation structure) the disc wind appears to be flowing faster for larger protostellar radius. This is despite the fact that the mass flux through the disc drops consistently with increasing protostellar radius through all the models (see figure 4.16). This is probably resulting from the decreased amount of ionising photons emitted by the larger protostars. Because of this, the regions at the bottom of the disc wind (which are dense and slow) are not contributing towards this measurement and it is instead probing the higher region of the disc wind.

Rotational velocity appears not to vary with protostellar radius for the mass

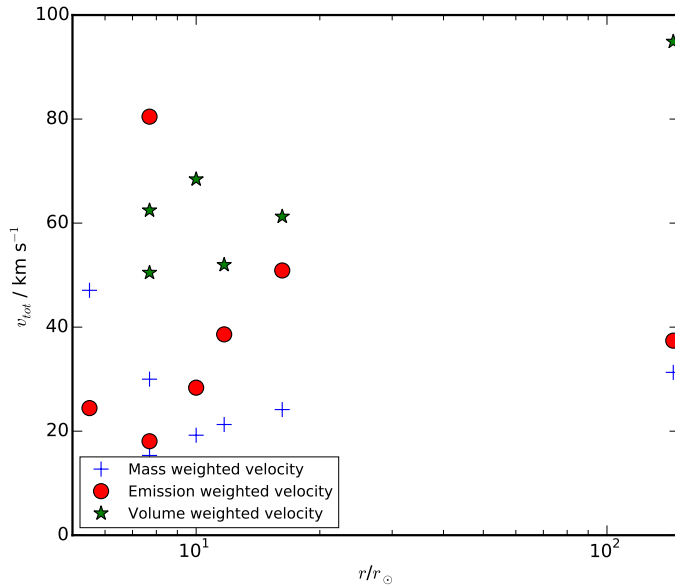


Figure 4.21: The total velocity of the ionised material in the disc wind. Normalised by either the cell volume, the mass of material in cell or the ionised density squared times the cell volume (emission measure). Note that the volume weighted emission for the R5.5 model is off the scale on this figure at $\sim 400 \text{ km s}^{-1}$.

weighting or volume weighting (see figure 4.22, however for the emission measure there is a general trend for lower rotational velocity for larger protostars). This is believed to be the same effect as seen in the total velocity: the emission measure is tracing material higher up in the wind, which will come from smaller radii in the disc and have correspondingly lower specific angular momentum. However this does not explain why the R7.7 and R11.7 models show significantly lower velocities than the rest of the models.

For the polar wind the entire region is ionised. This means that the three different methods are weighted towards different regions of the wind. The emission weighting is biased towards the densest regions, the volume weighted towards the least dense and the mass weighted as an intermediate. In figure 4.23 we

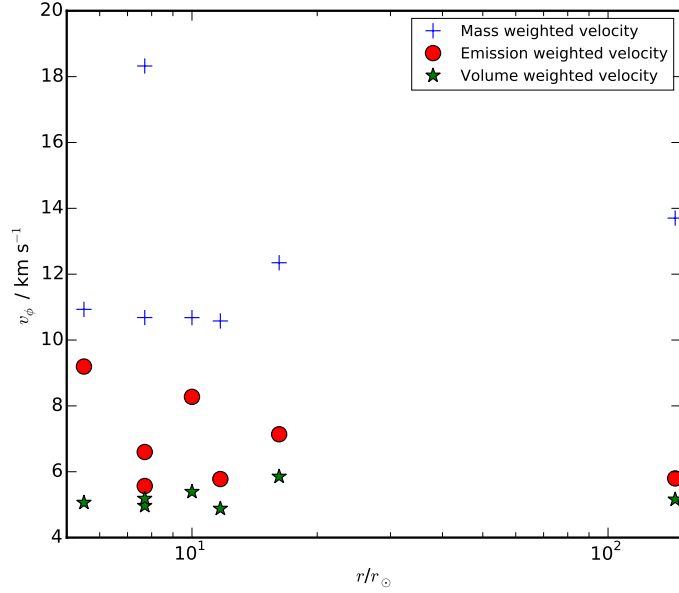


Figure 4.22: The rotational velocity of the ionised material in the disc wind. Normalised by either the cell volume, the mass of material in cell or the ionised density squared times the cell volume (emission measure).

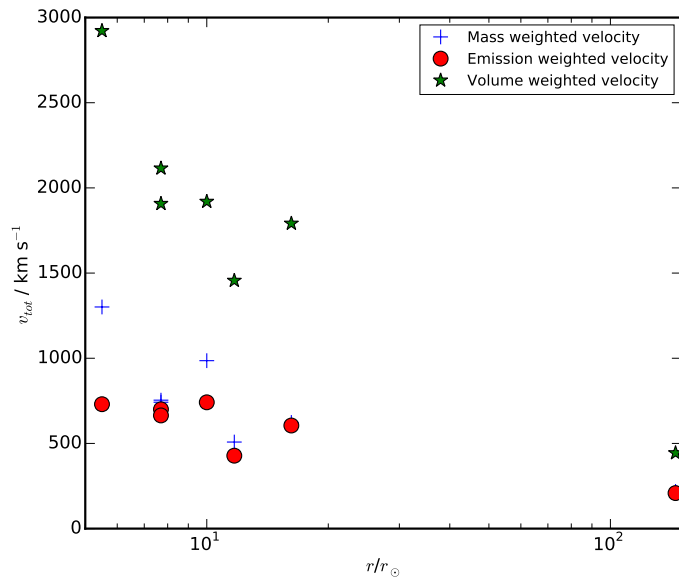


Figure 4.23: The total velocity of the ionised material in the polar wind. Normalised by either the cell volume, the mass of material in cell or the ionised density squared times cell volume (emission measure).

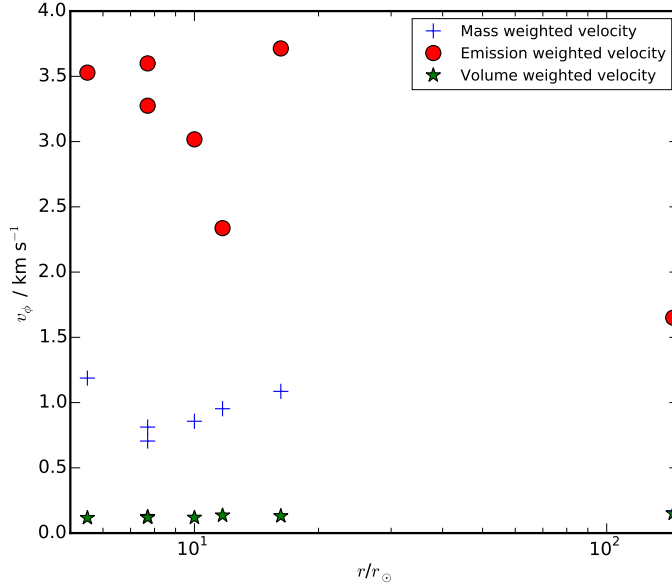


Figure 4.24: The rotational velocity of the ionised material in the polar wind. Normalised by either the cell volume, the mass of material in the cell or the ionised density squared times cell volume (emission measure).

can see that the volume weighted total velocity decreases steeply with increasing protostellar radius. This shows that the terminal velocity of the polar wind is strongly influenced by the radius of the central protostar. The emission weighted velocity, which is more biased towards the denser inner regions of the polar wind also shows slower velocities for larger protostellar radius, but the effect is much less pronounced.

For the rotational velocities of the polar wind (figure 4.24) the first thing to note is that they comprise only a small fraction of the total velocity ($< 1/100^{\text{th}}$ for the emission weighted velocity, showing the greatest proportion in the polar wind c.f. the mass weighted rotational velocity in the disc being $\sim 1/3^{\text{rd}}$). Also the rotational velocities tend not to vary significantly with protostellar radius.

4.5 Conclusions

In this chapter I have presented a series of hydrodynamic models of Keplerian, hydrostatic accretion discs around MYSOs representative of a $10M_{\odot}$ protostar contracting towards the main sequence. In these models the effect of radiation pressure is simulated using local velocity gradients along lines of sight from 225 discrete point sources in the disc and a finite size source for the protostar. The resulting density and velocity distribution after 2×10^8 s (~ 10 crossing times of the fast component of the wind) were analysed in order to calculate the ionised regions and to calculate mass fluxes which could be attributed to either a slow, dense disc wind or a fast rarefied polar wind. The main conclusions are:

- $10M_{\odot}$ protostars can drive at least some disc wind for all disc configurations tested. Mass loss rates for the models are ~ 50 times higher than those seen in Proga *et al.* (1998). This is partially due to the larger simulated area allowing mass loading from further out in the disc, however this comparison between the R7.7 and R7.7_cut models show this can only account for a factor of ~ 2 , the rest of the difference is due to the assumed higher accretion rates and luminosities.
- Models with smaller protostellar radii drive stronger mass fluxes from their discs. This is attributed to the effect of increased accretion and reflected starlight luminosity coming from the discs around smaller stars.
- Mass fluxes from all the models except R145.0 are $\sim 10^2$ higher than would be the case for a spherical wind from these protostars, showing that the presence of a disc can significantly boost the mass loss rate of a young massive protostar.
- Disc mass loss happens mostly from the inner regions of the disc as shown by the modest reduction in the mass loss rate of the R7.7_cut model despite the

significant reduction of its density in the outer regions.

- In the case of bloated protostars (as predicted by Hosokawa & Omukai 2009), disc winds are not driven in their most expansive stage and will not start until the star has contracted and increased its surface temperature.

Radiative transfer of the models presented in this chapter are described in chapter 5. Using these radiative transfer simulations, synthetic observations of appropriate instruments provide predictions of how the models would appear at a distance of 800pc.

Chapter 5

Radiative transfer and synthetic observations of disc wind simulations

5.1 Introduction

Comparisons of models to observations requires looking at observable quantities of the model and simulating how they would be resolved with real instruments from Earth. One of the main observable quantities expected from a MYSO is radio frequency bremsstrahlung emission ($\sim 1-100\text{GHz}$). At frequencies from $1\sim 50\text{GHz}$ this is one of the few types of emission emitted by these deeply embedded objects which reaches us mostly unobscured. An optically thick region of this emission will appear as a black body with a power law spectral index of $S_\nu \propto \nu^2$, and a homogeneous optically thin region will have an index proportional to $\nu^{-0.1}$ (Wright & Barlow 1975). This radio frequency emission when combined with

a value for the terminal velocity for the MYSO's wind can be used to give an estimate of the mass loss rate from the star (e.g. Abbott *et al.* 1980, 1981).

In order to get kinematic information from the disc wind, observations of line radiation need to be employed. Here we consider two possible sources of this information, the bound-bound transitions of hydrogen resulting from relaxation of a hydrogen atom after proton-electron recombination, and the forbidden line transitions of singly ionised carbon. Hydrogen recombination lines in the radio and millimetre wavelengths are commonly observed towards MYSOs (e.g. Simon *et al.* 1983; Lumsden *et al.* 2012; Galván-Madrid *et al.* 2012; Guzmán *et al.* 2014). In addition to the hydrogen recombination lines we also investigate the feasibility of using C⁺ lines as a way of tracing the disc wind. C⁺ is photoionised in similar regions to hydrogen (having an ionisation energy of 11.3 eV in comparison to hydrogen's 13.6 eV), is abundant in the ISM and has multiple forbidden transition lines in the (sub)millimetre regime. These lines have not been used extensively in studies of star formation (though examples do exist - Ossenkopf *et al.* (2015) used the line at 158 μm line to investigate the heating and cooling in the S140 star forming region and Goicoechea *et al.* (2015) used it to map the kinematics of the Orion molecular cloud), however they have been used to a significant extent in studies of the ISM (e.g. Pérez-Beaupuits *et al.* 2015; Velusamy *et al.* 2015).

In this Chapter I present radiative transfer calculations of these three potential methods of observing the simulated disc wind from a 10 M_{\odot} MYSO presented in the previous chapter. Section 5.2 describes the method used to calculate the emission from the hydrodynamic model, section 5.3 presents the solutions to the radiative transfer equation for the three emission methods given, and section 5.4 shows the synthetic observations of the free free emission with the e-Merlin radio

interferometer, using the radiative transfer results from the previous section as the model emission.

5.2 Method

5.2.1 Model interpolation

In order to perform the radiative transfer for the free-free and recombination line emission, we need to have the density, temperature, ionisation fraction and the velocity components at each point in a discretised 3D volume. In order to do this we use the grids from chapter 4 and interpolate these onto a 300x150x150 x,y,z grid (spanning -300 to 300 au in x, 0 to 300 au in y and -150 to 150 au in z). As the model is cylindrically symmetric, we can simulate just one half of the disc and assume the intensity distribution is mirrored in the other half. This means the computation time and memory requirements for each model are halved. The density was then re-scaled so that $\sum \rho^2 V$ for the interpolated cube and the gridded hydrodynamic model were equal (in order to compensate for the interpolation introducing or removing material).

In order to raytrace the cube, it is rotated so that the viewing angle is aligned with one of the axes and a rotation matrix is applied to velocity elements so that they are in the rotated co-ordinate system, see equation 5.1.

$$\begin{pmatrix} u'_x \\ u'_y \\ u'_z \end{pmatrix} = \begin{pmatrix} u_x \\ u_y \\ u_z \end{pmatrix} \begin{pmatrix} 1 & 0 & 0 \\ 0 & \cos \theta & -\sin \theta \\ 0 & \sin \theta & \cos \theta \end{pmatrix}, \quad (5.1)$$

Where θ is the inclination angle, measured between the disc's rotation axis and the line of sight to the observer $u_{x,y,z}$ are the velocity components in the simulation frame of reference and $u'_{x,y,z}$ are the components in the frame of reference with the line of sight from the observer to the object as the z axis. After the cube has been rotated so that the z axis lies along the line of sight from the observer to the object and the velocity components from the hydrodynamic model have been rotated into this frame, the emission and absorption coefficients are calculated for each cell in the cube. The method for calculating these is described in sections 5.2.2 and 5.2.3.

Once the emissivity and absorption coefficients have been calculated the optical depth and source functions can be obtained for each cell and the radiative transfer equation solved. These are then integrated down each column of the interpolated cube in order to get the emission from that part of the model, and together these make the predicted image of the model.

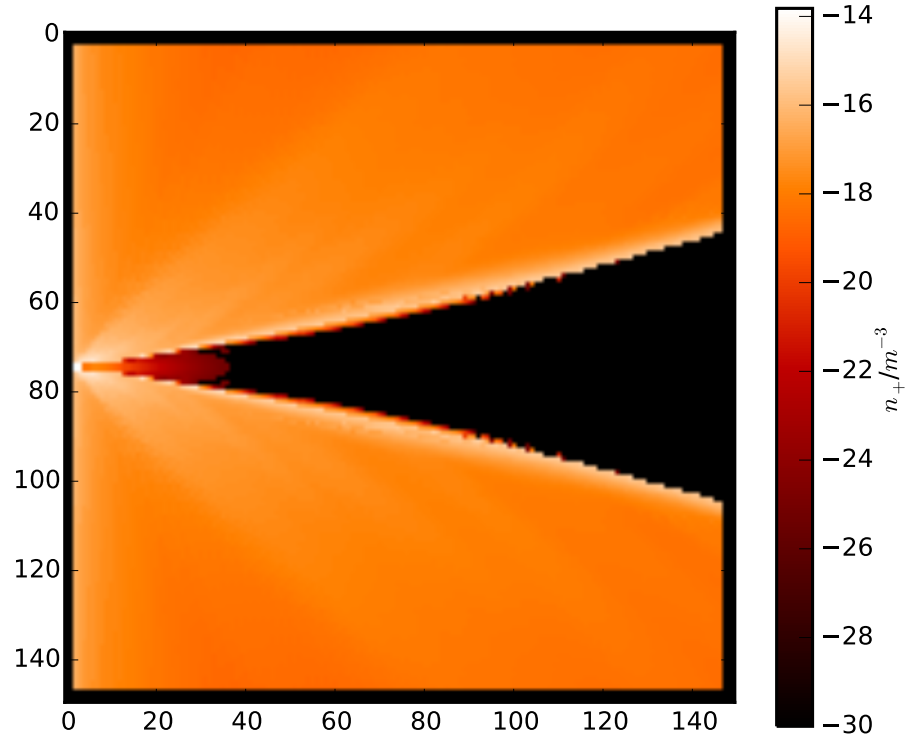


Figure 5.1: The interpolated ion mass density (in g/cm^3) through the centre of the cube used for radiative transfer. The axes labels are in pixel numbers, and each pixel is a cell $(2 \text{ au})^3$.

5.2.2 Bremsstrahlung

In order to solve the radiative transfer equation and make predictions of the radiation that would be emitted by models such as those described in chapter 4 we need to calculate the free-free absorption and emission coefficients. The free-free emissivity and absorption coefficients for a thermal distribution of electron velocities are given by Rybicki & Lightman (1979)

$$\epsilon^{ff} = 4\pi j^{ff} = 6.8 \times 10^{-38} T^{-1/2} n_e n_i \bar{g}_{ff} \exp[-h\nu/k_B T], \quad (5.2)$$

$$\alpha^{ff} = 1.8 \times 10^{-2} T^{-3/2} n_e n_i \nu^{-2} \bar{g}_{ff}, \quad (5.3)$$

where α and ϵ are the absorption and emission coefficients in cgs units, N_+ and N_e are the number densities of electrons and ions (which are assumed to be equal) and \bar{g}_{ff} is the velocity averaged gaunt factor and is a factor of order unity dependent upon T , ν and Z (though as we are only considering free-free emission from electrons interacting with single protons Z is always 1 in these calculations). There is no single formula for \bar{g}_{ff} but there are a number of approximate formulae which are valid in certain regions. In order to simplify the following equations two variables are introduced :

$$\begin{aligned} \gamma^2 &= 1.58 \times 10^5 Z/T, \\ u &= 4.8 \times 10^{-11} \nu/T. \end{aligned} \quad (5.4)$$

The following approximations are used in calculating the gaunt factors in certain regimes.

For $10^{-3} \leq \gamma^2 \leq 10^3$ and $10^{-4} \leq u \leq 10^{3/2}$ Hummer's (1988) approximation uses a two dimensional Chebyshev polynomial to give the gaunt factor as a function of γ^2 and u . If γ or u do not fall into these ranges then if $u < 10^{-4}$ and $\gamma \geq 1$ the long-wavelength approximation from (Scheuer 1960) is used. Here the

gaunt factor is given by a simple expression:

$$\bar{g}_{ff} = -0.55133 (1/2 \ln \gamma + \ln u + 0.056745). \quad (5.5)$$

If this too is inapplicable then one further approximation is tried for $u < 10^{-4}$ and $\gamma < 1$, here the high-energy approximation of Elwert (1954) gives

$$\bar{g}_{ff} = 0.55133 (\ln u + 0.80888). \quad (5.6)$$

If the values of γ^2 and u fall outside of all of these ranges then a value of 1 is assumed (for details of Hummer's approximation and of equations 5.5 and 5.6 see Hummer 1988). Figure 5.2 shows some example values of \bar{g}_{ff} for different values of γ^2 and u .

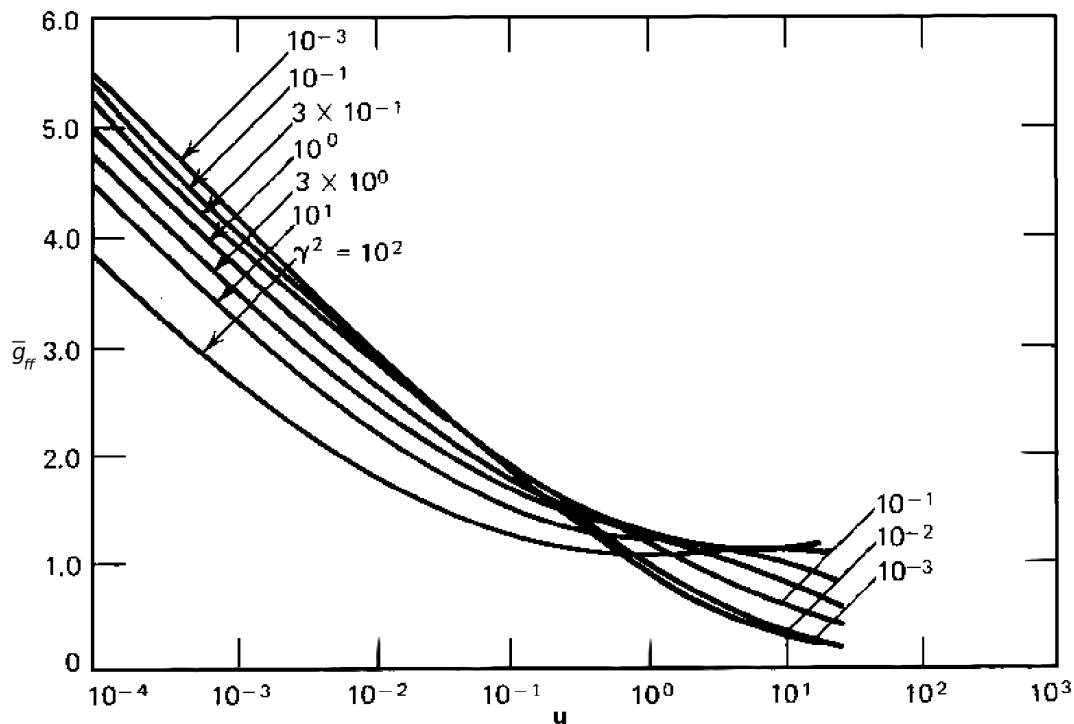


Figure 5.2: The value of the gaunt factor for various values of γ^2 and u , as defined in equation 5.4. Reproduced from Rybicki & Lightman (1986).

5.2.3 Hydrogen photoionisation, recombination and Transition lines

In addition to free-free emission and absorption there are bound-free and free-bound interactions to take into account (i.e. photo-ionisation and radiative-recombination). The absorption co-efficient due to photo-ionisation can be written as (Rybicki & Lightman 1986)

$$\alpha_\nu^{fb} = N_n \sigma_{bf}(\nu), \quad (5.7)$$

where N_n is the number of neutral atoms in the n^{th} electronic state (assumed to be thermalised for the temperature of the gas) and σ_{bf} is the bound free cross

section for a given frequency and is given by

$$\sigma_{bf}(\nu) = \sum_{n=n_0}^{\infty} \left(\frac{64\pi n}{3^{3/2} Z^2} \right) \alpha a_0^2 \left(\frac{\nu_n}{\nu} \right)^3 \quad (5.8)$$

where ν_n is the frequency of the n - ∞ transition ($\nu_n = 13.6 \text{ eV}/n^2 h$), n_0 is the lowest value of n for which $\nu_n \leq \nu$, α is the fine structure constant ($\alpha^{-1} = 137.036$), a_0 is the Bohr radius ($a_0 = 5.29 \times 10^{-11} \text{ m}$) and ν is the frequency of the photon in the frame of reference of the absorbing material ($\nu = \nu_0 (1 - v/c)$) (Rybicki & Lightman 1986).

The emissivity due to radiative recombinations can be given by the product of the number of recombinations to a given level and the energy of that transition

$$j_{\nu}^{fb} = \sum_{n=0}^{\infty} \left(\frac{h\nu_n}{4\pi} N_+ N_e \langle v \sigma_{fb} \rangle \phi(\nu) \right), \quad (5.9)$$

where N_+ and N_e are the number densities of electrons and protons and are assumed to be equal, $\phi(\nu)$ is the line profile function, given by

$$\phi(\nu) \propto \exp \left[-\frac{(\nu - \nu_0)^2}{\nu_D^2} \right]$$

and is normalised so that,

$$\int_0^{\infty} \phi(\nu) d\nu \equiv 1.$$

Here ν_D is the Doppler width due to thermal motions and is equal to

$$\nu_D = \frac{\nu_0}{c} \sqrt{\frac{k_B T}{m_p}}. \quad (5.10)$$

The $\langle v\sigma_{fb} \rangle$ term in equation 5.9 is the recombination coefficient and is given by

$$\langle v\sigma_{fb} \rangle = \int v f(v) \sigma_{fb} dv, \quad (5.11)$$

where $f(v)$ is the distribution of electron velocities. For a Maxwellian distribution of velocities this is

$$\langle v\sigma_{fb} \rangle = 3.262 \times 10^{-6} M(n, T), \quad (5.12)$$

where

$$M(n, T) = \frac{\exp[13.6 eV/k_B T]}{n^3 T^{3/2}} E_1(13.6 eV/k_B T), \quad (5.13)$$

and where

$$E_1(x) = \int_x^\infty \frac{\exp[-t]}{t} dt. \quad (5.14)$$

For bound-bound transitions in hydrogen the method outlined in section 2.1.1 can be used if the assumption of thermalised level populations is made. The Einstein coefficients for the transitions from $n < 11$ are taken from Wiese & Fuhr (2009). Using the approximation of Menzel (1968) for large n oscillator strengths, the Einstein A coefficient can be approximated to:

$$A_{n+1,n} \simeq \frac{8\pi^2 \nu_{n+1,n}^2}{m_p c^3} 0.190775 (1 + 1.5/n) \quad (5.15)$$

In order to get the emission coefficient (using equation 2.2) we also need to know the number of atoms in the upper level of the transition. For this we assume all neutral atoms have thermalised level distributions and add to that the number of recombinations which end up in the upper level.

5.2.4 C⁺ lines

In addition to hydrogen continuum and line emission there are other elements in the material making up the protostar and disc. In particular carbon and oxygen are present in significant amounts (Wilson & Pauls 1984). Ionised carbon and atomic oxygen fine structure transitions in sub-millimetre wavelengths are important coolants in dense regions (Stahler & Palla 2004) and are potentially observable. Of these: ionised carbon is the best candidate to trace the disc wind, which is nearly entirely composed of ionised hydrogen. As the first ionisation energies of carbon and oxygen are 11.2eV and 13.6eV respectively, they should also be ionised in this region.

In order to calculate the emission from the [C⁺] lines at 659.364, 847.903, 1507.27 and 1900.54GHz, LIME was used in a similar way to that described in Chapter 3. For the abundance of C⁺ it is assumed that carbon is ionised in the same places and to the same extent as hydrogen (i.e. $\frac{n_{C^+}}{n_{H^+}} = \frac{n_C}{n_H}$) and the C/H ratio used is the same as that which is observed in the Orion nebula (3.4×10^{-4} , Rubin *et al.* 1991).

In order to allow LIME to accurately calculate the contributions from both the carbon ions and the dust, the density profile from the hydrodynamic model needs to be split up into ionised, atomic and molecular regions. In order to do this, first

the ionisation fraction calculated in chapter 4 is used to split the density between neutral and ionised material. The neutral material then needs to be sub-divided into atomic and molecular components. In order to calculate the proportions of atomic and molecular hydrogen consistently, rate equations for the creation and destruction of H_2 molecules (including photochemistry) would have to be coupled to the hydrodynamic and radiative transfer equations, and this falls outside the scope of this work.

In the millimetre wavelength range, dust provides significant opacity. In order to calculate the dust density profile we assume an initial dust to (neutral) gas mass ratio of $1/100$ and model sublimation by including a factor of $\exp[-T/1500]$ (as in e.g. Ilee *et al.* 2013). In order to split the neutral material into atomic and molecular components we make the assumption that the molecular fraction follows the same profile as the dust destruction, i.e. the fraction of neutral material that is molecular is $\exp[-T/1500]$. Whilst this is a fairly crude assumption, and likely wrong by a significant factor in some regions, the only consequence of the split between the two neutral phases is in how they collisionally excite the C^+ ions. The collisional coefficients differ by at most $\sim 10\%$ and so this simplification should not introduce much error into the calculation of the C^+ line intensities. More importantly, a limitation of LIME is that the amount of dust in the model is set by a constant dust to gas ratio with respect to a single density profile. By fixing the molecular density to follow the same destruction profile as the dust we can create a varying dust ratio throughout the model.

This gives density profiles for the different phases of hydrogen as:

$$\begin{aligned}
n_{H_2} &= n_{tot}(1 - I) \exp\left[\frac{-T}{1500}\right] \\
n_H &= n_{tot}(1 - I) \left(1 - \exp\left[\frac{-T}{1500}\right]\right) \\
n_{H^+} &= n_{tot}I,
\end{aligned} \tag{5.16}$$

where n_{tot} is the density of the chapter 4 models and I is the ionisation fraction.

In order to sample both the dust and ionised regions when emission originates from the sampling in LIME is based on either the ρ_{H_2} compared to $\rho_0/100$ or of the ρ_{H^+} compared to the density of the stellar wind at $2R_*$

The central protostar is modelled as a sphere of constant density at the effective surface temperature required to give a luminosity of $8500L_\odot$. The sphere is created by assigning 5% of points to random positions on a sphere with radius $r = R_*$ and a further 5% in the range $R_* < r < 1.1R_*$. This allows LIME to create a good approximation to a sphere with a sharp boundary for the central protostar.

5.3 Results

5.3.1 Bremsstrahlung

Emission maps have been created for each of the models (other than R145.0, which testing showed was only emitting free-free emission on the order of $1/1000^{th}$ of the other models).

The majority of the free-free emission is coming from the surface of the model where the ionising flux balances the recombination column. This is the region with the highest density of ionised material and as the free-free emissivity is proportional to the ionised density squared it dominates the emission.

It is important to note that inner gaps in the emission is likely caused by shadows thrown from the discontinuity between the inner and outer models, see figure 4.11. Examples of this can be seen in the gaps of the emission in the 5 GHz images (figure 5.6). In this figure the region around $120 < x < 180$, $y < 30$ show a gap in the emission between radii of $20 \sim 60$ AU. Given that in the rest of both the inner and outer models the surface layer is a smoothly flaring surface it seems likely that it is not a real effect.

In each of the subsequent figures the intensity of radiation from one half of each of the disc models is shown for a given inclination angle and frequency. The model number is given in the top left and the integrated flux across the half disc is shown in the bottom left in mJy (the total flux from the disc is assumed to be twice this).

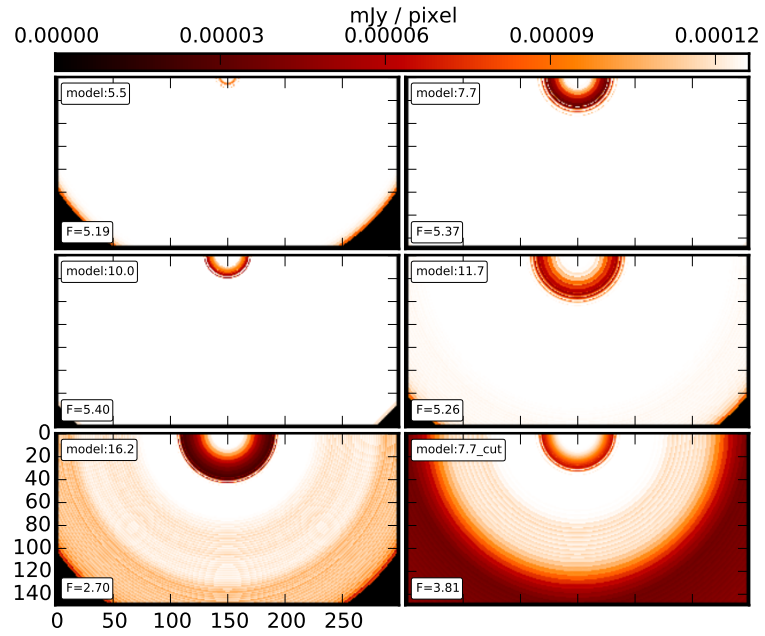


Figure 5.3: Free-free emission for the discs at an inclination angle of 0° and a frequency of 1.5GHz.

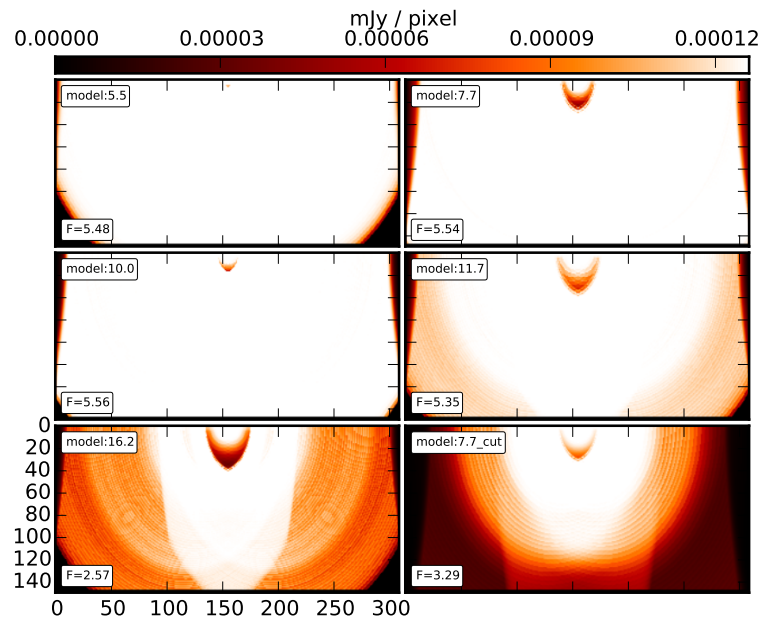


Figure 5.4: Free-free emission for the discs at an inclination angle of 45° and a frequency of 1.5GHz.

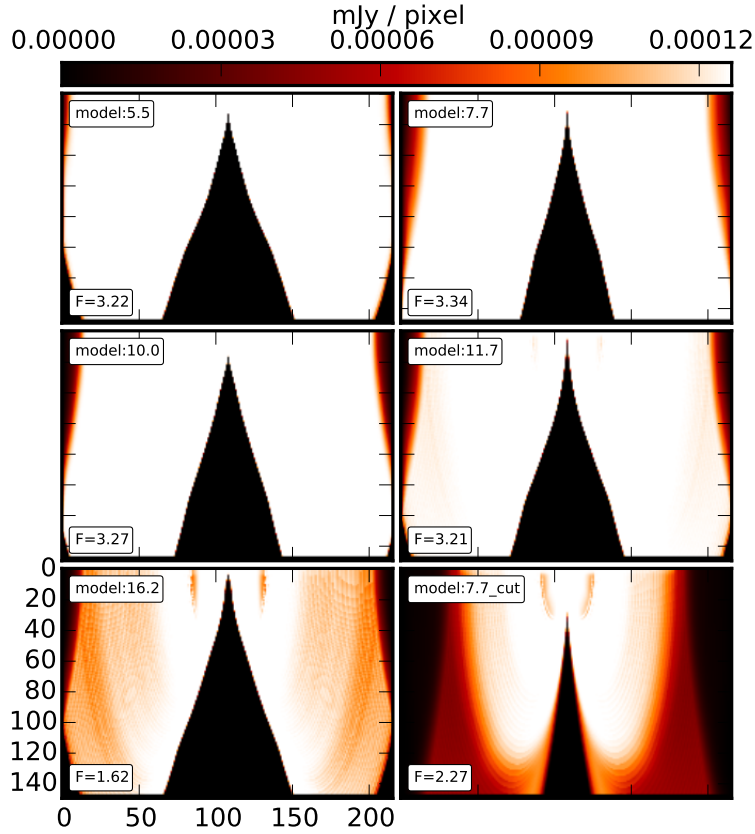


Figure 5.5: Free-free emission for the discs at an inclination angle of 75° and a frequency of 1.5GHz.

For the free-free emission at 1.5GHz, the models are all optically thick for all inclination angles, with the exception of the outer region of the R16.2 and R7.7_cut models. These two models feature the most tenuous outer regions which can become optically thin even at 1.5GHz. However these models are still optically thick in the inner regions and where the inclination angle means that the line of sight passes through the ionisation surface more than twice (see figures 5.4 and 5.5).

In the 5GHz band the emission is optically thinner with only the R5.5 model showing high optical depth and constant intensity across the majority of the disc.

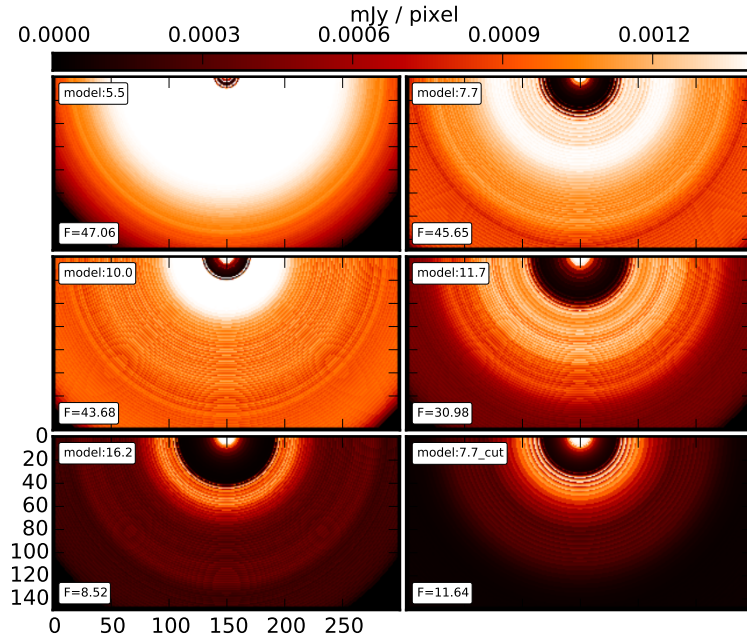


Figure 5.6: Free-free emission for the discs at an inclination angle of 0° and a frequency of 5GHz.

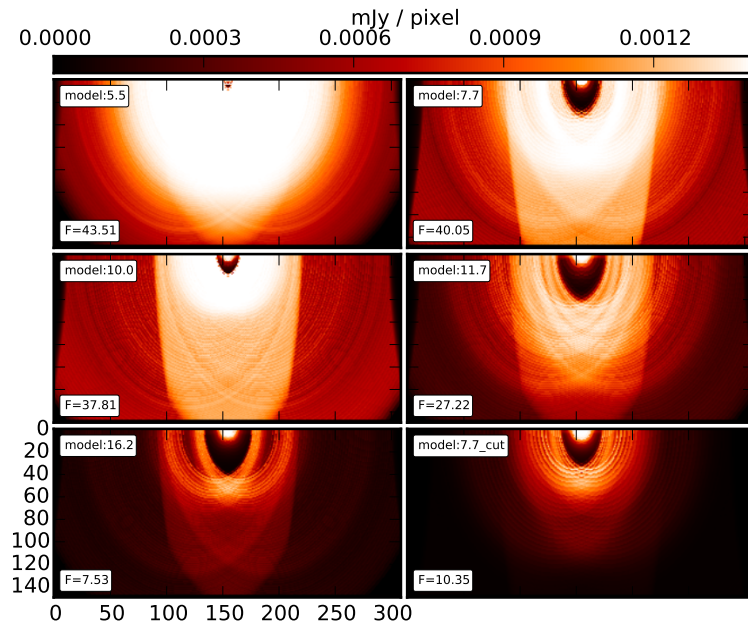


Figure 5.7: Free-free emission for the discs at an inclination angle of 45° and a frequency of 5GHz.

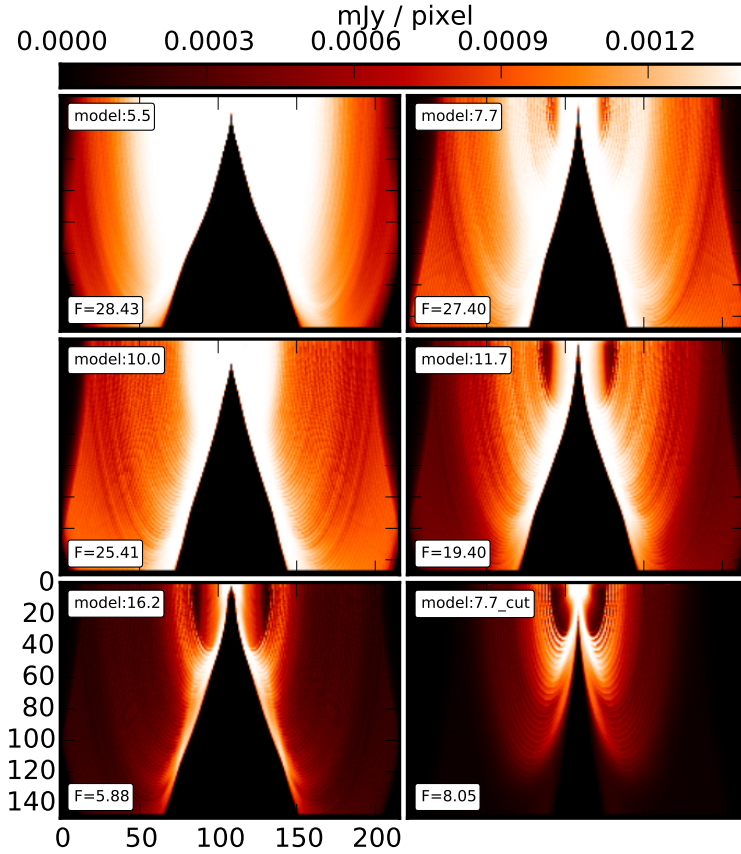


Figure 5.8: Free-free emission for the discs at an inclination angle of 75° and a frequency of 5GHz.

The inner region of each of the models shows optically thick emission coming from the region around the protostar. Also, due to the decreased optical depth, the effective area of emission has decreased compared to 1.5GHz, this is an effect which has been seen in actual observations of MYSOs (Gibb & Hoare 2007).

The 23GHz emission is almost entirely optically thin, with the slight exception of the R5.5 model at 75° (figure 5.11) where the line of sight grazes the ionisation surface. With almost all of the emission being optically thin at 23GHz the emission can be compared with the momentum flux, and the relation between the

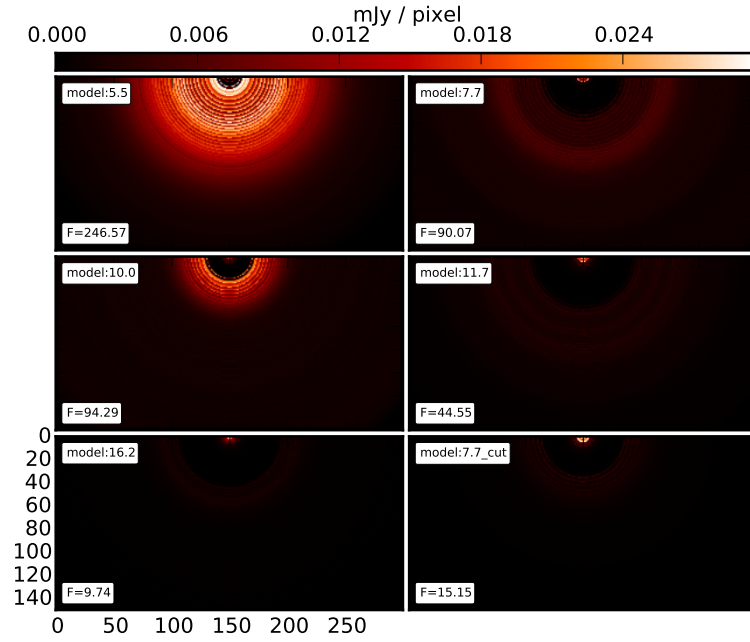


Figure 5.9: Free-free emission for the discs at an inclination angle of 0° and a frequency of 23GHz.

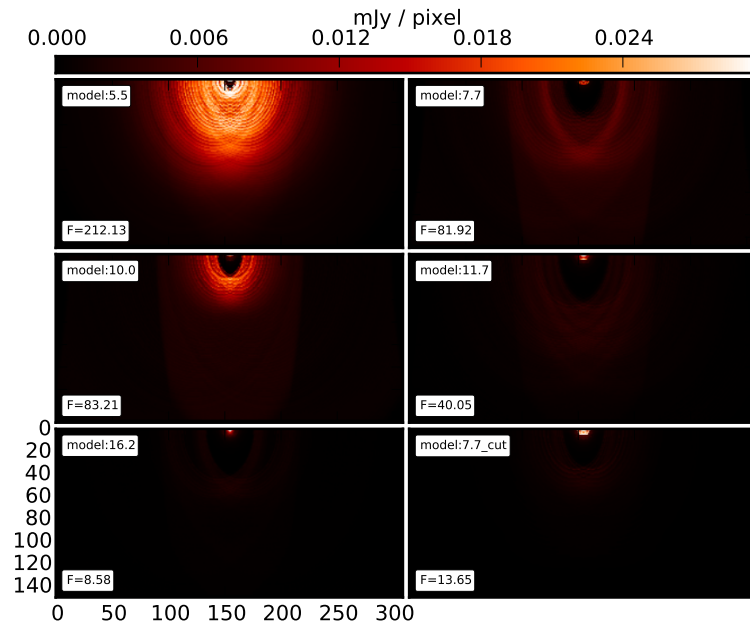


Figure 5.10: Free-free emission for the discs at an inclination angle of 45° and a frequency of 23GHz.

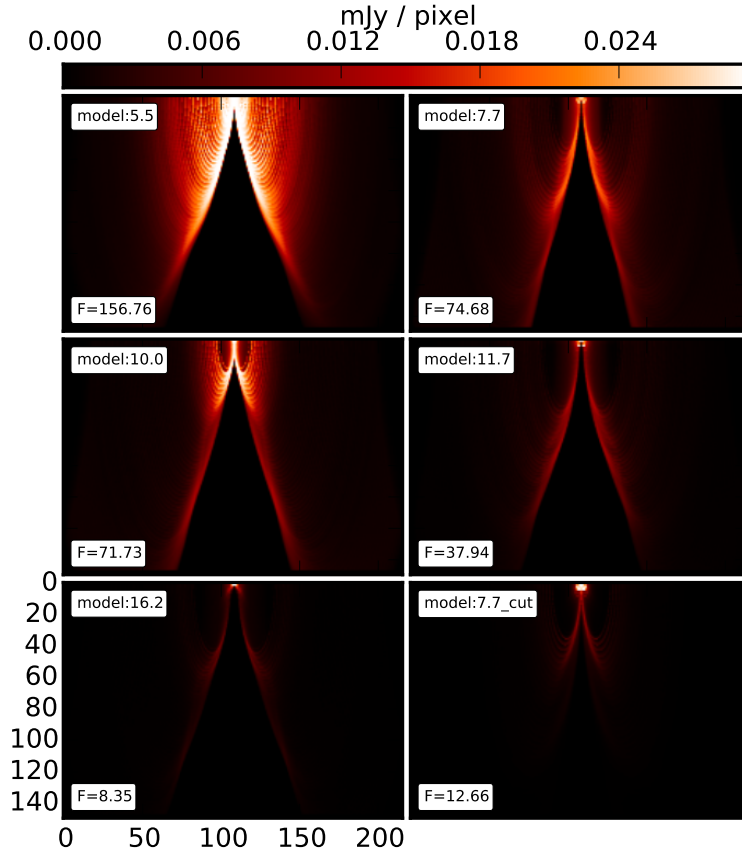


Figure 5.11: Free-free emission for the discs at an inclination angle of 75° and a frequency of 23GHz.

two observed, this is shown in figure 5.12. As there is no single value of v_∞ that characterises the disc wind and polar wind the value used is the emission weighted velocity (as defined in Chapter 4) for the disc wind and the total system. This will include material which is still undergoing acceleration and so is travelling at less than its final velocity, however this will be similar for each model and so should not affect the scaling significantly. From this plot we can see there is a strong dependence of the emitted flux at 23GHz to either the momentum flux from the disc or the entire system. The power law index of 0.82-0.92 is slightly higher than

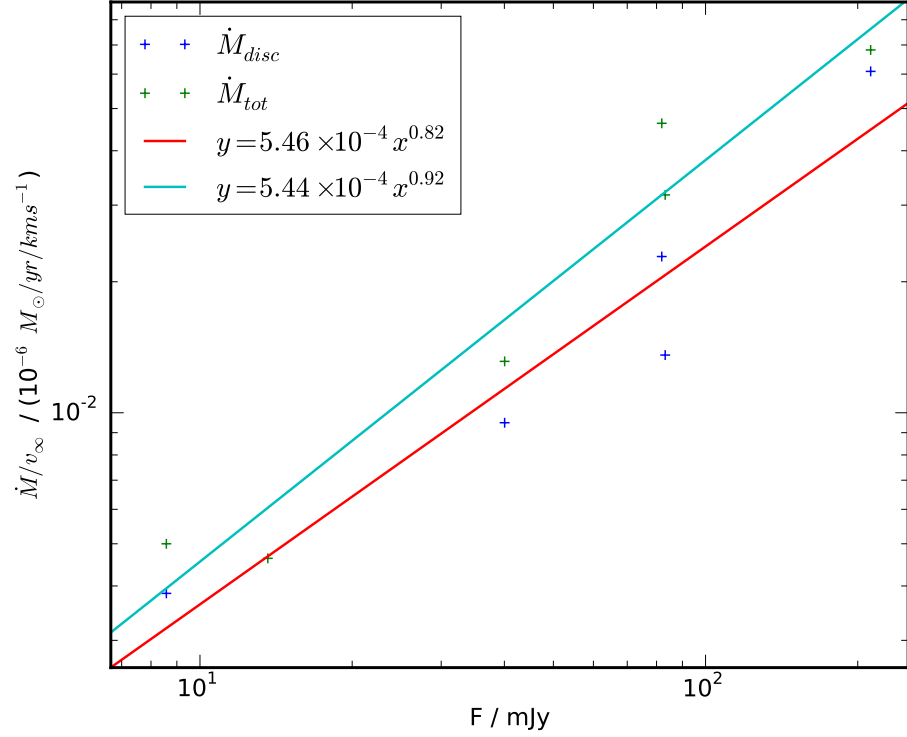


Figure 5.12: The 23GHz flux plotted against the mass flux divided by terminal velocity in the disc wind (blue crosses, best fit red line) and total mass flux (green crosses, best fit cyan line).

the theoretical index of $3/4$ which can be derived for an optically thin, spherically symmetric wind of constant velocity (Lamers & Cassinelli 1999), however this can be understood given the very different geometry of the disc wind.

Figures 5.13, 5.15 and 5.17 show the spectra for each of the models for the 3 inclination angles and figures 5.14, 5.16 and 5.18 show the spectral index of each of the spectra as a function of frequency, where the spectral index is

$$a = \frac{d \log S_\nu}{d \log \nu}, \quad (5.17)$$

In all the inclination angles the spectral index drops from 2 at 1GHz to ~ -0.1

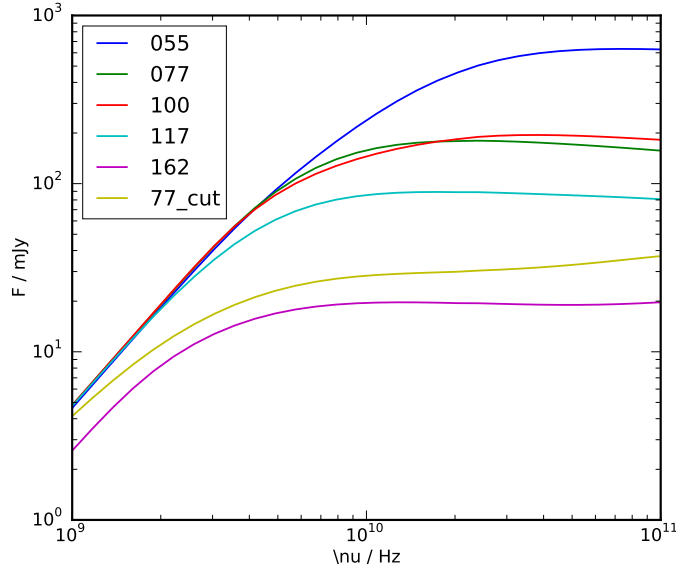


Figure 5.13: The free-free emission spectra for each of the models viewed with an inclination angle of 0°

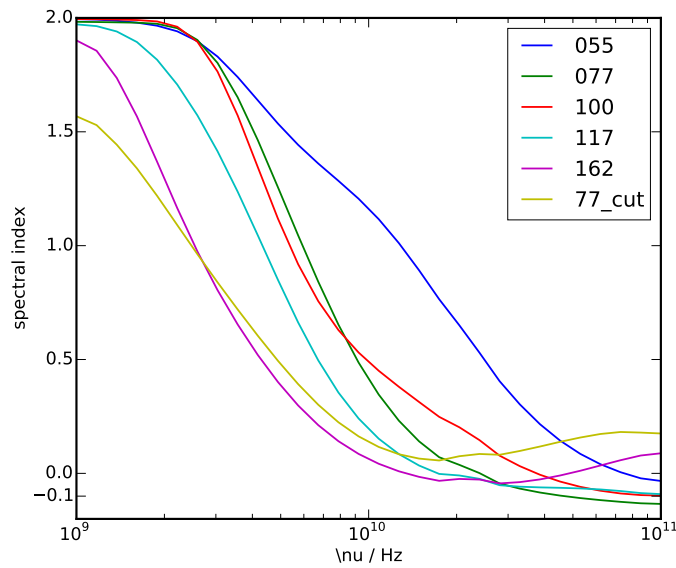


Figure 5.14: The spectral index for each of the models as a function of frequency, for an inclination angle of 0°

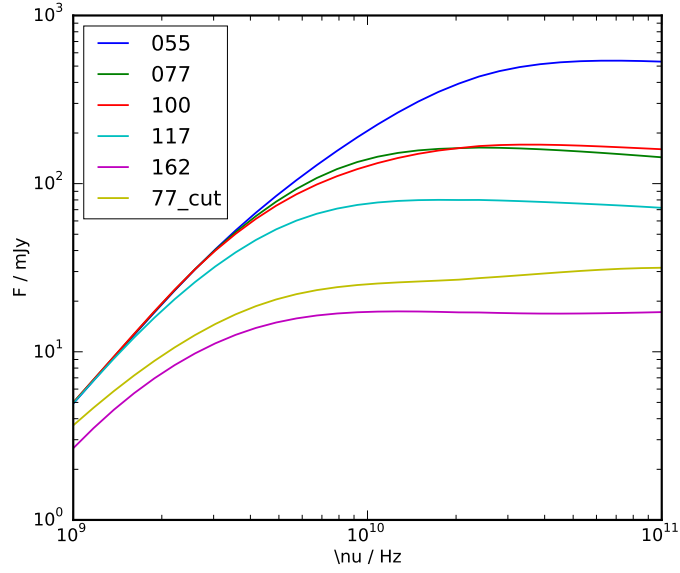


Figure 5.15: The free-free emission spectra for each of the models viewed with an inclination angle of 45°

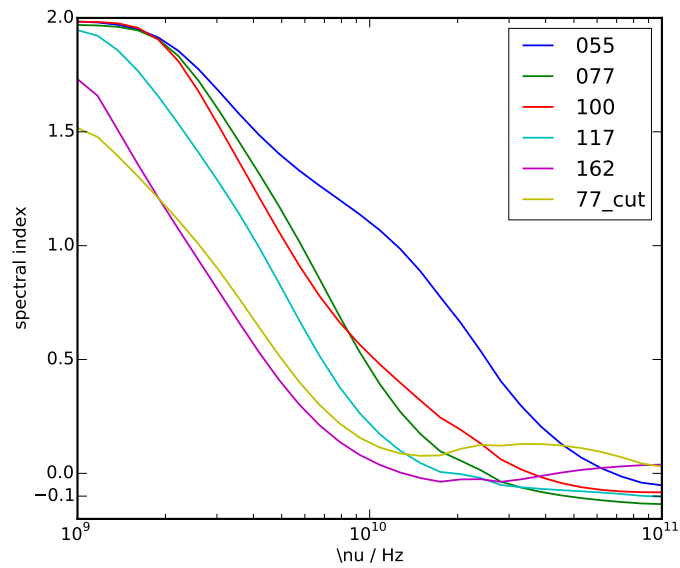


Figure 5.16: The spectral index for each of the models as a function of frequency, for an inclination angle of 45°

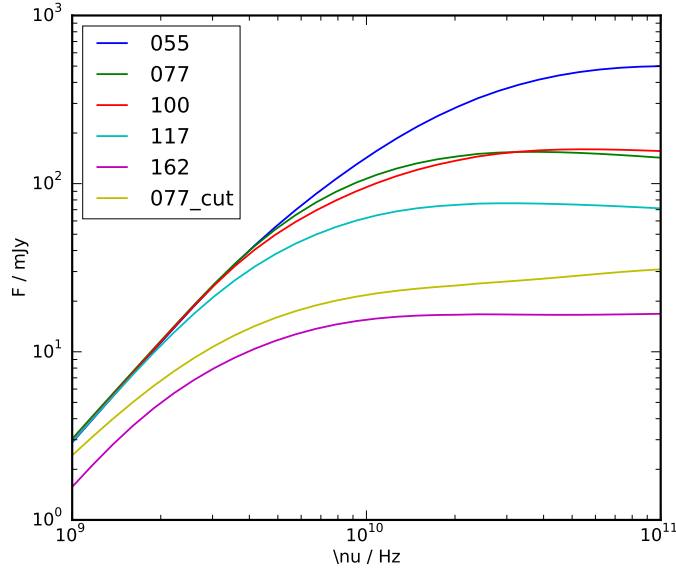


Figure 5.17: The free-free emission spectra for each of the models viewed with an inclination angle of 75°

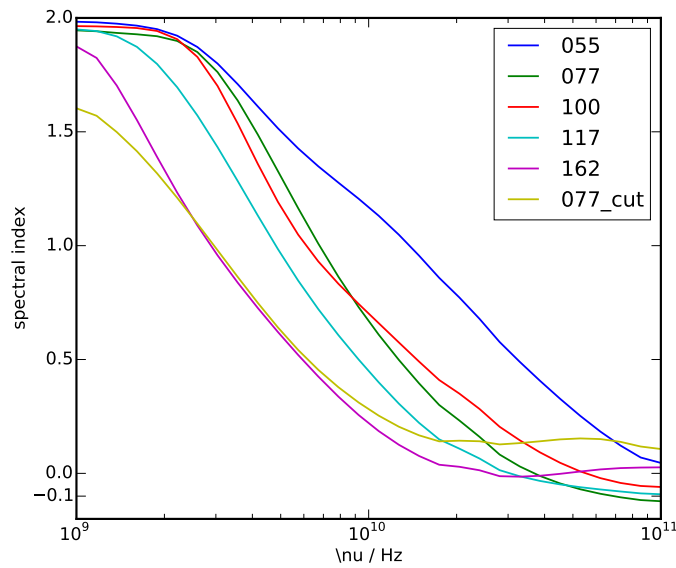


Figure 5.18: The spectral index for each of the models as a function of frequency, for an inclination angle of 75°

at 100GHz. The spectral index drops fastest for the models driving the least amount of mass from the disc. More optically thick discs have higher spectral indices in the region of $\sim 3\text{-}30\text{GHz}$. The exception to this is the R07.7_cut model which only has a spectral index of ~ 1.5 at 1.5GHz, falls to 0 between 10 and 20GHz, and then increases slightly between 20 and 100GHz (see figures 5.13, 5.15 and 5.17). This is due to the presence of the exponential cut off term in the disc density which significantly decreases the emissivity in the outer regions of the disc.

Spectral indices for most models are seen to transition from +2 to ~ -0.1 . These indexes are typical of optically thick / thin HII regions. By looking at the optical depths of the emission in a model we can see that these spectral indices do coincide with optically thick / thin emission across the entire disc (optical depths of the R10.0 model are shown in figure 5.19 for the same three inclinations and frequencies shown in the previous figures). The high optical depths at the lower frequencies extending out to the edge of the model indicates there would be emission coming from outside the simulated region. This means that for the lower frequencies the fluxes calculated are lower limits rather than predicted values, and this could lower the spectral index at these frequencies if this flux was included. The calculated indices are in contrast to the usual spherical indices seen from outflowing winds, which have a constant spectral index of +0.6 (Wright & Barlow 1975). This spectral index of 0.6 is derived using a spherical wind with constant temperature and a density profile proportional to r^{-2} . In the disc wind shown here the ionised density is not a simple function of radius. It depends on where the ionisation front penetrates into the disc and what the dynamics are at that point. In particular the edge of the ionised region in the

disc (where the maximum ionised density is and therefore the source of the bulk of the emission) does not vary significantly with radius (see figure 4.11). This in turn explains why the spectral index is more similar to a constant density HII region rather than a spherically symmetric expanding, constant velocity wind.

Gibb & Hoare (2007) fitted spectral indices to observations of 5 MYSOs (S106-IR, S140-IRS1, W75N-VLA3, NGC2024-IRS2 and LkH α 101) in the 5-45GHz range. The fitted spectral indices are between 0.5 and 0.8 in 4 of the 5 protostars observed (with the other having an index of 0.18). Although this appears inconsistent with the results presented here, the fits shown by Gibb are based on 3 or 4 data points, and are confined to a single spectral index over the whole of the frequency range. In addition there is some indication in the spectra they show of higher indices at their lower frequencies (5-10GHz) and lower or even negative indices at their highest frequencies which are uncontaminated by dust emission (20-45GHz).

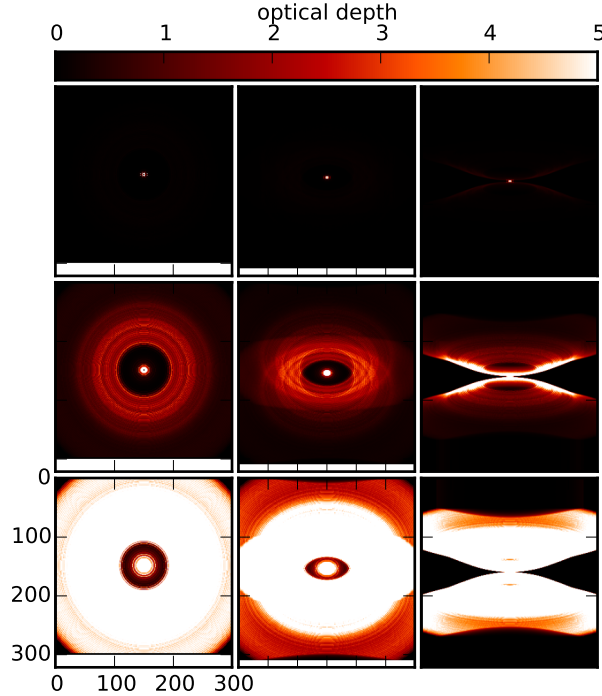


Figure 5.19: The optical depth of the R10.0 model for different inclination angles and frequencies. **top to bottom** : 23, 5.0 and 1.5GHz; **left to right**: 0° , 45° and 75° .

5.3.2 C^+ lines

Using LIME to solve the equations of statistical equilibrium and radiative transfer we are able to create a position-position-velocity cube for each of the possible C^+ lines for each model for a number of viewing angles. The C^+ lines at 659, 848 and 1507GHz are not significantly excited in these models, due to them having an upper energy level of 40,000K. The 1901GHz line however is and can be seen clearly in emission from each of the models except R145.0. As the R145.0 model has very little ionised gas, the C^+ abundance is low and lines are not visible in radiative transfer calculations of it. This wavelength regime ($\sim 150\mu m$) is not possible to observe from the ground (due to the opacity of the atmosphere) and

so space based instruments are needed. Herschel currently has provided the best resolution at this band at ~ 10 arcseconds, significantly less than the 0.3 needed to begin to resolve a 300au disc at a distance of 800pc.

Although this line is not observable with any currently operational or planned telescopes, it is an optically thin line tracing the ionised disc wind. This allows us to look at the line profiles for different models and compare them to other similar lines which could be tracing such an ionised disc wind. The figures below (figures 5.20 to 5.25) show the dust continuum, continuum subtracted line intensity, intensity weighted velocity and the unresolved line spectrum.

There is a general trend that the earlier models (i.e. the ones with protostars with larger radii) have wider wings than the later ones, but weaker emission. This is consistent with the findings of chapter 4 that the earlier models have higher emission weighted velocities in the disc but less ionising flux from the protostar and therefore lower ionised densities in the disc wind. Looking at the 15° models the full width at zero intensity (FWZI) increases from 175 km s^{-1} for the R05.5 model to 500 km s^{-1} for the R16.2 model. Interestingly the R07.7_cut model line profiles look much more like the ones from R16.2 than the ones from R07.7, demonstrating that any inferences of the state of the protostar from the properties of the disc wind are dependent upon the large scale structure of the disc which would need to be determined from separate measurements.

Lines calculated in these models are narrow compared to the Brackett12 line observed ($n=12-4$) by Lumsden *et al.* (2012) but comparable to the $n=41-40$, $n=43-42$ and $n=52-50$ lines observed by Guzmán *et al.* (2014). Lumsden *et al.* (2012) suggest that Stark broadening is an important factor in obtaining the line widths that they see. As this has not been included in these models it may provide

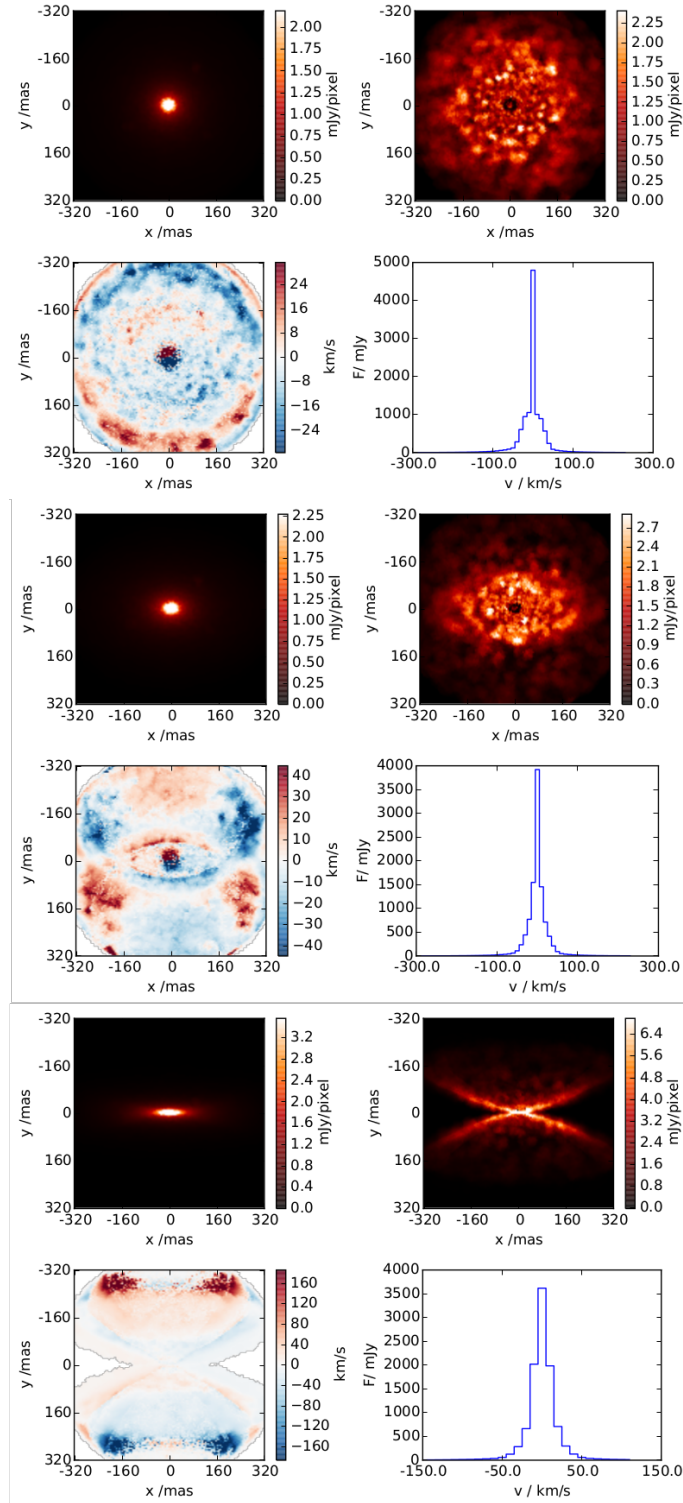


Figure 5.20: The R05.5 model viewed at an angle of 15, 45 and 75° (top, middle and bottom). **Upper left** the dust continuum of the model at 1900GHz. **Upper right** The integrated intensity of the [C⁺] line at 1900.5GHz. **Lower left** the intensity weighted velocity of the line. **Lower right** The total spectrum from the model.

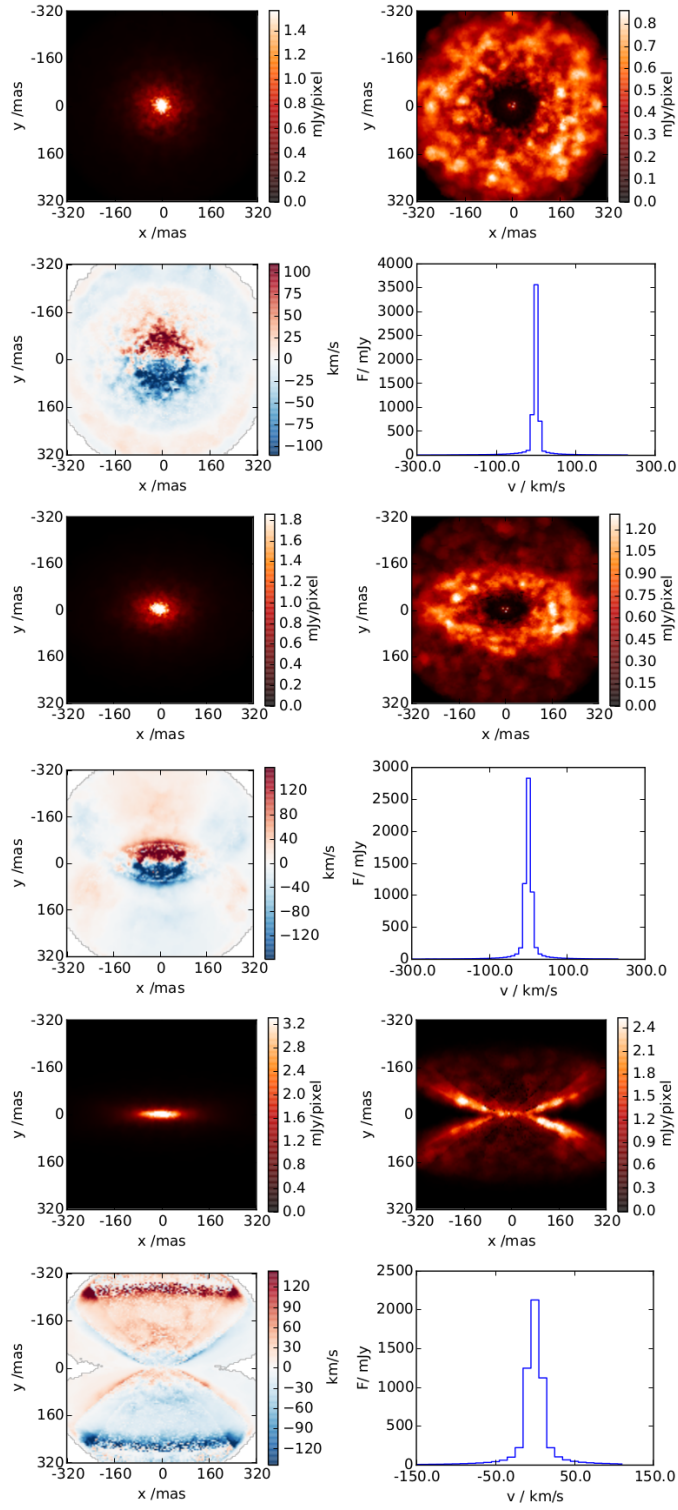


Figure 5.21: The R07.7 model viewed at an angle of 15, 45 and 75° (top, middle and bottom). **Upper left** the dust continuum of the model at 1900GHz. **Upper right** The integrated intensity of the $[C^+]$ line at 1900.5GHz. **Lower left** the intensity weighted velocity of the line. **Lower right** The total spectrum from the model.

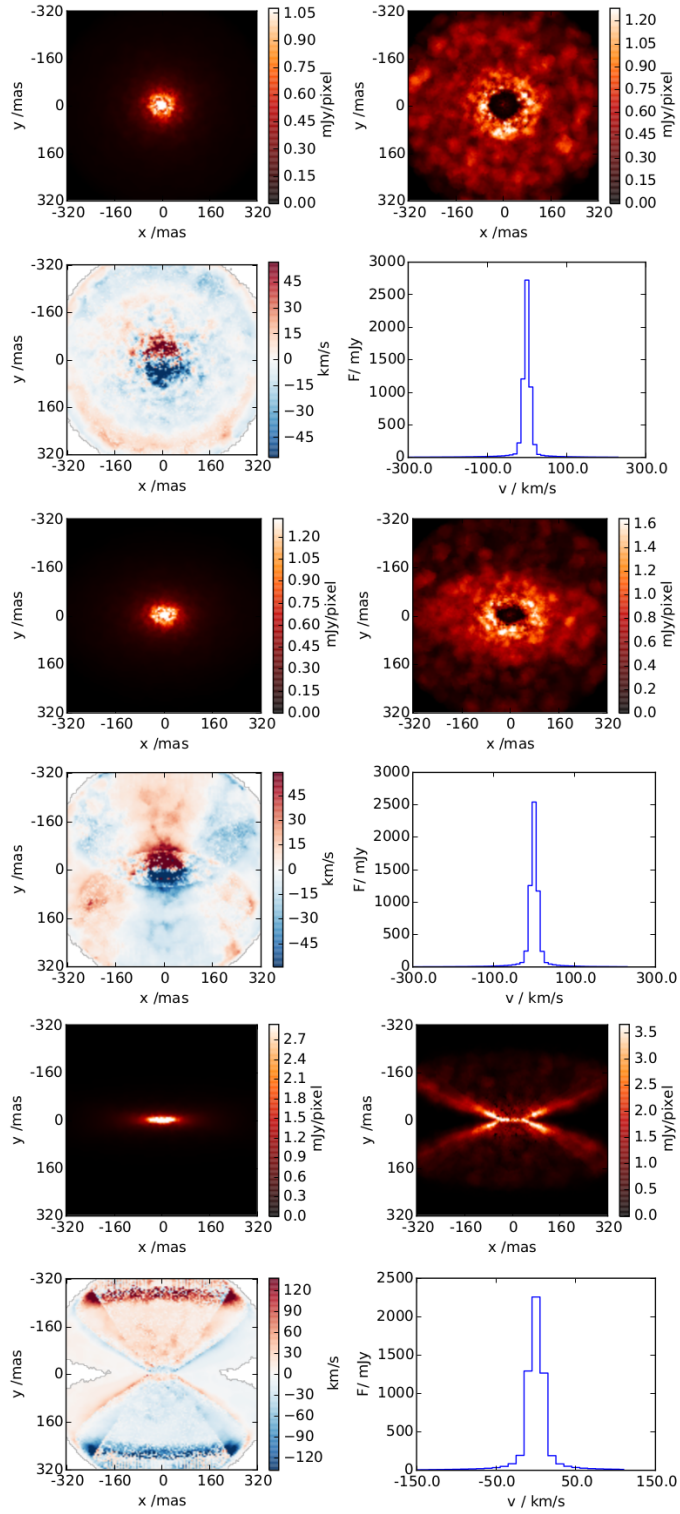


Figure 5.22: The R10.0 model viewed at an angle of 15 , 45 and 75° (top, middle and bottom). **Upper left** the dust continuum of the model at 1900GHz . **Upper right** The integrated intensity of the $[\text{C}^+]$ line at 1900.5GHz . **Lower left** the intensity weighted velocity of the line. **Lower right** The total spectrum from the model.

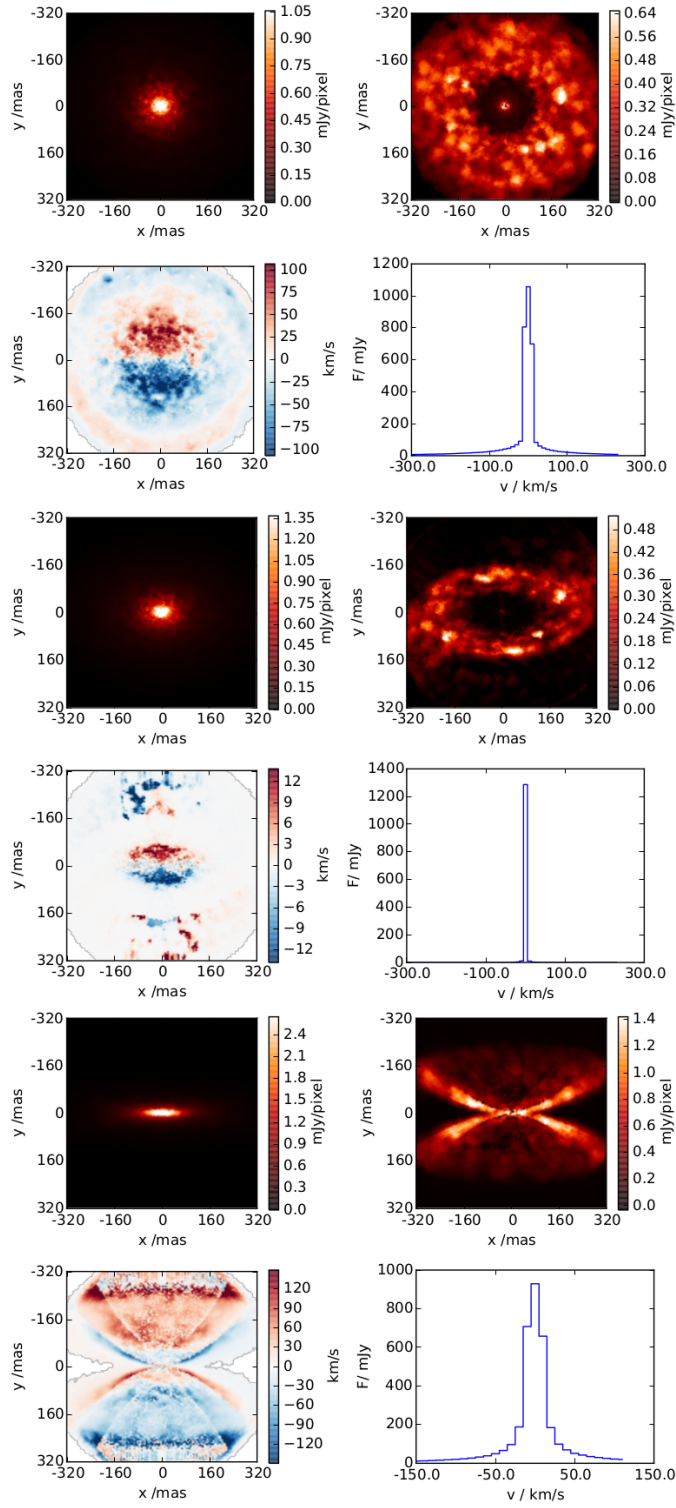


Figure 5.23: The R11.7 model viewed at an angle of 15, 45 and 75° (top, middle and bottom). **Upper left** the dust continuum of the model at 1900GHz. **Upper right** The integrated intensity of the $[C^+]$ line at 1900.5GHz. **Lower left** the intensity weighted velocity of the line. **Lower right** The total spectrum from the model.

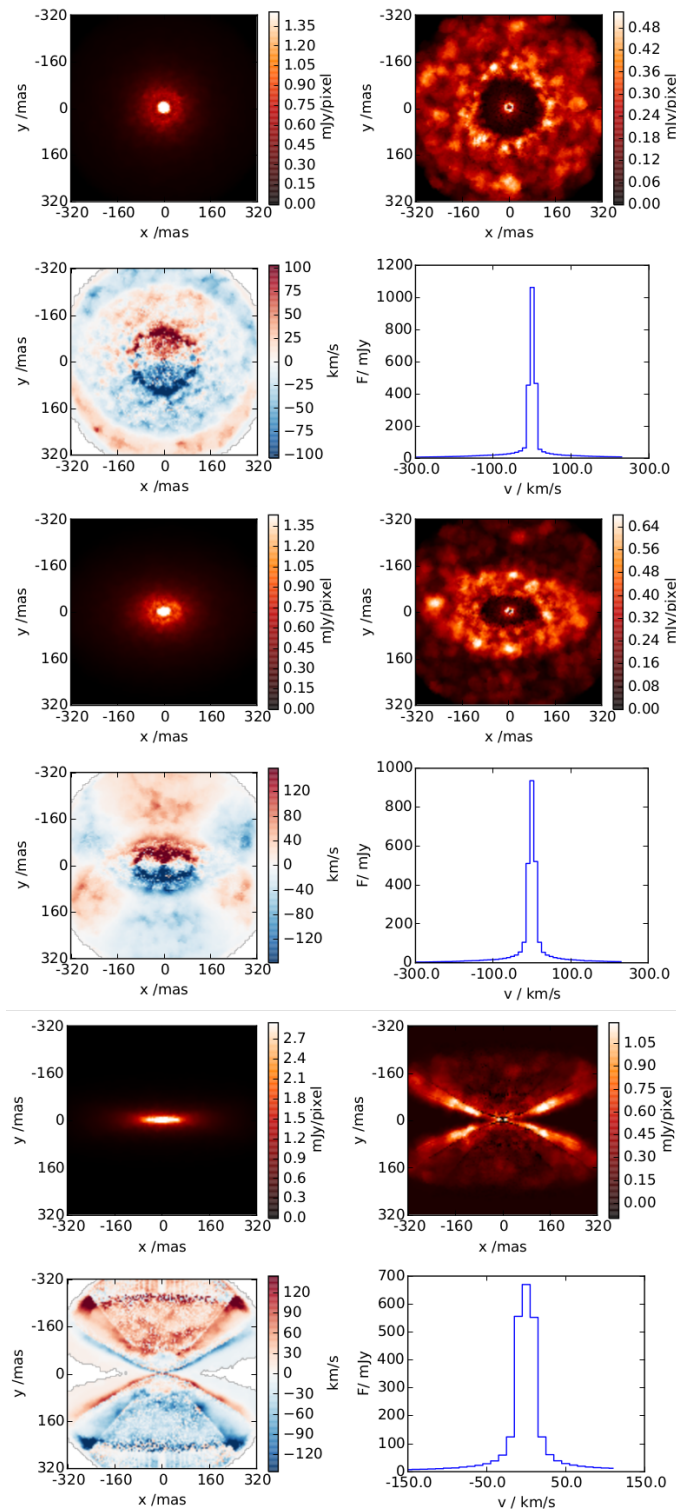


Figure 5.24: The R16.2 model viewed at an angle of 15, 45 and 75° (top, middle and bottom). **Upper left** the dust continuum of the model at 1900GHz. **Upper right** The integrated intensity of the [C⁺] line at 1900.5GHz. **Lower left** the intensity weighted velocity of the line. **Lower right** The total spectrum from the model.

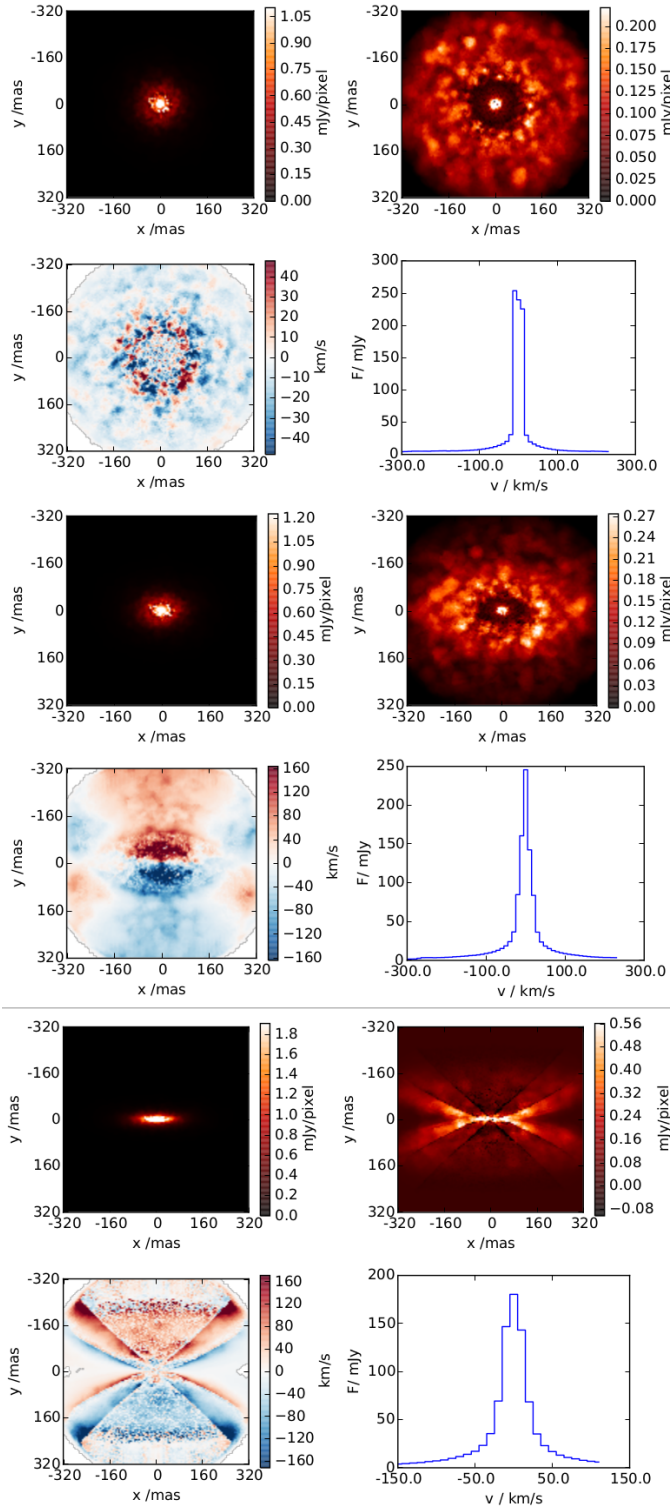


Figure 5.25: The R07.7cut model viewed at an angle of 15, 45 and 75° (top, middle and bottom). **Upper left** the dust continuum of the model at 1900GHz. **Upper right** The integrated intensity of the [C⁺] line at 1900.5GHz. **Lower left** the intensity weighted velocity of the line. **Lower right** The total spectrum from the model.

the reason why the observed lines are significantly wider than the predictions.

As noted in chapter 4 the rotational velocity is significantly smaller than the velocity in the plane of the simulation. This can be seen in the fact that even with channel widths of 10 km s^{-1} no double peaked spectra are seen in any of the models.

5.3.3 Hydrogen recombination lines

In order to create images of the hydrogen recombination lines the absorption and emission coefficients were calculated (as described in section 5.2.3) for each model at 20 frequencies corresponding to velocities of between -200 and $+200 \text{ km s}^{-1}$. These were then added to the free-free coefficients and the radiative transfer equation was solved along each column of the model. The resulting spectra are shown in figures 5.26 to 5.31. As with the Bremsstrahlung the R145.0 model did not produce significant emission and so is not included in these results.

The spectra all show extended wing emission, out to at least 200 km s^{-1} in each of the models, with some appearing to extend out further. All of the models except R05.5 show bright, flat topped regions in the spectra, suggesting the lines are very optically thick. This is born out by looking at the line opacities of the models which show saturated emission across the emitting region and large (>100) optical depths. The peak intensity of the line emission drops sharply with decreasing radius, with the peak of the emission from the R16.2 model more than a factor of 10 less than from the R05.5 model.

Inclination angle seems to have little effect on the shape of the profiles, but greater inclinations give decreased flux at all velocities. This can be understood

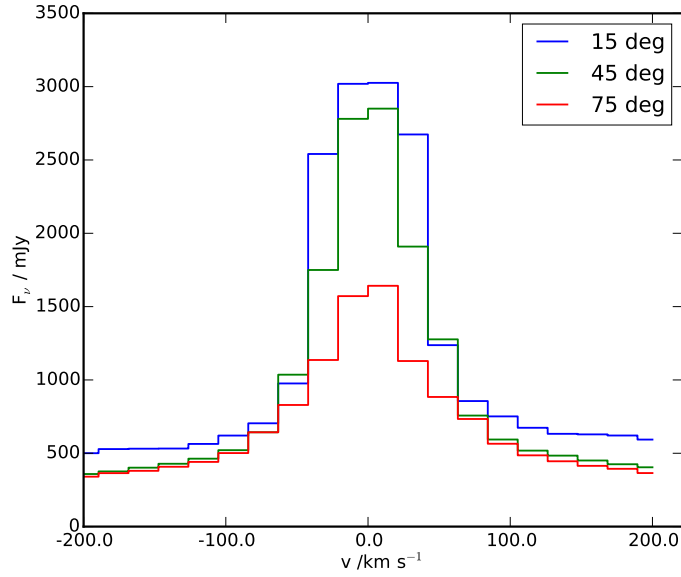


Figure 5.26: The spectra of the hydrogen 66-65 line for the R05.5 model for 3 different inclinations.

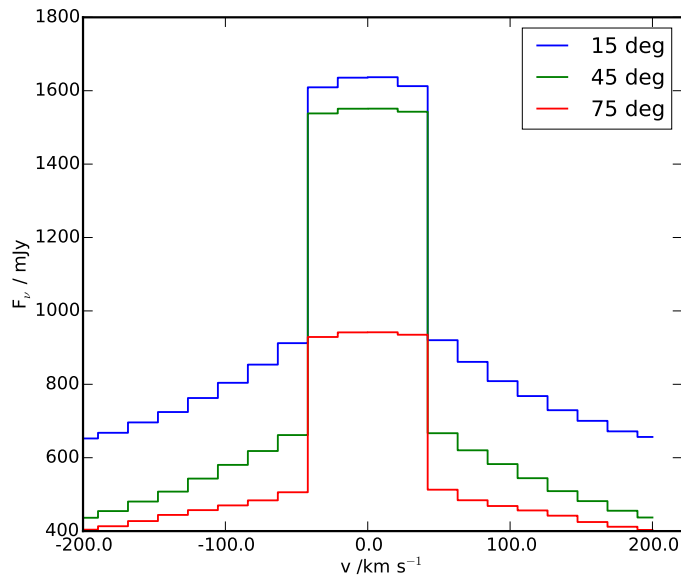


Figure 5.27: The spectra of the hydrogen 66-65 line for the R07.7 model for 3 different inclinations.

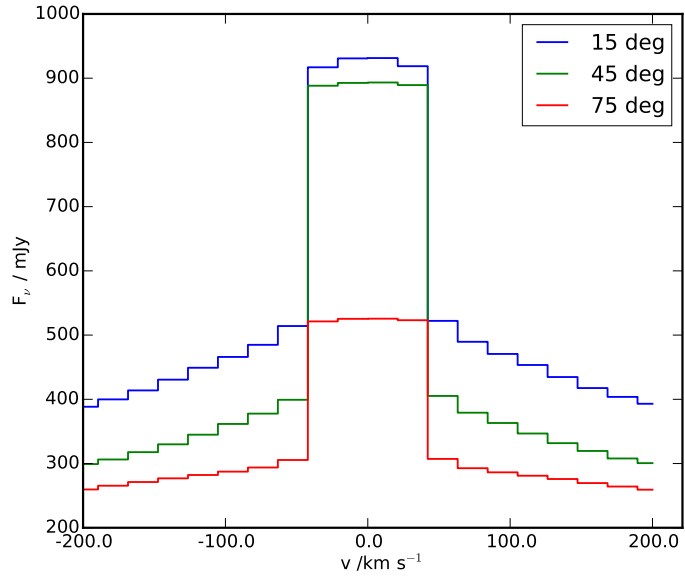


Figure 5.28: The spectra of the hydrogen 66-65 line for the R10.0 model for 3 different inclinations.

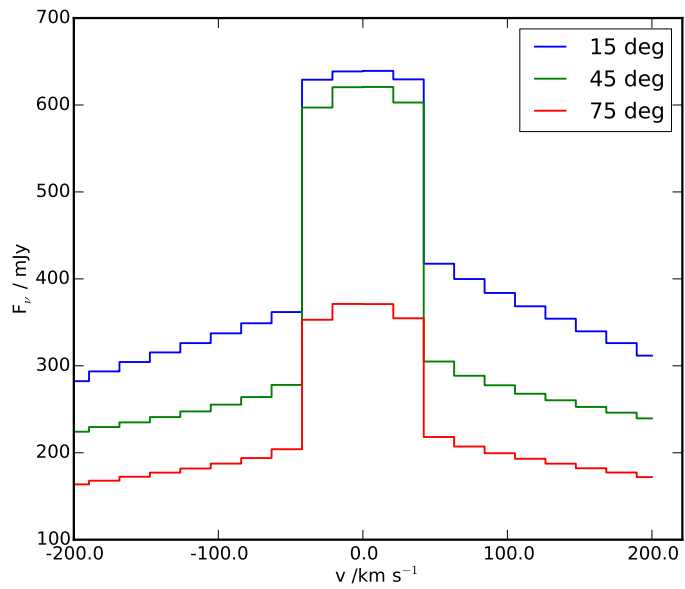


Figure 5.29: The spectra of the hydrogen 66-65 line for the R11.7 model for 3 different inclinations.

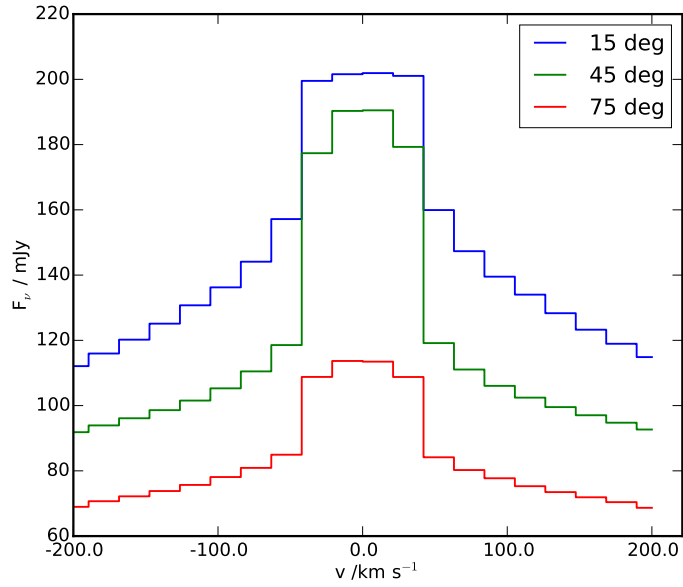


Figure 5.30: The spectra of the hydrogen 66-65 line for the R16.2 model for 3 different inclinations.

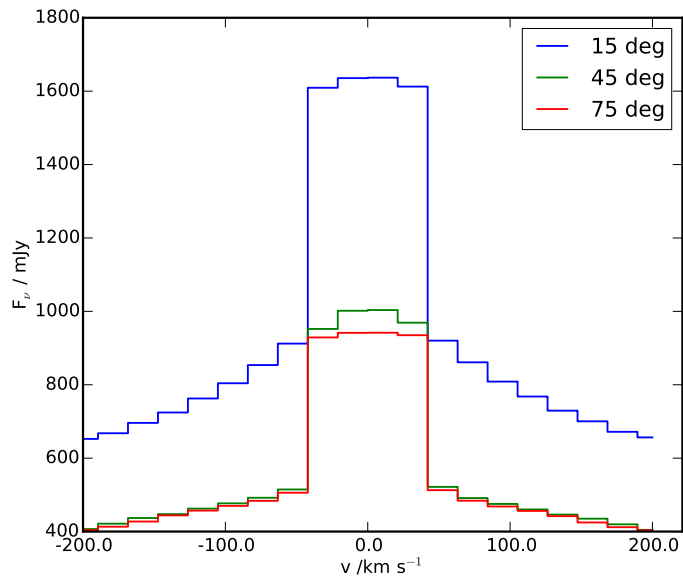


Figure 5.31: The spectra of the hydrogen 66-65 line for the R07.7cut model for 3 different inclinations.

if the lines are optically thick as at viewing angles closer to edge on less of the disc is visible. The single peaked nature of the lines in all the models is due to the low rotational to linear velocity ratio seen in the ionised disc wind (see section 4.4, figures 4.21 and 4.22).

5.4 e-Merlin simulated observations

In order to make predictions of the observability of the features for which synthetic brightness maps were constructed, the Common Astronomy Software Applications package (CASA) was used to simulate observations with the Merlin, an interferometer consisting of 7 radio telescopes across the United Kingdom. The longest baseline in Merlin is 217km and the beam sizes in the frequencies used range between 0.15 and 0.01 arcseconds. This angular resolution is sufficient to resolve the 300au disc at a distance of 800pc. There are three frequency bands available with e-Merlin, 1.3-1.8 GHz, 4-8 GHz and 22-24 GHz. Presented here are synthetic observations of the radiative transfer calculations presented in section 5.3.1 at 1.5, 5 and 23 GHz. The observations were simulated with a 16h track. The resulting measurement set was then CLEANed interactively in order to minimise the effect of side-lobes. The cleaning here has not been optimised however, and it is probable that careful cleaning could produce better images.

In the 1.5GHz band at an inclination angle of 0° (figure 5.32) no structure is seen in any of the models. The input skymodel is of nearly constant brightness and the synthetic observations accurately reproduce this (for the section of sky simulated) In order to see structure in images at this frequency it would be necessary to extend the models out to greater radii. However, given that the

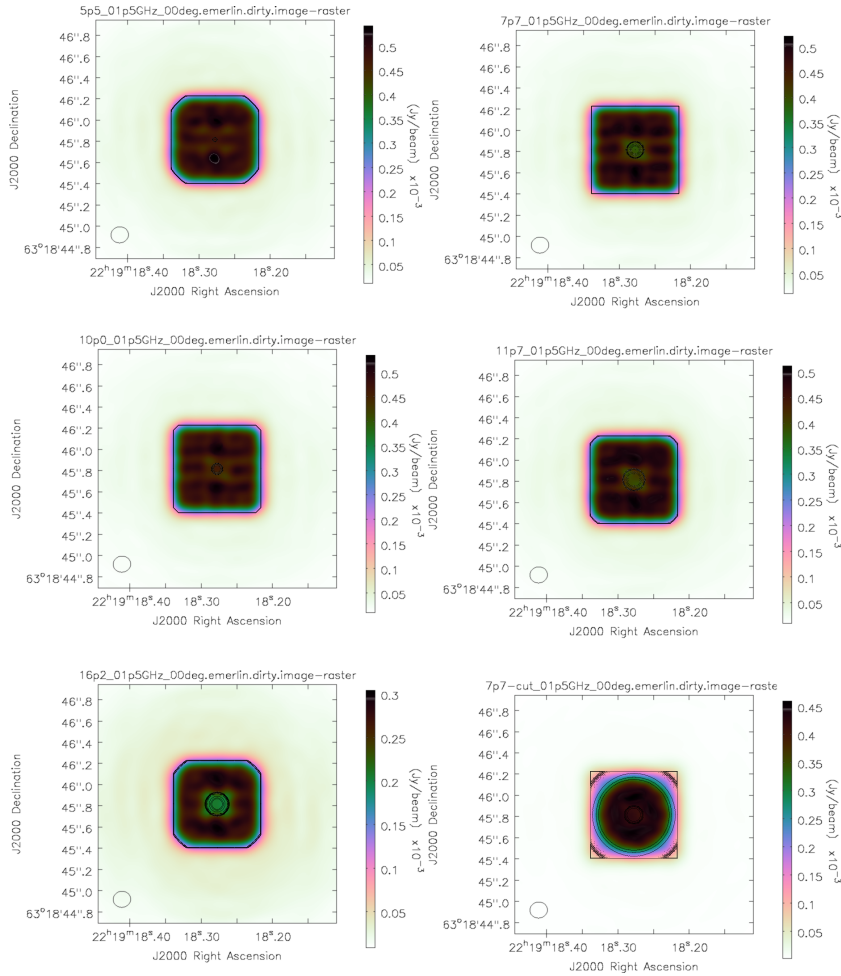


Figure 5.32: Synthetic observations of the models with e-Merlin at 1.5GHz viewed at an inclination angle of 0° . The contours show the radiative transfer model used as a skymodel and are scaled to the peak of the brightness.

optical depth is still greater than 5 at the outer edge of the current model (see figure 5.19) and that the maximum ionised density in the models only drops slowly with radius, it is likely that the model would need to be extended significantly in order to reach optically thin regions at this wavelength.

In the 5GHz band at 0° (figure 5.33) some structure is visible and it is clear that not all the models have the same spatial extent in their emission. For the

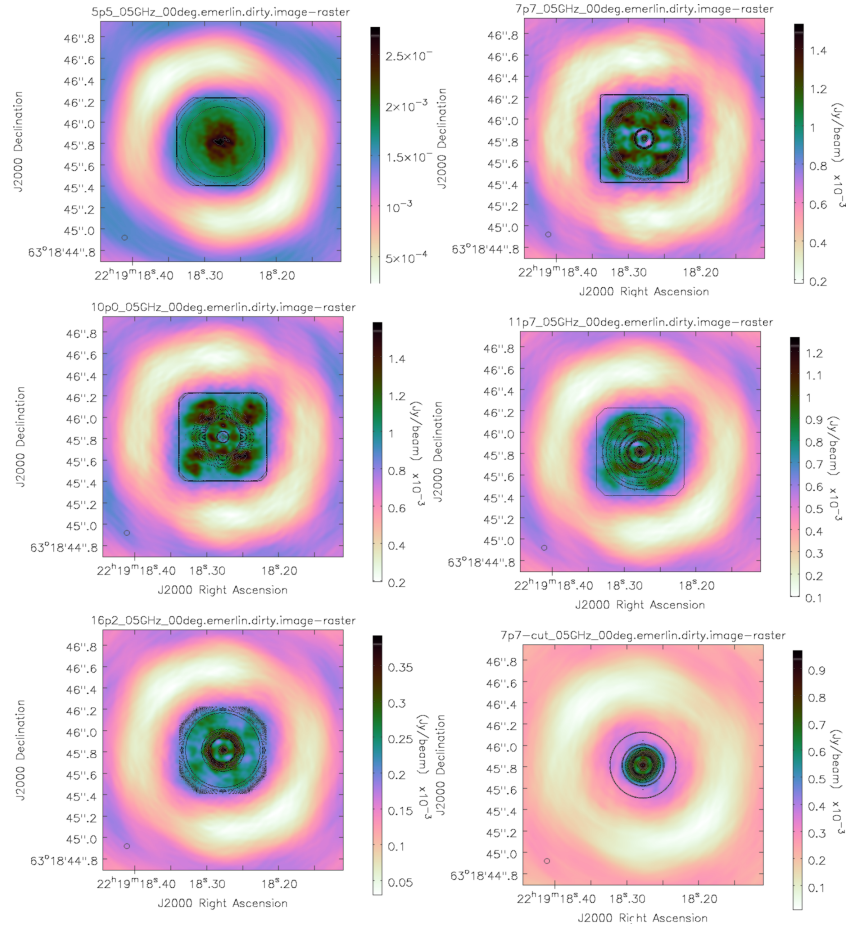


Figure 5.33: Synthetic observations of the models with e-Merlin at 5GHz viewed at an inclination angle of 0° . The contours show the radiative transfer model used as a skymodel and are scaled to the peak of the brightness.

models with lower mass fluxes (most notably in the R07.7_cut model but also in R16.2) the outer regions of the disc become optically thin and the brightness of the disc in those regions decreases.

At 23 GHz the face on models appear to be over-resolved, with a strong central source dominating the emission in the R10.0, R11.7 R16.2 and R07.7_cut models (figure 5.34).

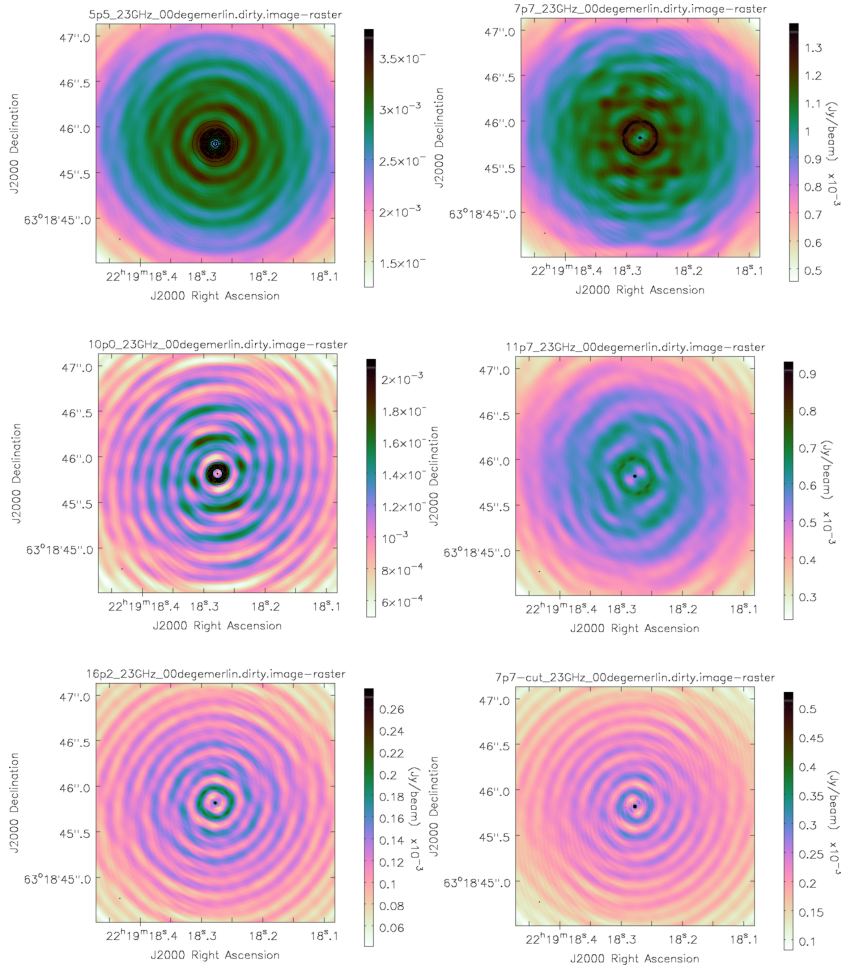


Figure 5.34: Synthetic observations of the models with e-Merlin at 23GHz viewed at an inclination angle of 0° . The contours show the radiative transfer model used as a skymodel and are scaled to the peak of the brightness.

At 45° small amounts of structure become visible in the 1.5GHz window (figure 5.35), but most of the models remain optically thick and at constant brightness across the simulated region. The R16.2 and R07.7_cut models in particular show some elongation in the plane of the disc.

In the 5GHz observations at 45° (figure 5.36), elongation of the emission has become pronounced in all but the R5.5 model (which has the highest mass

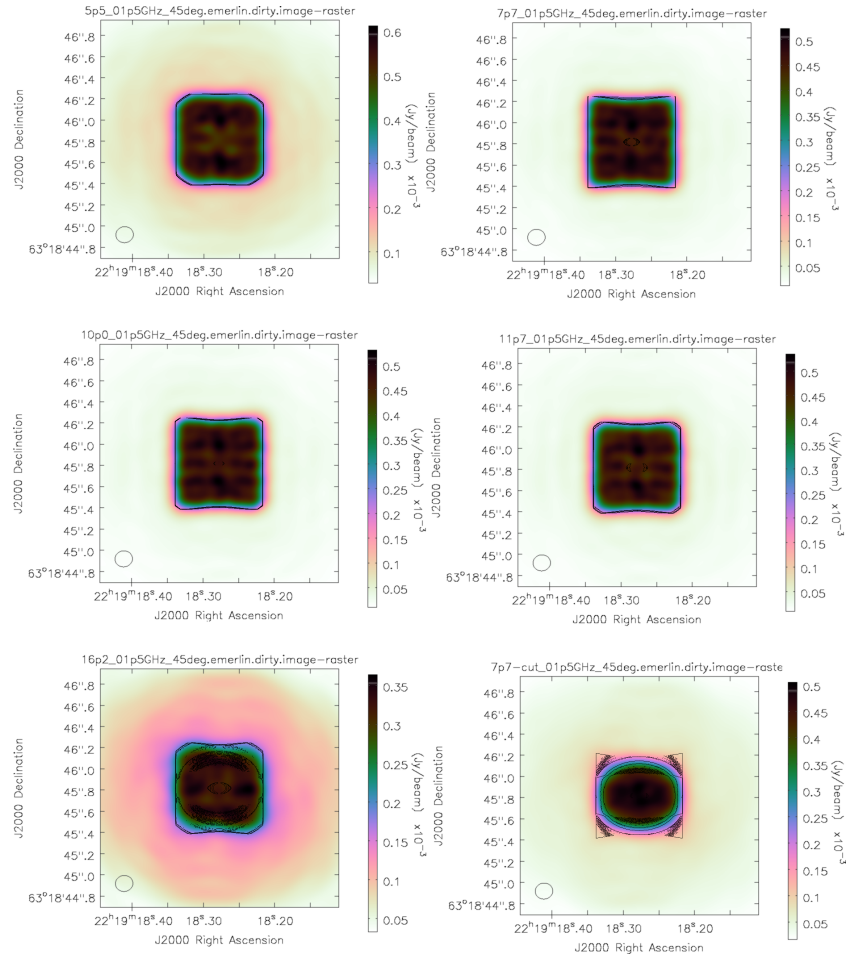


Figure 5.35: Synthetic observations of the models with e-Merlin at 1.5GHz viewed at an inclination angle of 45° . The contours show the radiative transfer model used as a skymodel and are scaled to the peak of the brightness.

flux and is the most optically thick). These maps look superficially similar to the 5GHz emission seen in IRS1-S140 (Hoare 2006, see figure 1.8) however the models are brighter than this source by a factor of between 3 and 20, depending on the model. However the simulated images clearly show that a disc wind at an intermediate angle can produce an elongated structure in free-free emission at 5GHz.

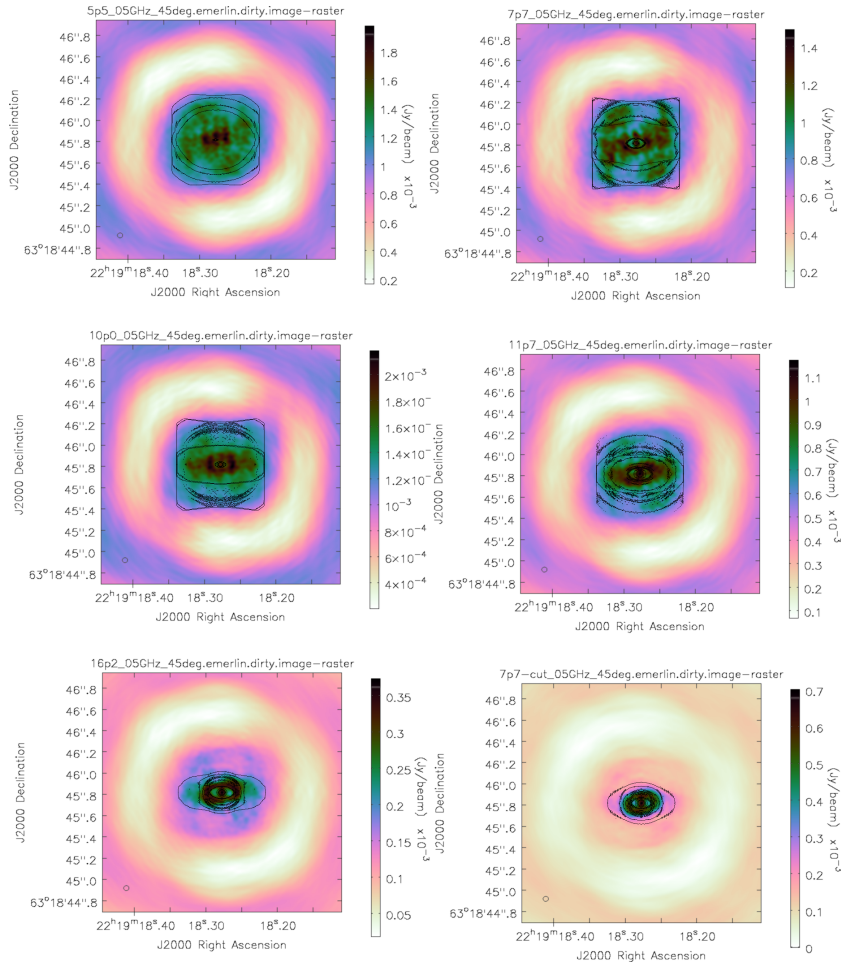


Figure 5.36: Synthetic observations of the models with e-Merlin at 5GHz viewed at an inclination angle of 45° . The contours show the radiative transfer model used as a skymodel and are scaled to the peak of the brightness.

As with the 23GHz images at 0° , the 45° images appear to be over-resolved (figure 5.37). The only images which show more than a point source at the centre are the R05.5 and R07.7 models which show an elongated structure in the first and a ring of emission in the second. However interpreting the structure of these without the modelled emission overlaid would be very unconvincing. At best all that could be gathered from observations such as these would be a

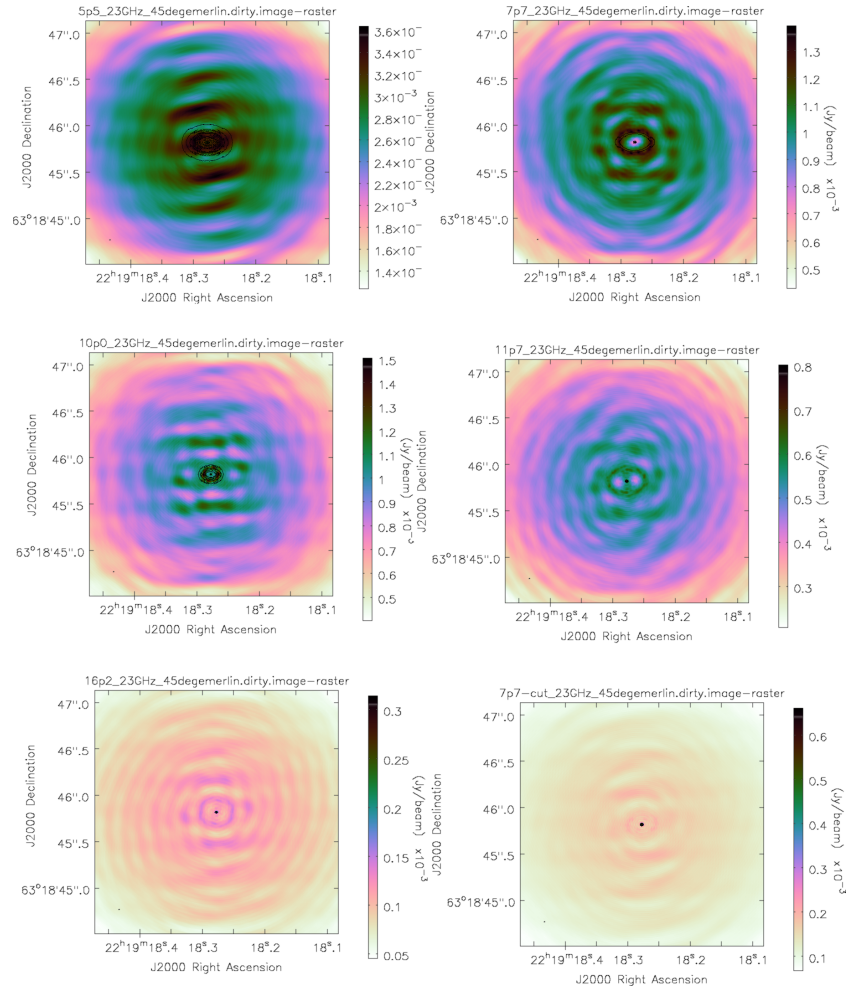


Figure 5.37: Synthetic observations of the models with e-Merlin at 23GHz viewed at an inclination angle of 45° . The contours show the radiative transfer model used as a skymodel and are scaled to the peak of the brightness.

flux measurement and possibly an indication of which direction the emission was elongated in.

Figure 5.38 shows the 1.5GHz emission at an inclination angle of 75° , the hour glass shape structure can be seen clearly on all the models. The exception to this is the emission of the R07.7_cut model, which is the most compact, however this still shows elongation in the direction of the disc. Any of the observations

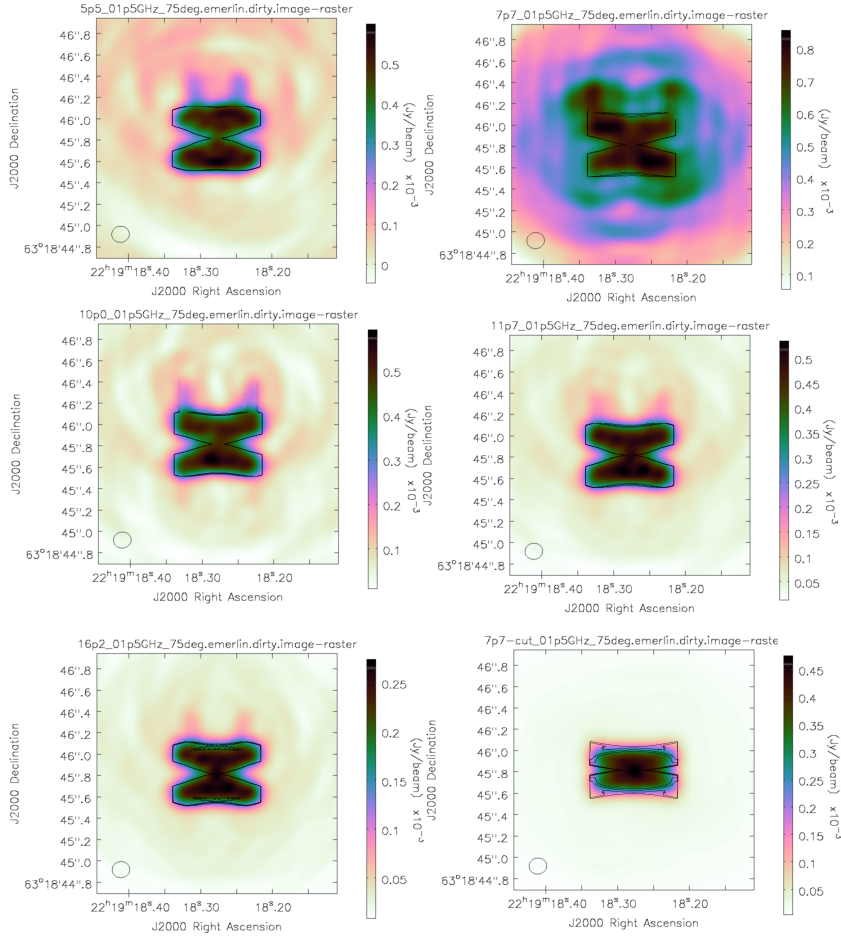


Figure 5.38: Synthetic observations of the models with e-Merlin at 1.5GHz viewed at an inclination angle of 75° . The contours show the radiative transfer model used as a skymodel and are scaled to the peak of the brightness.

generated from the other 5 models would be clear indications of an ionised wind being blown from the surface of a circumstellar disc.

At 5GHz (figure 5.39) the ionisation surface of the disc becomes visible, giving the emission a distinctive ‘x’ shape for all the models. Even the R07.7-cut model now shows differentiation between the top and bottom halves of the disc. Observations such as these show the structure of the ionised disc wind clearly, but also reveal the presence of the neutral matter which must exist between the

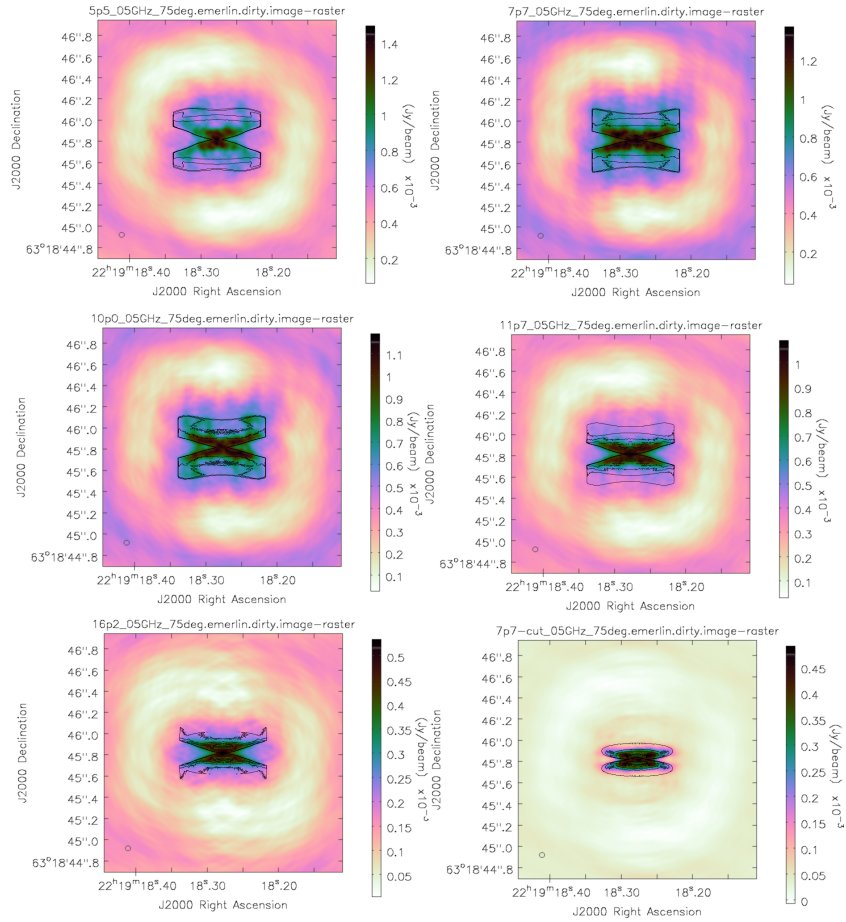


Figure 5.39: Synthetic observations of the models with e-Merlin at 5GHz viewed at an inclination angle of 75° . The contours show the radiative transfer model used as a skymodel and are scaled to the peak of the brightness.

two halves of the disc. In this way the radial dependence of the disc scale height could be recovered and from this inferences on the method of heating the disc drawn (i.e. whether it is primarily viscously heated or by stellar illumination).

The 23GHz image at 75° (figure 5.40) is the only one at that frequency to show clearly resolved structure. Again the two high density surfaces at the base of the ionised region of the disc wind are visible as an x shape in all the images to some extent, though the detection is faint in the R07.7_cut model.

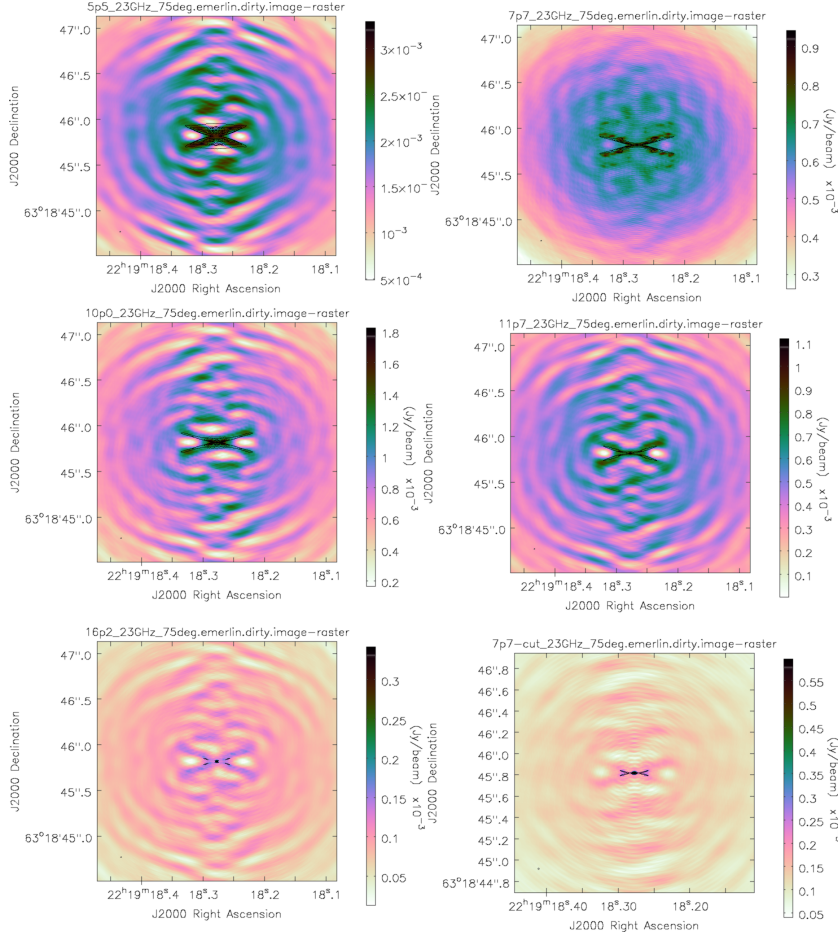


Figure 5.40: Synthetic observations of the models with e-Merlin at 23GHz viewed at an inclination angle of 75° . The contours show the radiative transfer model used as a skymodel and are scaled to the peak of the brightness.

5.5 Conclusions

In this Chapter I have explored different possible emission mechanisms from an MYSO blowing a wind from a surrounding accretion disc and investigated how they would look when observed from Earth at a distance of 800pc. The disc-wind model presented in chapter 4 was used as an input to the model providing densities, temperatures and ionisation fractions. We find that the disc wind de-

scribed by the hydrodynamic model could be observed with current instruments. The combination of detailed, spatially resolved free free emission possible with e-Merlin at 5GHz and 23GHz and kinematic information from hydrogen recombination lines or emission lines from ionised species in the disc wind allows a detailed picture of the disc wind to be reconstructed.

There are similarities between the emission predicted by these simulations and observations of the radio continuum observed towards the MYSO S140 IRS1 performed by Hoare (2006) and the hydrogen recombination lines observed by Lumsden *et al.* (2012).

In particular the 5GHz synthetic e-Merlin images of the disc models at 45° inclination (figure 5.36) show a strong resemblance to the observations of Hoare (2006) (see figure 1.8) showing both a similar morphology and a peak brightness of ~ 1 mJy/beam.

The line emission from both the [C⁺] and hydrogen recombination lines also show similar profiles to observations of MYSOs. The intensities of these lines vary significantly with the R05.5 lines showing peak brightnesses of nearly 3.5Jy and the R16.2 model showing similar line profiles but intensities of only ~ 200 mJy. For H lines, the assumptions made of LTE and that all recombinations to the electronic state n have a chance to transition to $n-1$ before being re-ionised are severe. Future work would include a fully self consistent calculation of ionisation, recombination and line emission using an existing code designed for this purpose.

However if these intensities are borne out by more self consistent calculations it would suggest that a combination of bremsstrahlung, and hydrogen recombination

line emission at 23GHz would provide an indicator of the evolutionary state of the central MYSO. As the protostar contracts down from its inflated state due to a high accretion rate towards a more main sequence like state, both the free free emission and hydrogen recombination line emission will increase significantly. These are both clearly observable quantities with the current generation of radio telescopes.

Chapter 6

Conclusions

6.1 Summary of conclusions

This thesis contains simulations of the dynamics of discs around protostellar objects and radiative transfer calculations of such models in order to determine their observable properties. The following sections restate the conclusions of each chapter. In section 6.2 we consider ideas for future work and final remarks are offered in section 6.3.

6.1.1 Simulated observations of gravitationally unstable young protoplanetary discs

In this chapter I presented radiative transfer simulations of a hybrid model comprising a $0.39 M_{\odot}$ self gravitating disc with a radius of 64 au and spiral density waves, surrounded by an envelope that is a contracting $10 M_{\odot}$ BE-sphere. The main results of these simulations are as follows:

- CASA simulations of this model show that at a distance of 100 pc, extraction

of kinematic and structural information from the continuum and molecular lines is possible with ALMA band 7.

- Our simulations show that molecular features are predominantly seen in absorption against the hot mid-plane of self-gravitating protoplanetary discs, with emission only being seen where voids in the structure of the disc do not provide a bright continuum source to be absorbed.
- The quiescent nature of the envelope around such discs only affects lines within $\pm 0.5 \text{ km s}^{-1}$ of the LSR velocity.
- The lines studied (OCS 26 \rightarrow 25, H₂CO 4₀₄ \rightarrow 3₀₃, C¹⁷O 3 \rightarrow 2 and HCO⁺ 3 \rightarrow 2) taken together allow all regions of the disc to be sampled and the rotation of the disc to be constrained from the inner edge to the outer edge.
- Spiral structures in young embedded discs are detectable at a wide range of inclination angles. They can be resolved spatially at angles close to face on and can be inferred from position velocity diagrams at low inclination angles.
- The dust continuum emission at millimetre wavelengths is optically thick and millimetre observations lead to significant underestimates of the disc mass, by a factor of 4 or more.

One assumption underpinning this model is that the gas and dust are in thermal equilibrium in the disc. If they are not and the dust is significantly cooler than the gas then transitions may not show up in absorption. However, the large volume densities are expected to provide efficient dust-gas coupling. Outflows could contaminate line profiles of those species which commonly trace outflows, such as CO and HCO⁺. In these cases, a detailed study of their line profiles using high spectral resolution should help to disentangle the various kinematic components.

These results demonstrate that ALMA will be able to probe the very earliest stages of circumstellar discs which feed the growing protostar, and which eventually will evolve into a planetary system. My results show that ALMA observations in band 7 will allow the assessment of whether or not these young discs are gravitationally unstable and test theories of pre-stellar to protostellar core evolution. If such gravitational instabilities exist, they will have significant implications for the evolution of the disc. For example, they will affect fragmentation, planetesimal formation (Boley 2009; Johnson & Li 2013; Gibbons *et al.* 2012) and the chemical evolution in the disc (I2011).

6.1.2 Hydrodynamic simulations of line mediated radiatively driven disc winds

In chapter four I presented work on a series of hydrodynamic models of Keplerian, hydrostatic accretion discs around MYSOs representative of a $10M_{\odot}$ protostar contracting towards the main sequence. In these models the effect of radiation pressure is simulated using local velocity gradients along lines of sight from 225 discrete point sources in the disc and a finite size source for the protostar. The resulting density and velocity distribution after $2 \times 10^8 s$ (~ 10 crossing times of the fast component of the wind) were analysed in order to calculate the ionised regions and to calculate mass fluxes which could be attributed to either a slow, dense disc wind or a fast rarefied polar wind. The main conclusions are:

- $10M_{\odot}$ protostars can drive at least some disc wind for all disc configurations tested. Mass loss rates for the models are ~ 50 times higher than those seen in Proga *et al.* (1998), partially due to the assumed higher accretion rates and

luminosities and partially due to the larger simulated area allowing mass loading from further out in the disc.

- Models with smaller protostellar radii drive stronger mass fluxes from their discs. This is attributed to the effect of increased accretion and reflected starlight luminosity coming from the discs around smaller stars.

- Mass fluxes from all the models except R145.0 are $\sim 10^2$ higher than would be the case for a spherical wind from these protostars, showing that the presence of a disc can significantly boost the mass loss rate of a young massive protostar.

- Disc mass loss happens mostly from the inner regions of the disc as shown by the modest reduction in the mass loss rate of the R7.7_cut model despite the significant reduction of its density in the outer regions.

- In the case of bloated protostars (as predicted by Hosokawa & Omukai 2009), disc winds are not driven in their most expansive stage and will not start until the star has contracted and increased its surface temperature.

6.1.3 Radiative transfer and synthetic observations of disc wind simulations

In this Chapter I have explored different possible emission mechanisms from an MYSO blowing a wind from a surrounding accretion disc and investigated how they would look when observed from Earth at a distance of 800pc. The disc-wind model presented in chapter 4 was used as an input to the model providing densities, temperatures and ionisation fractions. We find that the disc wind described by the hydrodynamic model could be observed with current instruments. The combination of detailed, spatially resolved free free emission possible with

e-Merlin at 5GHz and 23GHz and kinematic information from hydrogen recombination lines or emission lines from ionised species in the disc wind allows a detailed picture of the disc wind to be reconstructed.

There are similarities between the emission predicted by these simulations and observations of the radio continuum observed towards the MYSO S140 IRS1 performed by Hoare (2006) and the hydrogen recombination lines observed by Lumsden *et al.* (2012).

In particular the 5GHz synthetic e-Merlin images of the disc models at 45° inclination (figure 5.36) show a strong resemblance to the observations of Hoare (2006) (see figure 1.8) showing both a similar morphology and a peak brightness of ~ 1 mJy/beam.

The line emission from both the $[C^+]$ and hydrogen recombination lines also show similar profiles to observations of MYSOs. The intensities of these lines vary significantly with the R05.5 lines showing peak brightnesses of nearly 3.5Jy and the R16.2 model showing similar line profiles but intensities of only ~ 200 mJy. For H lines, the assumptions made of LTE and that all recombinations to the electronic state n have a chance to transition to $n-1$ before being re-ionised are severe. Future work would include a fully self consistent calculation of ionisation, recombination and line emission using an existing code designed for this purpose.

However if these intensities are borne out by more self consistent calculations it would suggest that a combination of bremsstrahlung, and hydrogen recombination line emission at 23GHz would provide an indicator of the evolutionary state of the central MYSO. As the protostar contracts down from its inflated state due

to a high accretion rate towards a more main sequence like state, both the free free emission and hydrogen recombination line emission will increase significantly. These are both clearly observable quantities with the current generation of radio telescopes.

6.2 Future work

Despite the state of the art simulations and observations that have been performed recently, unexplored areas of research still exist in the field of circumstellar discs and young stellar objects. This section outlines future work which could be carried out in order to further the work presented in this thesis.

6.2.1 Simulated observations of gravitationally unstable young protoplanetary discs

Observations of discs with cleared rings and spiral structure are just now beginning to become feasible at (sub)millimetre wavelengths thanks to ALMA. Recent observations of HL Tau (ALMA Partnership *et al.* 2015) show a resolved disc of ~ 100 au in radius with clearly visible lanes in the dust emission. Although this has been attributed to planet formation rather than gravitational instability, it shows ALMA's capability to provide detailed observations to test models with.

In order to further the understanding of gravitationally unstable discs it will be important to determine what observational properties will be constant across all discs of this nature and which vary from disc to disc. The current work of Evans *et al.* (2015) in replicating the physical and chemical model of a gravitationally

unstable disc for a proto-solar star will provide useful information in this regard, and the calculation of synthetic observations based on the method described in chapter 3 are planned.

In order to be able to observe gravitational instabilities in circumstellar discs high resolution ($\lesssim 0.075\text{arcsec}$) observations are needed at frequencies where the natal core is optically thin. This leaves ALMA as the only instrument capable of making these observations. With the 15km baselines now available, new observations will be able to be taken of nearby circumstellar discs in star forming regions and compared against theoretical predictions.

6.2.2 Hydrodynamic simulations and radiative transfer calculations of line mediated radiatively driven disc winds

The hydrodynamic simulations of the disc wind could be improved in two main ways. Firstly the scope of the simulation could be increased and secondly the detail of the microphysics could be improved.

To improve the scale of the model one possible option is to move from a 2D axis-symmetric model to a full 3D one. A three dimensional model would remove the simplifying assumptions of axis-symmetry of the hydrodynamic variables and would allow angular momentum to be evolved with the hydrodynamics rather than treated as a scalar quantity coupled to the gas. The dropping of these assumptions would allow investigation into the stability of the wind in the azimuthal direction. A first step in this direction would be to perform shearing box calculations of the disc wind (and thus avoid the wind launching region, and the

increased staircasing effect that would result from the decrease in resolution in 3D) to see whether, and under what conditions, azimuthal perturbations could be amplified.

The other possibility for increasing the scope of the model would be to increase the outer edge of the model past 300au. In doing this the initial condition of a constant α disc would become less appropriate at large radii. More realistic initial conditions could be obtained by using the results from a cloud collapse simulation (e.g. Kuiper *et al.* 2011) after the central object has accreted $10M_{\odot}$ of gas. Such larger scale simulations would provide insight into how the mass flux and velocity change when they come into contact with the parent core. They would also give a larger physical model from which to calculate emission from. This would be particularly useful for the low frequency free-free emission which was entirely optically thick in the model presented in this thesis (see chapter 5).

With regards to the microphysics of the model there are three areas which could be improved: calculating the ionisation state of the gas at runtime, calculating the radiation field self-consistently and determining accurate temperatures. The temperatures used in the model presented here use simple isothermal or adiabatic equations of state. In order to get more accurate temperatures heating and cooling terms would need to be calculated and thermal equilibrium maintained between the gas and the radiation field. In order to calculate these rates both the ionisation state of the gas and the radiation intensity as a function of frequency need to be known at each hydro cell at each time step.

These are all linked in that they require knowledge of the radiation field in each cell in order to calculate the quantities accurately. This requires some method

of calculating the radiation field as it is shaped by the gas (and in particular the dust) every hydrodynamical time step. The radiation-hydrodynamics code Torus (Harries 2015) uses a monte carlo treatment of the radiation in order to calculate radiation pressure on the dust, the ionisation state of the gas and to calculate thermal equilibrium. Adapting this to include line driving terms would result in a model with self consistent temperatures, ionisation structure, radiation field and radiation pressures. These more accurate temperatures and ionisation structures would also allow post-processing radiative transfer of the model to give more accurate results.

6.3 Final remarks

The study of circumstellar discs can provide useful insight into the process of star formation and the physical conditions in which this process takes place. Soon ALMA, when fully completed and operational, will drastically improve our understanding of star formation with detailed (sub)millimetre observations. In order to understand the physical processes which give rise to these observations the study of matter, light and their interactions is crucial.

This thesis has shown that hydrodynamic modelling and post processing with radiative transfer can provide detailed theoretical which can be compared against observation, to determine the physical conditions at the heart of the star formation process.

References

- ABBOTT, D.C. (1982). The theory of radiatively driven stellar winds. II - The line acceleration. *ApJ*, **259**, 282–301. 19, 45, 86
- ABBOTT, D.C. & LUCY, L.B. (1985). Multiline transfer and the dynamics of stellar winds. *ApJ*, **288**, 679–693. 106
- ABBOTT, D.C., BIEGING, J.H., CHURCHWELL, E. & CASSINELLI, J.P. (1980). VLA radio continuum measurements of mass loss from early-type stars. *ApJ*, **238**, 196–202. 114
- ABBOTT, D.C., BIEGING, J.H. & CHURCHWELL, E. (1981). Mass loss from very luminous OB stars and the Cygnus superbubble. *ApJ*, **250**, 645–659. 114
- ALMA PARTNERSHIP, BROGAN, C.L., PÉREZ, L.M., HUNTER, T.R., DENT, W.R.F., HALES, A.S., HILLS, R.E., CORDER, S., FOMALONT, E.B., VLACHAKIS, C., ASAKI, Y., BARKATS, D., HIROTA, A., HODGE, J.A., IMPELLIZZERI, C.M.V., KNEISSL, R., LIUZZO, E., LUCAS, R., MARCELINO, N., MATSUSHITA, S., NAKANISHI, K., PHILLIPS, N., RICHARDS, A.M.S., TOLEDO, I., ALADRO, R., BROGUIERE, D., CORTES, J.R., CORTES, P.C., ESPADA, D., GALARZA, F., GARCIA-APPADOO, D., GUZMAN-RAMIREZ,

- L., HUMPHREYS, E.M., JUNG, T., KAMENO, S., LAING, R.A., LEON, S., MARCONI, G., MIGNANO, A., NIKOLIC, B., NYMAN, L.A., RADISZCZ, M., REMIJAN, A., RODÓN, J.A., SAWADA, T., TAKAHASHI, S., TILANUS, R.P.J., VILA VILARO, B., WATSON, L.C., WIKLIND, T., AKIYAMA, E., CHAPILLON, E., DE GREGORIO-MONSALVO, I., DI FRANCESCO, J., GUETH, F., KAWAMURA, A., LEE, C.F., NGUYEN LUONG, Q., MANGUM, J., PIETU, V., SANHUEZA, P., SAIGO, K., TAKAKUWA, S., UBACH, C., VAN KEMPEN, T., WOOTTEN, A., CASTRO-CARRIZO, A., FRANCKE, H., GALLARDO, J., GARCIA, J., GONZALEZ, S., HILL, T., KAMINSKI, T., KURONO, Y., LIU, H.Y., LOPEZ, C., MORALES, F., PLARRE, K., SCHIEVEN, G., TESTI, L., VIDELA, L., VILLARD, E., ANDREANI, P., HIBBARD, J.E. & TATEMATSU, K. (2015). The 2014 ALMA Long Baseline Campaign: First Results from High Angular Resolution Observations toward the HL Tau Region. *ApJL*, **808**, L3. 8, 168
- ANDRE, P., WARD-THOMPSON, D. & BARSONY, M. (1993). Submillimeter continuum observations of Rho Ophiuchi A - The candidate protostar VLA 1623 and prestellar clumps. *ApJ*, **406**, 122–141. 7
- ANDRÉ, P., MOTTE, F. & BACMANN, A. (1999). Discovery of an Extremely Young Accreting Protostar in Taurus. *ApJL*, **513**, L57–L60. 50
- ANDREWS, S.M. & WILLIAMS, J.P. (2007). A Submillimeter View of Circumstellar Dust Disks in ρ Ophiuchi. *ApJ*, **671**, 1800–1812. 11
- BACCIOTTI, F., RAY, T.P., MUNDT, R., EISLÖFFEL, J. & SOLF, J. (2002). Hubble Space Telescope/STIS Spectroscopy of the Optical Outflow from DG

Tauri: Indications for Rotation in the Initial Jet Channel. *ApJ*, **576**, 222–231.

12

BALBUS, S.A. & HAWLEY, J.F. (1991). A powerful local shear instability in weakly magnetized disks. I - Linear analysis. II - Nonlinear evolution. *ApJ*, **376**, 214–233. 14

BALBUS, S.A. & PAPALOIZOU, J.C.B. (1999). On the Dynamical Foundations of α Disks. *ApJ*, **521**, 650–658. 14

BALLESTEROS-PAREDES, J., VÁZQUEZ-SEMADENI, E. & SCALO, J. (1999). Clouds as Turbulent Density Fluctuations: Implications for Pressure Confinement and Spectral Line Data Interpretation. *ApJ*, **515**, 286–303. 3

BELTRÁN, M.T., BRAND, J., CESARONI, R., FONTANI, F., PEZZUTO, S., TESTI, L. & MOLINARI, S. (2006). Search for massive protostar candidates in the southern hemisphere. II. Dust continuum emission. *A&A*, **447**, 221–233. 65

BERGIN, E.A. & TAFALLA, M. (2007). Cold Dark Clouds: The Initial Conditions for Star Formation. *ARA&A*, **45**, 339–396. 3, 4

BISSANTZ, N., ENGLMAIER, P. & GERHARD, O. (2003). Gas dynamics in the Milky Way: second pattern speed and large-scale morphology. *MNRAS*, **340**, 949–968. 67

BLANDFORD, R.D. & PAYNE, D.G. (1982). Hydromagnetic flows from accretion discs and the production of radio jets. *MNRAS*, **199**, 883–903. 12

BLITZ, L. & WILLIAMS, J. (1999). Molecular clouds (a review). *Astro.ph.* 3

- BODENHEIMER, P., LAUGHLIN, G.P., RÓZYCZKA, M. & YORKE, H.W., eds. (2007). *Numerical Methods in Astrophysics: An Introduction*. 42
- BOLEY, A.C. (2009). The Two Modes of Gas Giant Planet Formation. *ApJL*, **695**, L53–L57. 52, 73, 165
- BOLEY, A.C. & DURISEN, R.H. (2008). Gravitational Instabilities, Chondrule Formation, and the FU Orionis Phenomenon. *ApJ*, **685**, 1193–1209. 51
- BOLEY, A.C., DURISEN, R.H., NORDLUND, Å. & LORD, J. (2007a). Three-Dimensional Radiative Hydrodynamics for Disk Stability Simulations: A Proposed Testing Standard and New Results. *ApJ*, **665**, 1254–1267. 1, 17
- BOLEY, A.C., DURISEN, R.H., NORDLUND, Å. & LORD, J. (2007b). Three-Dimensional Radiative Hydrodynamics for Disk Stability Simulations: A Proposed Testing Standard and New Results. *ApJ*, **665**, 1254–1267. 52
- BONEBERG, D.M., DALE, J.E., GIRICHIDIS, P. & ERCOLANO, B. (2014). Turbulence in Giant Molecular Clouds: The effect of photoionisation feedback. *ArXiv e-prints*. 3
- BONNOR, W.B. (1956). Boyle’s Law and gravitational instability. *MNRAS*, **116**, 351. 52
- BOTSCHWINA, P., HORN, M., FLUGGE, J. & SEEGER, S. (1993). Ab initio calculations on molecules of interest to interstellar cloud chemistry. *J. Chem. Soc., Faraday Trans.*, **89**, 2219–2230. 58
- BOURKE, T.L., MYERS, P.C., EVANS, N.J., II, DUNHAM, M.M., KAUFFMANN, J., SHIRLEY, Y.L., CRAPSI, A., YOUNG, C.H., HUARD, T.L.,

- BROOKE, T.Y., CHAPMAN, N., CIEZA, L., LEE, C.W., TEUBEN, P. & WAHHAJ, Z. (2006). The Spitzer c2d Survey of Nearby Dense Cores. II. Discovery of a Low-Luminosity Object in the “Evolved Starless Core” L1521F. *ApJL*, **649**, L37–L40. 52
- BRAIDING, C.R. & WARDLE, M. (2012). The Hall effect in star formation. *MNRAS*, **422**, 261–281. 49
- BRINCH, C. & HOGERHEIJDE, M.R. (2011). Lime - a flexible, non-lte line excitation and radiation transfer method for millimeter and far-infrared wavelengths. *AA*, **523**. 30, 31, 32
- BROWN, D.W., CHANDLER, C.J., CARLSTROM, J.E., HILLS, R.E., LAY, O.P., MATTHEWS, B.C., RICHER, J.S. & WILSON, C.D. (2000). A submillimetre survey for protostellar accretion discs using the JCMT-CSO interferometer. *MNRAS*, **319**, 154–162. 50
- CASELLI, P., KETO, E., BERGIN, E.A., TAFALLA, M., AIKAWA, Y., DOUGLAS, T., PAGANI, L., YÍLDÍZ, U.A., VAN DER TAK, F.F.S., WALMSLEY, C.M., CODELLA, C., NISINI, B., KRISTENSEN, L.E. & VAN DISHOECK, E.F. (2012). First Detection of Water Vapor in a Pre-stellar Core. *ApJL*, **759**, L37. 52, 58
- CASTOR, J.I., ABBOTT, D.C. & KLEIN, R.I. (1975). Radiation-driven winds in Of stars. *ApJ*, **195**, 157–174. 18
- CHANDLER, C.J., KOERNER, D.W., SARGENT, A.I. & WOOD, D.O.S. (1995). Dust Emission from Protostars: The Disk and Envelope of HH 24 MMS. *ApJL*, **449**, L139. 50

- CHEN, X., ARCE, H.G., ZHANG, Q., BOURKE, T.L., LAUNHARDT, R., SCHMALZL, M. & HENNING, T. (2010). L1448 IRS2E: A Candidate First Hydrostatic Core. *ApJ*, **715**, 1344–1351. 5
- CHIANG, E.I. & GOLDREICH, P. (1997). Spectral Energy Distributions of T Tauri Stars with Passive Circumstellar Disks. *ApJ*, **490**, 368–376. 79
- CHOI, M., TATEMATSU, K., PARK, G. & KANG, M. (2007). Ammonia Imaging of the Disks in the NGC 1333 IRAS 4A Protobinary System. *ApJL*, **667**, L183–L186. 50
- COSSINS, P., LODATO, G. & TESTI, L. (2010). Resolved images of self-gravitating circumstellar discs with ALMA. *MNRAS*, **407**, 181–188. 50
- D’ALESSIO, P., CALVET, N. & HARTMANN, L. (2001). Accretion Disks around Young Objects. III. Grain Growth. *ApJ*, **553**, 321–334. 54
- DIONATOS, O. (2010). The Molecular and Atomic Components of the HH211-mm Outflow Observed with Spitzer. In K. Tsinganos, D. Hatzidimitriou & T. Matsakos, eds., *9th International Conference of the Hellenic Astronomical Society*, vol. 424 of *Astronomical Society of the Pacific Conference Series*, 149. 13
- DOUGLAS, T.A., CASELLI, P., ILEE, J.D., BOLEY, A.C., HARTQUIST, T.W., DURISEN, R.H. & RAWLINGS, J.M.C. (2013). Simulated observations of young gravitationally unstable protoplanetary discs. *MNRAS*, **433**, 2064–2074. 1

- DREW, J.E., PROGA, D. & STONE, J.M. (1998). A radiation-driven disc wind model for massive young stellar objects. *MNRAS*, **296**, L6. 20, 21, 76, 77, 85, 88
- DURISEN, R.H., BOSS, A.P., MAYER, L., NELSON, A.F., QUINN, T. & RICE, W.K.M. (2007). Gravitational Instabilities in Gaseous Protoplanetary Disks and Implications for Giant Planet Formation. *Protostars and Planets V*, 607–622. 18
- EBERT, R. (1957). Zur Instabilität kugelsymmetrischer Gasverteilungen. Mit 2 Textabbildungen. *ZA*, **42**, 263. 52
- ELWERT, G. (1954). Die weiche röntgenstrahlung der ungestörten sonnenkorona. *Zeitschrift für Naturforschung A*, **9**, 637–653. 119
- ENOCH, M.L., LEE, J.E., HARVEY, P., DUNHAM, M.M. & SCHNEE, S. (2010). A Candidate Detection of the First Hydrostatic Core. *ApJL*, **722**, L33–L38. 5
- ENOCH, M.L., CORDER, S., DUCHÊNE, G., BOCK, D.C., BOLATTO, A.D., CULVERHOUSE, T.L., KWON, W., LAMB, J.W., LEITCH, E.M., MARRONE, D.P., MUCHOVEJ, S.J., PÉREZ, L.M., SCOTT, S.L., TEUBEN, P.J., WRIGHT, M.C.H. & ZAUDERER, B.A. (2011). Disk and Envelope Structure in Class 0 Protostars. II. High-resolution Millimeter Mapping of the Serpens Sample. *ApJS*, **195**, 21. 50
- EVANS, M.G., ILEE, J.D., BOLEY, A.C., CASELLI, P., DURISEN, R.H., HARTQUIST, T.W. & RAWLINGS, J.M.C. (2015). Gravitational instabilities

- in a protosolar-like disc - I. Dynamics and chemistry. *MNRAS*, **453**, 1147–1163. 168
- FALLE, S.A.E.G. (1991). Self-similar jets. *MNRAS*, **250**, 581–596. 45
- FLOWER, D.R. (2001). The rotational excitation of co by h 2. *Journal of Physics B: Atomic, Molecular and Optical Physics*, **34**, 2731. 58
- FORGAN, D. & RICE, K. (2013). The possibility of a self-gravitating disc around L1527 IRS? *MNRAS*, **433**, 1796–1801. 65
- GALVÁN-MADRID, R., GODDI, C. & RODRÍGUEZ, L.F. (2012). ALMA and VLA observations of recombination lines and continuum toward the Becklin-Neugebauer object in Orion. *A&A*, **547**, L3. 114
- GIBB, A.G. & HOARE, M.G. (2007). A high-frequency radio continuum study of massive young stellar objects. *MNRAS*, **380**, 246–262. 130, 138
- GIBBONS, P.G., RICE, W.K.M. & MAMATSASHVILI, G.R. (2012). Planetesimal formation in self-gravitating discs. *MNRAS*, **426**, 1444–1454. 73, 165
- GOICOECHEA, J.R., TEYSSIER, D., ETXALUZE, M., GOLDSMITH, P.F., OSSENKOPF, V., GERIN, M., BERGIN, E.A., BLACK, J.H., CERNICHARO, J., CUADRADO, S., ENCRENAZ, P., FALGARONE, E., FUENTE, A., HACAR, A., LIS, D.C., MARCELINO, N., MELNICK, G.J., MULLER, H.S.P., PERS-SON, C., PETY, J., ROLLIG, M., SCHILKE, P., SIMON, R., SNELL, R.L. & STUTZKI, J. (2015). Velocity-resolved [CII] emission and [CII]/FIR Mapping along Orion with Herschel. *ArXiv e-prints*. 114

- GREEN, S. & CHAPMAN, S. (1978). Collisional excitation of interstellar molecules - Linear molecules CO, CS, OCS, and HC3N. *ApJS*, **37**, 169–194. 58
- GUZMÁN, A.E., GARAY, G., RODRÍGUEZ, L.F., MORAN, J., BROOKS, K.J., BRONFMAN, L., NYMAN, L.Å., SANHUEZA, P. & MARDONES, D. (2014). The Slow Ionized Wind and Rotating Disklike System that are Associated with the High-mass Young Stellar Object G345.4938+01.4677. *ApJ*, **796**, 117. 114, 140
- HARRIES, T.J. (2015). Radiation-hydrodynamical simulations of massive star formation using Monte Carlo radiative transfer - I. Algorithms and numerical methods. *MNRAS*, **448**, 3156–3166. 171
- HARTMANN, L., CALVET, N., GULLBRING, E. & D’ALESSIO, P. (1998). Accretion and the Evolution of T Tauri Disks. *ApJ*, **495**, 385–400. 14
- HARTMANN, L., D’ALESSIO, P., CALVET, N. & MUZEROLLE, J. (2006). Why Do T Tauri Disks Accrete? *ApJ*, **648**, 484–490. 11
- HAWLEY, J.F., SMARR, L.L. & WILSON, J.R. (1984). A numerical study of nonspherical black hole accretion. I Equations and test problems. *ApJ*, **277**, 296–311. 43
- HAYFIELD, T., MAYER, L., WADSLEY, J. & BOLEY, A.C. (2011a). The properties of pre-stellar discs in isolated and multiple pre-stellar systems. *MNRAS*, **417**, 1839–1852. 12

- HAYFIELD, T., MAYER, L., WADSLEY, J. & BOLEY, A.C. (2011b). The properties of pre-stellar discs in isolated and multiple pre-stellar systems. *MNRAS*, **417**, 1839–1852. 49
- HOARE, M.G. (2006). An Equatorial Wind from the Massive Young Stellar Object S140 IRS 1. *ApJ*, **649**, 856–861. 21, 22, 155, 161, 167
- HOSOKAWA, T. & OMUKAI, K. (2009). Evolution of Massive Protostars with High Accretion Rates. *ApJ*, **691**, 823–846. 10, 84, 112, 166
- HUMMER, D.G. (1988). A fast and accurate method for evaluating the nonrelativistic free-free Gaunt factor for hydrogenic ions. *ApJ*, **327**, 477–484. 119
- ILEE, J.D., BOLEY, A.C., CASELLI, P., DURISEN, R.H., HARTQUIST, T.W. & RAWLINGS, J.M.C. (2011). Chemistry in a gravitationally unstable protoplanetary disc. *MNRAS*, **417**, 2950–2961. 2, 51
- ILEE, J.D., WHEELWRIGHT, H.E., OUDMAIJER, R.D., DE WIT, W.J., MAUD, L.T., HOARE, M.G., LUMSDEN, S.L., MOORE, T.J.T., URQUHART, J.S. & MOTTRAM, J.C. (2013). CO bandhead emission of massive young stellar objects: determining disc properties. *MNRAS*, **429**, 2960–2973. 76, 124
- JEANS, J. (1929). The wider aspects of cosmogony. *Astronomy and Cosmogony*. 4
- JOHNSON, J.L. & LI, H. (2013). Constraints on planet formation via gravitational instability across cosmic time. *MNRAS*. 73, 165

- JONKHEID, B.J. (2006). *Chemistry in evolving protoplanetary disks*. Ph.D. thesis, Leiden Observatory, Leiden University, P.O. Box 9513, 2300 RA Leiden, The Netherlands. 6
- JOOS, M., HENNEBELLE, P. & CIARDI, A. (2012). Protostellar disk formation and transport of angular momentum during magnetized core collapse. *A&A*, **543**, A128. 49, 52
- JOOS, M., HENNEBELLE, P., CIARDI, A. & FROMANG, S. (2013). The influence of turbulence during magnetized core collapse and its consequences on low-mass star formation. *ArXiv e-prints*. 49
- JØRGENSEN, J.K., BOURKE, T.L., MYERS, P.C., DI FRANCESCO, J., VAN DISHOECK, E.F., LEE, C.F., OHASHI, N., SCHÖIER, F.L., TAKAKUWA, S., WILNER, D.J. & ZHANG, Q. (2007). PROSAC: A Submillimeter Array Survey of Low-Mass Protostars. I. Overview of Program: Envelopes, Disks, Outflows, and Hot Cores. *ApJ*, **659**, 479–498. 50
- JØRGENSEN, J.K., VAN DISHOECK, E.F., VISSER, R., BOURKE, T.L., WILNER, D.J., LOMMEN, D., HOGERHEIJDE, M.R. & MYERS, P.C. (2009). PROSAC: a submillimeter array survey of low-mass protostars. II. The mass evolution of envelopes, disks, and stars from the Class 0 through I stages. *A&A*, **507**, 861–879. 50
- KAZES, I. & CRUTCHER, R.M. (1986). Measurement of magnetic-field strengths in molecular clouds Detection of OH-line Zeeman splitting. *A&A*, **164**, 328–336. 4

- KENNICUTT, R.C. & EVANS, N.J. (2012). Star Formation in the Milky Way and Nearby Galaxies. *ARA&A*, **50**, 531–608. 3
- KETO, E. & CASELLI, P. (2010). Dynamics and depletion in thermally supercritical starless cores. *MNRAS*, **402**, 1625–1634. 51
- KETO, E., RAWLINGS, J. & CASELLI, P. (2014). Chemistry and radiative transfer of water in cold, dense clouds. *MNRAS*, **440**, 2616–2624. 52, 53
- KIM, W.T. & OSTRIKER, E.C. (2007). Gravitational Runaway and Turbulence Driving in Star-Gas Galactic Disks. *ApJ*, **660**, 1232–1245. 3
- KLESSEN, R.S. & GLOVER, S.C.O. (2014). Physical Processes in the Interstellar Medium. *ArXiv e-prints*. 30
- KRASNOPOLSKY, R., LI, Z.Y. & SHANG, H. (2011). Disk Formation in Magnetized Clouds Enabled by the Hall Effect. *ApJ*, **733**, 54. 49
- KRAUS, S., HOFMANN, K.H., MENTEN, K.M., SCHERTL, D., WEIGELT, G., WYROWSKI, F., MEILLAND, A., PERRAUT, K., PETROV, R., ROBBERDUBOIS, S., SCHILKE, P. & TESTI, L. (2010). A hot compact dust disk around a massive young stellar object. *Nature*, **466**, 339–342. 75
- KRUMHOLZ, M.R. & MATZNER, C.D. (2009). The Dynamics of Radiation-pressure-dominated H II Regions. *ApJ*, **703**, 1352–1362. 12, 13, 76
- KRUMHOLZ, M.R., MCKEE, C.F. & KLEIN, R.I. (2005). The formation of stars by gravitational collapse rather than competitive accretion. *Nature*, **438**, 332–334. 9

- KRUMHOLZ, M.R., KLEIN, R.I. & MCKEE, C.F. (2007). Molecular Line Emission from Massive Protostellar Disks: Predictions for ALMA and EVLA. *ApJ*, **665**, 478–491. 50
- KUIPER, R., KLAHR, H., BEUTHER, H. & HENNING, T. (2010). Circumventing the Radiation Pressure Barrier in the Formation of Massive Stars via Disk Accretion. *ApJ*, **722**, 1556–1576. 76
- KUIPER, R., KLAHR, H., BEUTHER, H. & HENNING, T. (2011). Three-dimensional Simulation of Massive Star Formation in the Disk Accretion Scenario. *ApJ*, **732**, 20. 13, 76, 170
- KUIPER, R., YORKE, H.W. & TURNER, N.J. (2015). Protostellar Outflows and Radiative Feedback from Massive Stars. *ApJ*, **800**, 86. 9
- LADA, C.J. (1987). Star formation - From OB associations to protostars. In M. Peimbert & J. Jugaku, eds., *Star Forming Regions*, vol. 115 of *IAU Symposium*, 1–17. 7
- LAMERS, H.J.G.L.M. & CASSINELLI, J.P. (1999). *Introduction to Stellar Winds*. 133
- LARSON, R.B. (1969). Numerical calculations of the dynamics of collapsing proto-star. *MNRAS*, **145**, 271. 5
- LI, Z.Y., KRASNOPOLSKY, R. & SHANG, H. (2013). Does Magnetic Field-Rotation Misalignment Solve the Magnetic Braking Catastrophe in Protostellar Disk Formation? *ArXiv e-prints*. 53

- LIU, Y., HERCZEG, G.J., GONG, M., ALLERS, K.N., BROWN, J.M., KRAUS, A.L., LIU, M.C., SHKOLNIK, E.L. & VAN DISHOECK, E.F. (2015). Herschel/PACS view of disks around low-mass stars and brown dwarfs in the TW Hydrae association. *A&A*, **573**, A63. 10
- LLOYD, S. (1982). Least squares quantization in PCM. *IEEE T Inform Theory*, **28**, 129–137. 30
- LODATO, G. (2008). Classical disc physics. *New Astronomy Review*, **52**, 21–41. 10, 11, 13, 15
- LOONEY, L.W., MUNDY, L.G. & WELCH, W.J. (2000). Unveiling the Circumstellar Envelope and Disk: A Subarcsecond Survey of Circumstellar Structures. *ApJ*, **529**, 477–498. 50
- LUMSDEN, S.L., WHEELWRIGHT, H.E., HOARE, M.G., OUDMAIJER, R.D. & DREW, J.E. (2012). Tracers of discs and winds around intermediate- and high-mass young stellar objects. *MNRAS*, **424**, 1088–1104. 114, 140, 161, 167
- LYNDEN-BELL, D. & PRINGLE, J.E. (1974). The evolution of viscous discs and the origin of the nebular variables. *MNRAS*, **168**, 603–637. 14
- MACHIDA, M.N. & HOSOKAWA, T. (2013). Evolution of protostellar outflow around low-mass protostar. *MNRAS*, **431**, 1719–1744. 56
- MACHIDA, M.N. & MATSUMOTO, T. (2011). The origin and formation of the circumstellar disc. *MNRAS*, **413**, 2767–2784. 11

- MACHIDA, M.N., INUTSUKA, S.I. & MATSUMOTO, T. (2011a). Effect of Magnetic Braking on Circumstellar Disk Formation in a Strongly Magnetized Cloud. *PASJ*, **63**, 555–. 7
- MACHIDA, M.N., INUTSUKA, S.I. & MATSUMOTO, T. (2011b). Effect of Magnetic Braking on Circumstellar Disk Formation in a Strongly Magnetized Cloud. *PASJ*, **63**, 555–. 49
- MAUD, L.T., HOARE, M.G., GIBB, A.G., SHEPHERD, D. & INDEBETOUW, R. (2013). High angular resolution millimetre continuum observations and modelling of S140-IRS1. *MNRAS*, **428**, 609–624. 21, 23, 75
- MENZEL, D.H. (1968). Oscillator Strengths for High-level Transitions in Hydrogen. *Nature*, **218**, 756–757. 122
- MESTEL, L. & SPITZER, L., JR. (1956). Star formation in magnetic dust clouds. *MNRAS*, **116**, 503. 2
- OSORIO, M., ANGLADA, G., CARRASCO-GONZÁLEZ, C., TORRELLES, J.M., MACÍAS, E., RODRÍGUEZ, L.F., GÓMEZ, J.F., D’ALESSIO, P., CALVET, N., NAGEL, E., DENT, W.R.F., QUANZ, S.P., REGGIANI, M. & MAYENGIJON, J.M. (2014). Imaging the Inner and Outer Gaps of the Pre-transitional Disk of HD 169142 at 7 mm. *ApJL*, **791**, L36. 8
- OSSENKOPF, V. & HENNING, T. (1994). Dust opacities for protostellar cores. *A&A*, **291**, 943–959. 54

- OSSENKOPF, V., KOUMPIA, E., OKADA, Y., MOOKERJEA, B., VAN DER TAK, F.F.S., SIMON, R., PÜTZ, P. & GÜSTEN, R. (2015). Fine-structure line deficit in S 140. *A&A*, **580**, A83. 114
- PAULDRACH, A., PULS, J. & KUDRITZKI, R.P. (1986). Radiation-driven winds of hot luminous stars - Improvements of the theory and first results. *A&A*, **164**, 86–100. 91
- PÉREZ-BEAUPUITS, J.P., STUTZKI, J., OSSENKOPF, V., SPAANS, M., GÜSTEN, R. & WIESEMAYER, H. (2015). Detection of a large fraction of atomic gas not associated with star-forming material in M17 SW. *A&A*, **575**, A9. 114
- PERSSON, M.V., JØRGENSEN, J.K. & VAN DISHOECK, E.F. (2012). Subarc-second resolution observations of warm water toward three deeply embedded low-mass protostars. *A&A*, **541**, A39. 50
- PINEDA, J.E., ARCE, H.G., SCHNEE, S., GOODMAN, A.A., BOURKE, T., FOSTER, J.B., ROBITAILLE, T., TANNER, J., KAUFFMANN, J., TAFALLA, M., CASELLI, P. & ANGLADA, G. (2011). The Enigmatic Core L1451-mm: A First Hydrostatic Core? Or a Hidden VeLLO? *ApJ*, **743**, 201. 5
- PINEDA, J.E., MAURY, A.J., FULLER, G.A., TESTI, L., GARCÍA-APPADOO, D., PECK, A.B., VILLARD, E., CORDER, S.A., VAN KEMPEN, T.A., TURNER, J.L., TACHIHARA, K. & DENT, W. (2012). The first ALMA view of IRAS 16293-2422. Direct detection of infall onto source B and high-resolution kinematics of source A. *A&A*, **544**, L7. 50

- PROGA, D., STONE, J.M. & DREW, J.E. (1998). Radiation-driven winds from luminous accretion discs. *MNRAS*, **295**, 595. 19, 21, 76, 90, 104, 111, 165
- PUDRITZ, R.E. & NORMAN, C.A. (1983). Centrifugally driven winds from contracting molecular disks. *ApJ*, **274**, 677–697. 12
- PULS, J., SPRINGMANN, U. & LENNON, M. (2000). Radiation driven winds of hot luminous stars. XIV. Line statistics and radiative driving. *A&AS*, **141**, 23–64. 87
- REN, J.Z., LIU, T., WU, Y. & LI, L. (2011). Outflow activities in the young high-mass stellar object G23.44-0.18. *MNRAS*, **415**, L49–L53. 58
- RICCI, L., TESTI, L., NATTA, A., SCHOLZ, A., DE GREGORIO-MONSALVO, I. & ISELLA, A. (2014). Brown Dwarf Disks with ALMA. *ApJ*, **791**, 20. 10
- ROBERTS, W.W. (1969). Large-Scale Shock Formation in Spiral Galaxies and its Implications on Star Formation. *ApJ*, **158**, 123. 2
- RUBIN, R.H., SIMPSON, J.P., HAAS, M.R. & ERICKSON, E.F. (1991). Axisymmetric model of the ionized gas in the Orion Nebula. *ApJ*, **374**, 564–579. 123
- RUGE, J.P., WOLF, S., URIBE, A.L. & KLAHR, H.H. (2013). Tracing large-scale structures in circumstellar disks with ALMA. *A&A*, **549**, A97. 50
- RYBICKI, G.B. & LIGHTMAN, A.P. (1979). *Radiative processes in astrophysics*. 117
- RYBICKI, G.B. & LIGHTMAN, A.P. (1986). *Radiative Processes in Astrophysics*. xiv, 26, 120, 121

- SÁNCHEZ-MONGE, Á., CESARONI, R., BELTRÁN, M.T., KUMAR, M.S.N., STANKE, T., ZINNECKER, H., ETOKA, S., GALLI, D., HUMMEL, C.A., MOSCADELLI, L., PREIBISCH, T., RATZKA, T., VAN DER TAK, F.F.S., VIG, S., WALMSLEY, C.M. & WANG, K.S. (2013). A candidate circumbinary Keplerian disk in G35.20-0.74 N: A study with ALMA. *A&A*, **552**, L10. 10
- SCHEUER, P.A.G. (1960). The absorption coefficient of a plasma at radio frequencies. *MNRAS*, **120**, 231. 118
- SCHNEIDER, N., BONTEMPS, S., SIMON, R., OSSENKOPF, V., FEDERRATH, C., KLESSEN, R.S., MOTTE, F., ANDRÉ, P., STUTZKI, J. & BRUNT, C. (2011). The link between molecular cloud structure and turbulence. *A&A*, **529**, A1. 4
- SCHÖIER, F.L., VAN DER TAK, F.F.S., VAN DISHOECK, E.F. & BLACK, J.H. (2005). An atomic and molecular database for analysis of submillimetre line observations. *A&A*, **432**, 369–379. 58
- SHAKURA, N.I. & SUNYAEV, R.A. (1973). Black holes in binary systems. Observational appearance. *A&A*, **24**, 337–355. 14
- SHU, F.H., SHANG, H., GLASSGOLD, A.E. & LEE, T. (1997). X-rays and fluctuating X-winds from protostars. *Science*, **277**, 1475–1479. 12
- SIMON, M., FELLI, M., CASSAR, L., FISCHER, J. & MASSI, M. (1983). Infrared line and radio continuum emission of circumstellar ionized regions. *ApJ*, **266**, 623–645. 114
- STAHLER & PALLA (2004). *The Formation of Stars*. Wiley-VCH. 28, 123

- STANKE, T. & WILLIAMS, J.P. (2007). Molecular CO Outflows in the L1641-N Cluster: Kneading a Cloud Core. *ApJ*, **133**, 1307–1320. 60
- TAN, J.C., BELTRÁN, M.T., CASELLI, P., FONTANI, F., FUENTE, A., KRUMHOLZ, M.R., MCKEE, C.F. & STOLTE, A. (2014). Massive Star Formation. *Protostars and Planets VI*, 149–172. 8
- TOOMRE, A. (1964). On the gravitational stability of a disk of stars. *ApJ*, **139**, 1217–1238. 16
- TROSCOMPT, N., FAURE, A., WIESENFELD, L., CECCARELLI, C. & VALIRON, P. (2009). Rotational excitation of formaldehyde by hydrogen molecules: ortho-H₂CO at low temperature. *A&A*, **493**, 687–696. 58
- VAN DER TAK, F.F.S., BOONMAN, A.M.S., BRAAKMAN, R. & VAN DISHOECK, E.F. (2003). Sulphur chemistry in the envelopes of massive young stars. *A&A*, **412**, 133–145. 60
- VAN DER TAK, F.F.S., BLACK, J.H., SCHÖIER, F.L., JANSEN, D.J. & VAN DISHOECK, E.F. (2007). A computer program for fast non-LTE analysis of interstellar line spectra. With diagnostic plots to interpret observed line intensity ratios. *A&A*, **468**, 627–635. 27
- VÁZQUEZ-SEMADENI, E. (2011). Theory of Feedback in Clusters and Molecular Cloud Turbulence. In J. Alves, B.G. Elmegreen, J.M. Girart & V. Trimble, eds., *Computational Star Formation*, vol. 270 of *IAU Symposium*, 275–282. 3

- VELUSAMY, T., LANGER, W.D., GOLDSMITH, P.F. & PINEDA, J.L. (2015). Internal structure of spiral arms traced with [C II]: Unraveling the warm ionized medium, H I, and molecular emission lanes. *A&A*, **578**, A135. 114
- VISSER, R., VAN DISHOECK, E.F., DOTY, S.D. & DULLEMOND, C.P. (2009). The chemical history of molecules in circumstellar disks. I. Ices. *A&A*, **495**, 881–897. 51
- VISSER, R., DOTY, S.D. & VAN DISHOECK, E.F. (2011). The chemical history of molecules in circumstellar disks. II. Gas-phase species. *A&A*, **534**, A132. 51
- WANG, K.S., VAN DER TAK, F.F.S. & HOGERHEIJDE, M.R. (2012). Kinematics of the inner thousand AU region around the young massive star AFGL 2591-VLA3: a massive disk candidate? *A&A*, **543**, A22. 10
- WERNLI, M., VALIRON, P., FAURE, A., WIESENFELD, L., JANKOWSKI, P. & SZALEWICZ, K. (2006). Improved low-temperature rate constants for rotational excitation of CO by H₂. *A&A*, **446**, 367–372. 58
- WIESE, W.L. & FUHR, J.R. (2009). Accurate atomic transition probabilities for hydrogen, helium, and lithium. *Journal of Physical and Chemical Reference Data*, **38**, 565–719. 122
- WILSON, T.L. & PAULS, T. (1984). Radio continuum and recombination line observations of Orion A. *A&A*, **138**, 225–230. 123
- WILSON, T.L. & ROOD, R. (1994). Abundances in the Interstellar Medium. *ARA&A*, **32**, 191–226. 58, 88

- WRIGHT, A.E. & BARLOW, M.J. (1975). The radio and infrared spectrum of early-type stars undergoing mass loss. *MNRAS*, **170**, 41–51. 113, 137
- YANG, B., STANCIL, P.C., BALAKRISHNAN, N. & FORREY, R.C. (2010). Rotational Quenching of CO due to H₂ Collisions. *ApJ*, **718**, 1062–1069. 58
- YILDIZ, U.A., KRISTENSEN, L.E., VAN DISHOECK, E.F., BELLOCHE, A., VAN KEMPEN, T.A., HOGERHEIJDE, M.R., GÜSTEN, R. & VAN DER MAREL, N. (2012). APEX-CHAMP⁺ high-J CO observations of low-mass young stellar objects. III. NGC 1333 IRAS 4A/4B envelope, outflow, and ultraviolet heating. *A&A*, **542**, A86. 62
- YORKE, H.W. & SONNHALTER, C. (2002). On the Formation of Massive Stars. *ApJ*, **569**, 846–862. 12
- YOUNG, K.E., LEE, J.E., EVANS, N.J., II, GOLDSMITH, P.F. & DOTY, S.D. (2004). Probing Pre-Protostellar Cores with Formaldehyde. *ApJ*, **614**, 252–266. 58
- ZAPATA, L.A., LOINARD, L., RODRÍGUEZ, L.F., HERNÁNDEZ-HERNÁNDEZ, V., TAKAHASHI, S., TREJO, A. & PARISE, B. (2013). ALMA 690 GHz Observations of IRAS 16293-2422B: Infall in a Highly Optically Thick Disk. *ApJL*, **764**, L14. 50
- ZUCKERMAN, B. & EVANS, N.J., II (1974). Models of massive molecular clouds. *ApJL*, **192**, L149–L152. 3